# PIEZOELECTRICITY IN ZnO-BASED MULTILAYER STRUCTURES FOR SENSOR APPLICATIONS

**by**

**YING CHEN**

**A dissertation submitted to the**

**Graduate School-New Brunswick**

**Rutgers, The State University of New Jersey**

**In partial fulfillment of the requirements**

**For the degree of**

**Doctor of Philosophy**

**Graduate Program in Electrical and Computer Engineering**

**Written under the direction of**

**Professor Yicheng Lu**

**And approved by**

_____

_____

_____

_____

**New Brunswick, New Jersey**

**May, 2008**

## ABSTRACT OF THE DISSERTATION

### Piezoelectricity in ZnO-based Multilayer Structures for Sensor Applications

By YING CHEN

Dissertation Director:

Professor Yicheng Lu

Znic oxide (ZnO) is a multifunctional material with promising applications. Through proper doping, ZnO can be made transparent and conductive, piezoelectric, or ferromagnetic. Piezoelectric ZnO which possess large electromechanical coupling coefficients has been deposited on high velocity and low loss substrates to develop surface acoustic wave (SAW) and bulk acoustic wave (BAW) devices. Such devices can be used in both communications and sensors fields. This dissertation focuses on the integration of piezoelectric ZnO with various important semiconductor materials, including GaN, SiC, and Si, for the acoustic wave based sensor applications.

The piezoelectric properties in ZnO/$Al_xGa_{1-x}N$/c-$Al_2O_3$ structure are investigated. The layered structure provides the flexibility to tailor acoustic properties by varying the Al composition in $Al_xGa_{1-x}N$, and the thickness ratio of ZnO to $Al_xGa_{1-x}N$. It is found that a wide thickness-frequency product region where coupling is close to its maximum value can be obtained. This multilayer structure is promising to design the high velocity, low loss and wide bandwidth SAW devices, which can be used in both the communications and sensors fields.

A new hybrid deposition technology is developed by using metalorganic chemical vapor deposition (MOCVD) of a thin ZnO buffer layer with a minimum thickness of ~10nm followed by sputtering deposition of a thick (above 2μm) piezoelectric Ni-doped $Mg_xZn_{1-x}O$ films. This novel deposition technology improves piezoelectric properties of a-$Mg_xZn_{1-x}O$ ($0 \le x \le 0.3$) films on r-$Al_2O_3$ for ZnO based tunable SAW device.

Piezoelectric ZnO/SiC-6H structure offers high velocities and high coupling coefficients for high frequency SAW devices, which can be used in high-temperature and harsh environments. Epitaxial ZnO films grown on c-plane [0001] oriented SiC-6H substrates by MOCVD form a rectifying heterojunction.

Thin film bulk acoustic resonators (TFBAR) are demonstrated using piezoelectric $Mg_xZn_{1-x}O$ films on Si substrates with an acoustic mirror consisting of alternating quarter-wavelength $SiO_2$ and W layers. The bulk acoustic velocity of $Mg_xZn_{1-x}O$ increases with increasing Mg composition. A mass sensitivity higher than $10^3$ $Hzcm^2/ng$ is obtained. ZnO nanostructures possess unique advantages for the biosensor applications, such as giant surface areas, high sensitivity, biological compatibility, and integratability with Si-based electronics. A prototype of biosensors integrating TFBAR with functionalized ZnO nanotips is demonstrated with improved sensitivity.

## DEDICATION

This work is dedicated to my husband and best friend

Jian Mao

## ACKNOWLEDGEMENTS

First, I would like to thank my dissertation advisor, Professor Yicheng Lu, for his support, guidance, encouragement, and patience. Prof. Lu's advice and critique are invaluable for my work.

I would like to thank my dissertation committee members, Dr. Kuang Sheng, Dr. Wei Jiang, and Dr. Richard H. Wittstruck for the time and effort they have spent to review this work.

I would like to thank my fellow co-workers in Prof. Lu's research group, who have provided support throughout my work. In particular, I would like to thank Dr. Gaurav Saraf, Dr. Hanhong Chen, and Mr. Ziqing Duan for growth and film characterizations, Dr. Zheng Zhang and Mr. Pavel Reyes for biosensor testing, Dr. Jun Zhu and Dr. Jian Zhong for device processing, and Dr. Nuri Emanetoglu for device simulation.

I would like to thank my family and friends who have supported me through my studies and research at Rutgers. In particular, I would like to thank my husband, Jian Mao, for all the help and support he gave when I study in Rutgers University, and his continued love throughout my whole life. Finally, I would like thank my parents, who have always supported me with their love and prayers, regardless of the distances separating us.

This work has been supported by the National Science Foundation under the grants ECS-0088549, "Monolithically Integrated Tunable ZnO SAW Chip", the New Jersey Commission on Science and Technology with the Research Excellence Center grant “Multi-mode Wireless Sensor (MUSE)”, and ECS-0224166, “Development of ZnO Based Room Temperature Spintronics”.

## TABLE OF CONTENTS

## LIST OF TABLES

## LIST OF ILLUSTRATIONS

# CHAPTER I. INTRODUCTION

## 1.1 Motivation

Znic Oxide (ZnO) emerges not only as a wide energy band gap semiconductor, but also as a multifunctional material. It can be made as piezoelectric, ferromagnetic, transparent and conducting through proper doping or alloying. This dissertation focuses on the integration of piezoelectric ZnO with various important semiconductor materials, including GaN, SiC, and Si, for the acoustic wave based sensor applications.

Piezoelectric thin films have broad applications in transducers, actuators, and resonators. Piezoelectric transducers generate electrical signals in response to mechanical vibrations and produce mechanical energy in response to electrical signals. Based on piezoelectric transducers, surface acoustic wave (SAW) and bulk acoustic wave (BAW) technologies were emerged. Radio-frequency (RF) acoustic wave devices are now widely employed in wireless communication and network systems, such as bandpass and spectrum-shaping filters, convolvers, duplexers, and delay lines. These devices have many advantages, such as small size, low cost, mass-producible, and versatile functionality. In addition, piezoelectric thin films also have been used in sensors, micro-electromechanical systems (MEMS), and nano-electromechanical systems (NEMS). SAW and BAW devices have been developed for sensor applications, including sensing for temperature, pressure, ambient gaseous atmosphere, chemical and biological agents,.

Piezoelectric ZnO has large electromechanical coupling coefficients; furthermore, it can be epitaxially grown on the high acoustic velocity substrates at relatively low temperature, which make it a promising candidate for multi-layer thin film acoustic

devices. By alloying of ZnO with MgO, a ternary compound $Mg_xZn_{1-x}O$ is formed. $Mg_xZn_{1-x}O$ ($0 \le x \le 0.3$) belongs to the (6mm) crystal group and has a wurtzite structure. It can be used as a new piezoelectric material. The phase velocity and electromechanical coupling coefficient of piezoelectric $Mg_xZn_{1-x}O$ films can be tailored by varying Mg composition, which provides more flexibility in SAW filter design. Sapphire is non-piezoelectric material, but has high acoustic velocity and low acoustic attenuation loss. The a-$Mg_xZn_{1-x}O$/r-$Al_2O_3$ structure offers large electromechanical coupling coefficients and higher-order-mode SAW propagation. The epitaxial relationship of a-$Mg_xZn_{1-x}O$ film on r-sapphire substrate is retained as $(11\bar{2}0)$ MgZnO || $(01\bar{1}2)$ $Al_2O_3$ and $[0001]$ MgZnO || $[0\bar{1}11]$ $Al_2O_3$. Due to the in-plane anisotropy of $Mg_xZn_{1-x}O$ grown on r-$Al_2O_3$, it offers another unique advantage as multi-mode SAW generation: the Rayleigh-type and Love-type SAW modes. In particular, this anisotropy property has unique applications for SAW sensors: the Rayleigh wave mode for gas-phase sensing and the Love wave mode for liquid-phase sensing.

AlN, GaN and their ternary alloy $Al_xGa_{1-x}N$ emerge for optoelectronic devices, high-power transistors, and acoustic wave applications. The high acoustic velocities and electromechanical coupling coefficients of piezoelectric $Al_xGa_{1-x}N$ materials make them suitable for high-frequency SAW and BAW devices in wireless communication systems. By integrating ZnO and $Al_xGa_{1-x}N$ into a multi-layer structure, higher order SAW modes with larger coupling coefficients and higher acoustic velocities can be obtained.

SiC has premium material properties, including a large Young's modulus, excellent physical stability, high thermal conductivity, and high acoustic velocities, which make it a good candidate for applications in aircraft, automotive, communication,

and power industries. Low lattice and thermal mismatches between ZnO and SiC promise to grow high quality ZnO/SiC heterostructures. The multifunctionality of ZnO combined with robust physical properties of SiC will lead to many interesting applications, such as optoelectronics, high frequency RF devices, power electronics, and high temperature sensors.

In order to develop high frequency and low loss SAW devices, piezoelectricity in ZnO based multilayer structures, including ZnO/$Al_xGa_{1-x}N$/c-$Al_2O_3$, $Mg_xZn_{1-x}O$/r-$Al_2O_3$, and ZnO/SiC, are investigated, including phase velocity and electromechanical coupling coefficient. The efficient generation of acoustic waves in these layered structures has allowed SAW devices to be used in a wide variety of frequency control systems requiring high frequency, low loss and temperature stability. ZnO based SAW devices can be used as wireless passive identifications tags and miniature chemical/biochemical sensors in diverse fields, including biomedical, pharmaceutical, and environmental monitoring, food science, manufacturing, and homeland security.

Thin film bulk acoustic resonators (TFBARs) are attractive as they offer the capability of monolithic integration of BAW resonators with RF ICs, leading to miniaturization, reducing circuit foot print and cost. Especially, TFBARs allow the implementation of BAW devices from several hundred MHz up to 20 GHz, which leads to development of the ultra-high sensitive sensors. Combining piezoelectric ZnO and $Mg_xZn_{1-x}O$ films with Si substrates, TFBAR sensors can be integrated with other electronic components on the same substrates. Furthermore, such integrated sensors are compatible with small-size microwave aerials, hence can be used for remote wireless sensing. The nanoscale structures of ZnO promise the development of novel sensors and

sensor arrays with faster responses, higher sensitivities, and higher selectivity than the existing ZnO film counterpart because of ZnO nanostructures's giant surface area. The feasibility of integration of ZnO nanostructures with TFBAR is studied for biological and biochemical sensors.

## 1.2 Objectives and Scope of Work

The objective of this research is to study and analyze piezoelectricity in ZnO based multilayer structures. ZnO is integrated with various semiconductor materials for sensor applications. The scope of this work covers:

(1). Deposition of ZnO film on $Al_xGa_{1-x}N$/c-$Al_2O_3$ by RF sputtering technology; characterization of ZnO/$Al_xGa_{1-x}N$/c-$Al_2O_3$ structures using X-ray diffraction (XRD) and scanning electron microscopy (SEM); and demonstration of SAW property tailoring in the ZnO/$Al_xGa_{1-x}N$/c-$Al_2O_3$ system by varying the Al mole composition in $Al_xGa_{1-x}N$ as well as the film thickness ratio of ZnO layer to $Al_xGa_{1-x}N$ layer.

(2) Epitaxial deposition of thick piezoelectric ZnO and $Mg_xZn_{1-x}O$ ($x \leq 0.3$) films on r-plane sapphire substrates using a novel hybrid MOCVD-sputtering technique; analysis of improved piezoelectric properties in a-$Mg_xZn_{1-x}O$/r-$Al_2O_3$ structure.

(3). Analysis and test of SAW properties and electrical characteristics in ZnO/SiC-6H structures.

(4) Feasibility studies of $Mg_xZn_{1-x}O$ based TFBAR on Si substrate; demonstration of a prototype of biosensor by integrating ZnO TFBAR with ZnO nanostructures.

## 1.3 Organization of the Dissertation

After a brief introduction in Chapter 1, surface acoustic wave and bulk acoustic wave devices are reviewed in Chapter 2, along with their applications in communications and sensors. Chapter 2 also presents material constants and piezoelectric applications of wide bandgap semiconductors: ZnO, $Mg_xZn_{1-x}O$, AlN, GaN, $Al_xGa_{1-x}N$, and SiC. The deposition techniques used for piezoelectric ZnO and $Mg_xZn_{1-x}O$ films are also reviewed. The tailoring of SAW properties in ZnO/$Al_xGa_{1-x}N$/c-$Al_2O_3$ multilayer structures is presented in Chapter 3. The simulation results are compared with the measured data from test devices fabricated on piezoelectric ZnO films grown on $Al_xGa_{1-x}N$/c-$Al_2O_3$. Chapter 4 demonstrates the novel hybrid MOCVD-sputtering deposition of ZnO and $Mg_xZn_{1-x}O$ films on r-$Al_2O_3$ substrates, with the results of the structural and piezoelectric characterizations of these films. In Chapter 5, the SAW properties in piezoelectric ZnO/SiC-6H structures are simulated and compared with measured data. Additionally, electrical properties of semiconducting ZnO film on n-type SiC-6H heterojunctions are studied. In Chapter 6, $Mg_xZn_{1-x}O$ thin film bulk acoustic wave resonators are demonstrated. A novel sensor structure by integrating multifunctional ZnO nanostructures with ZnO TFBAR is designed and fabricated. Finally, Chapter 7 summarizes the accomplished tasks and proposes future investigations in the field.

# CHAPTER II. TECHNICAL BACKGROUND

## 2.1 Introduction of Piezoelectricity

Piezoelectricity is the generation of electricity (or electric polarity) due to pressure, especially in a crystallized structure. A material is piezoelectric if the application of an external mechanical stress causes the development of an internal dielectric displacement. This displacement is manifested as an internal electric polarization or a surface electric charge. All centrosymmetric point groups cannot show a piezoelectric effect. Crystals belonging to non-centrosymmetric, except point group O, exhibit a piezoelectric effect of some magnitude, although some of the effects are very small.

The general piezoelectric equations of state are given below,

$$[T] = [c][S] - [d][E] \tag{2.1a}$$

$$[D] = [e][S] + [\varepsilon][E] \tag{2.1b}$$

where [$T$] denotes the stress, [$S$] means the strain., [$E$] is the electric field, [$D$] is the electric displacement, [$c$] are the stiffness coefficients, [$e$] represent the piezoelectric constants for the material, [$d$] is the transpose of the piezoelectric constant [$e$], and [ε] denote the dielectric permittivity of the solid.

The piezoelectric constant, $e_{ijk}$, relates the three components of the electric field to the nine components of the second rank tensor stress.

$$T_{ij} = -e_{ijk} E_k \tag{2.2}$$

Due to symmetry in the crystal, the number of coefficients needed to describe the stress term can be reduced from two to one because $T_{ij} = T_{ji}$. Couples of indices, $ij$ = 11, 12, 33,

23, 31, 12, can be written as 1, 2, 3, 4, 5, 6. The nine components of stress are reduced to six and expressed as $T_i$, and $e_{ijk}$ becomes $e_{ik}$, and $i$ = 1, 2, 3, 4, 5, 6:

$$T = \begin{bmatrix} T_{11} & T_{12} & T_{13} \\ T_{12} & T_{22} & T_{23} \\ T_{13} & T_{23} & T_{33} \end{bmatrix} = \begin{bmatrix} T_1 & T_6 & T_5 \\ T_6 & T_2 & T_4 \\ T_5 & T_4 & T_3 \end{bmatrix} \tag{2.3}$$

$$[e] = \begin{bmatrix} e_{11} & e_{21} & e_{31} \\ e_{12} & e_{22} & e_{32} \\ e_{13} & e_{23} & e_{33} \\ e_{14} & e_{24} & e_{34} \\ e_{15} & e_{25} & e_{35} \\ e_{16} & e_{26} & e_{36} \end{bmatrix} \tag{2.4}$$

The relationship between stress and strain is given using the Hooke's Law,

$$T_{ij} = c_{ijkl}\, S_{kl} \tag{2.5}$$

where $T_{ij}$ is the stress acting along the $x_i$ coordinate direction on a surface whose normal is parallel to the $x_j$ axis. $S_{kl}$ is the strain component defined by,

$$S_{kl} = \frac{1}{2}\left( \frac{\delta u_k}{\delta x_l} + \frac{\delta u_i}{\delta x_k} \right) \tag{2.6}$$

The strain $S_{kl}$ becomes $S_n$ (n = 1, 2, 3, 4, 5, 6) due to symmetry, and the stiffness coefficient matrix [$c$] reduces to a 6 x 6 matrix. Hooke's Law thus becomes:

$$T_i = c_{in}\, S_n \tag{2.7}$$

$$\text{where } [c] = \begin{bmatrix} c_{11} & c_{12} & c_{13} & c_{14} & c_{15} & c_{16} \\ c_{12} & c_{22} & c_{23} & c_{24} & c_{25} & c_{26} \\ c_{13} & c_{23} & c_{33} & c_{34} & c_{35} & c_{36} \\ c_{14} & c_{24} & c_{34} & c_{44} & c_{45} & c_{46} \\ c_{15} & c_{25} & c_{35} & c_{54} & c_{55} & c_{56} \\ c_{16} & c_{26} & c_{36} & c_{46} & c_{56} & c_{66} \end{bmatrix} \tag{2.8}$$

The two important parameters of a piezoelectric material are the acoustic wave velocity and the electromechanical coupling coefficient. These parameters are dependent on the material properties, the specific crystal orientation of the surface, and the propagation direction of the acoustic wave. The electromechanical coupling coefficient, $K$, is to measure of the efficiency of a given piezoelectric material in converting an applied electrical signal into the mechanical energy of an acoustic wave, or otherwise. Usually, the coupling coefficient is widely used as $K^2$, defined by

$$K^2 = \frac{e^2}{c\varepsilon} \tag{2.9}$$

where $c$, $e$ and $\varepsilon$ are the elastic, piezoelectric and dielectric constants for the propagation direction of the acoustic wave in the solid.

## 2.2 Surface Acoustic Wave Devices and Their Applications

Figure 2.1 shows the possible particle displacements of a mechanical wave, relative to the propagation direction [1]. Surface acoustic waves (SAWs) have particle motion in at least two out of three directions of the Cartesian coordinate system. The generalized surface acoustic wave (GSAW) has particle motion in the propagation direction and the two shear directions. The Rayleigh wave mode has only longitudinal and shear vertical particle displacement, while the Love wave mode has only longitudinal and shear horizontal particle displacement.

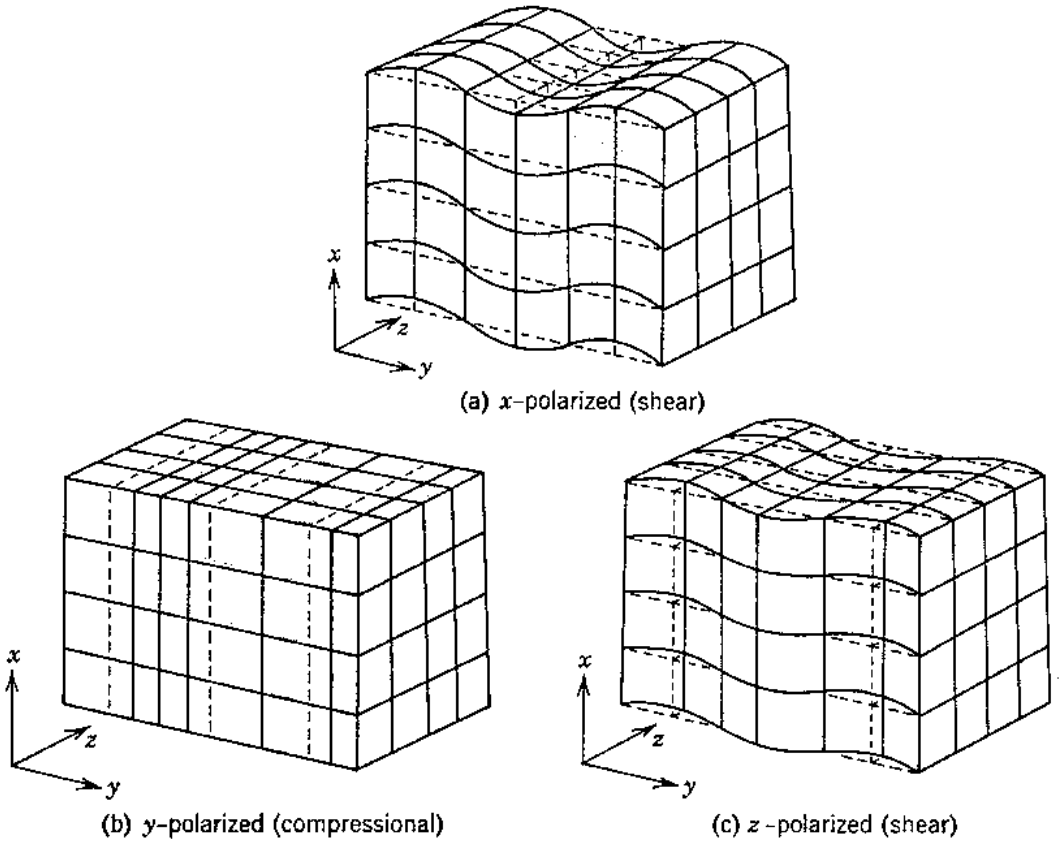


**Figure 2.1.** Acoustic wave propagation (a) shear vertical (SV); (b) longitudinal (compression); (c) shear horizontal (SH) [1].

The basic SAW device is sketched in figure 2.2. A thin metal film is deposited on the top of a piezoelectric crystal substrate without power supplies. An ac voltage applied to the input interdigital transducer (IDT) causes strain, inducing movement of crystal cells, thus causing the lattice to vibrate and generating a mechanical wave. This mechanical wave propagates along the surface, polarizing the lattice cells, generating an electric field. When this wave reaches the output IDT, the accompanying electric field will induce a potential difference between neighboring electrodes and convert into an electrical signal. The layout pattern of these input/output IDTs can be designed to provide

the desired bandpass filtering function $H(f) = V_{output}/V_{input}$ as the SAW propagates along the piezoelectric crystal surface. Through the design of the IDT patterns, SAW devices realize complex digital signal process and find applications in many digital communications systems [2,3].

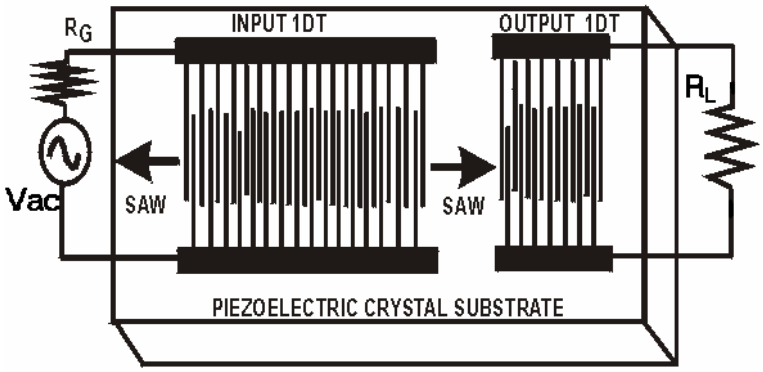


**Figure 2.2.** Basic SAW IDT structure on piezoelectric substrate.

The key specifications for SAW device design are the center frequency, electromechanical coupling coefficient, and bandwidth. The periodicity of the interdigital transducer and the SAW velocity of the substrate determine the center frequency, $f_c$, of the device:

$$v_{SAW} = \lambda_o f_c \tag{2.10}$$

where $\lambda_o$ is the wavelength at $f_c$, which is determined by the periodicity of the IDT.

The coupling coefficient is related to the difference of the metallized surface (i.e. short-circuited or infinite conductivity) velocity, $v_{sc}$, and the free surface (i.e. open circuit) velocity, $v_{oc}$, of the piezoelectric material.

$$K^2 = \frac{-2(v_{sc} - v_{oc})}{v_{oc}} \tag{2.11}$$

The bandwidth of a SAW device is inversely proportional to the number of electrodes in the IDTs:

$$BW_{3dB} = \frac{90}{N} \tag{2.12}$$

where $N$ is the number of electrode pairs in the IDT.

Additionally, the SAW device can operate at selected harmonic frequencies, depending on the metallization ratio $h = a/b$, as shown in figure 2.3 [4]. The IDTs in figure 2.3 (a) and figure 2.3 (b) can operate at selected odd-harmonic frequencies, while the IDT structure in figure 2.3 (c) can operate at selected even and odd harmonics, depending on the metallization ratio.

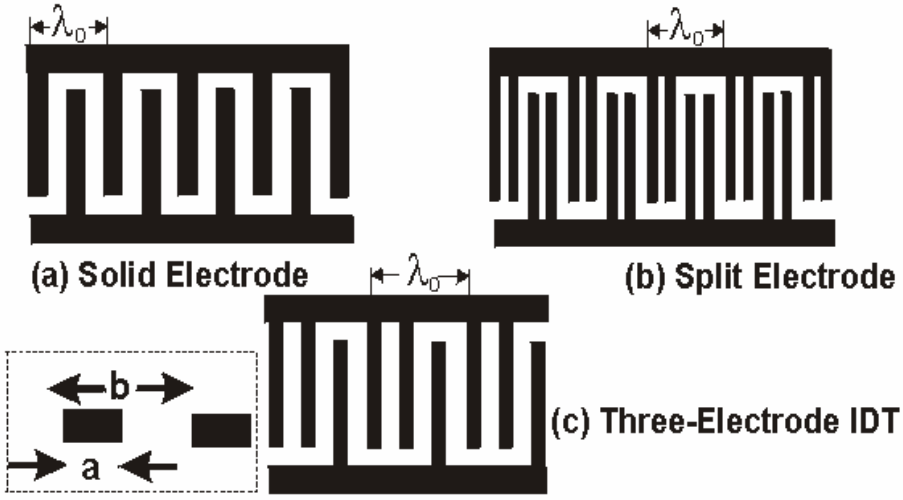


**Figure 2.3.** Some SAW IDT structures for fundamental and harmonic operation [4].

For temperature stable applications, such as oscillators and chemical/biochemical sensors, the temperature coefficient of delay (TCD), or temperature coefficient of

frequency (TCF), is also specified. The temperature coefficient of delay or frequency defined as the change in the time delay with changing environmental temperature with respect to room temperature is dependent on the variation of the material volume and the acoustic velocity.

SAW devices have found wide applications in communication systems for their versatility and efficiency in controlling and processing electrical signal [5]. Also they are easy to fabricate, rugged, cheap, and low weight. These properties have resulted in a multitude of device concepts for a wide range of signal processing functions. SAW devices may be classified into four general types: linear resonator and resonator-filter devices, linear devices using unidirectional IDTs, linear devices using bidirectional IDTs, and nonlinear devices. All these devices have been widely used for antenna duplexers, radio frequency (RF) and intermediate frequency (IF) filters, fixed frequency and tunable oscillator circuits, fixed or variable delay lines, synchronous and asynchronous convolvers, programmable correlators, resonators and resonator-filters for mobile/wireless communications, medical alert transmitters, automobile keyless locks, and garage door openers. As SAW technology has found its way into mass market products such as TV receivers, pagers, keyless entry systems and cellular phones, the production volume has risen to millions of devices produced every day. At the other end of the scale, there are specialized high performance signal processing SAW devices for satellite communication and military applications, such as radar and electronic warfare.

Significant research has been done in the last 20 years in the area of surface acoustic wave sensors. SAW sensors have been very successful and popular for a broad range of applications, including temperature, pressure, torque, viscosity, dew/humidity

and chemical/biochemical sensing. As SAW propagates along the surface of the material, any changes to the characteristics of the propagation path affect the velocity and amplitude of the wave. The output of the sensor is a change in the oscillation frequency or phase, which results from the SAW velocity change. A dual delay line oscillator configuration, in which the oscillation frequencies of a reference and a sensor oscillator are compared, is commonly used to eliminate the environmental effects. Compared with the electrochemical and optical biosensors, piezoelectric biosensors have several attractive features such as multi-domain sensing mechanisms, frequency as output, and good temperature stability [6]. In addition, SAW sensors are competitively priced, inherently rugged, very sensitive, and intrinsically reliable. Some are also capable of being passively and wirelessly interrogated. Being passive, SAW sensors have the advantage of zero power or low power consumption.

Interaction between the acoustic waves and the viscosity, conductivity, mass density and elastic stiffness properties of the propagation medium can give rise to a sensing response. The sensor system based on surface acoustic wave can respond to three mechanisms, i.e., mass loading, viscoelastic effect, and acoustoelectric interaction, which contribute to the change in the SAW velocity according to the following equation [7, 8]:

$$\frac{\Delta v}{v_0} = -c_m f_0 \Delta(\frac{m}{A}) + 4c_e \frac{f_0}{v_0^2} \Delta(hG') - \frac{K^2}{2} \Delta[\frac{\sigma_0^2}{\sigma_0^2 + v_0^2 C_0^2}] \qquad (2.13)$$

which $c_m$ and $c_e$ are the coefficients of mass sensitivity and elasticity of the substrate, *(m/A)* is the change in mass per unit area, $f_0$ is the operating frequency of SAW device, $h$ represents the coated film thickness, $G'$ is the shear modulus, $K^2$ is the electromechanical coupling coefficient, and $\sigma_0$ is the sheet conductivity of coated film. $C_0$ is the capacitance

per unit length of the SAW substrate material and $C_0 = \varepsilon_p + \varepsilon_a$, where $\varepsilon_p$ and $\varepsilon_a$ are the permittivities of the substrate and free space.

However, traditional SAW chemical and biochemical sensors have several drawbacks. For example, a single sensor was functionalized with a chemically sensitive material selective for the analyte [9]. This approach is successful when there are few chemicals present, and depends on the availability of highly specific receptor materials. SAW devices cannot differentiate between physisorbed and molecularly complexed mass on sensor surface, unless a secondary perturbation, such as mechanical or electrical perturbations, accompanies the mass change. Therefore, SAW sensor arrays (chemo-assays) with a different chemically selective coating on each sensor were used for environments containing many chemicals [9]. Furthermore, traditional SAW gas sensors suffer from humidity, while sensors operating in liquid environments suffer from high damping. Rayleigh waves suffer from large attenuation in liquids due to their shear vertical (SV) wave component. Therefore, Lamb and Love waves are utilized for sensors in liquid environments. Love waves have a shear horizontal (SH) instead of a SV wave component, thus are not attenuated by a liquid. They can be used for measuring liquid density and viscosity, as well as for chemical and biochemical sensing [10, 11]. A major limitation of traditional SAW chemical and biochemical sensors is their short lifetime. When the target accumulates on the surface, the sensitivity decreases. Also most SAW biosensors also suffer from “bio-fouling”.

Figure 2.4 (a) shows a schematic of wireless sensor as SAW RF-ID tag, operating in the 1.7 GHz and 2.5 GHz frequency bands [12]. RF ID tags can be read with only miliwatt levels of RF interrogation power in 3 to 20 meter distance range at -100 °C to

over +200 °C ambient. They have a high level of radiation "hardness" under gamma-ray sterilization of medical and food products requiring sterilization with gamma radiation with good electromagnetic interference filtering.

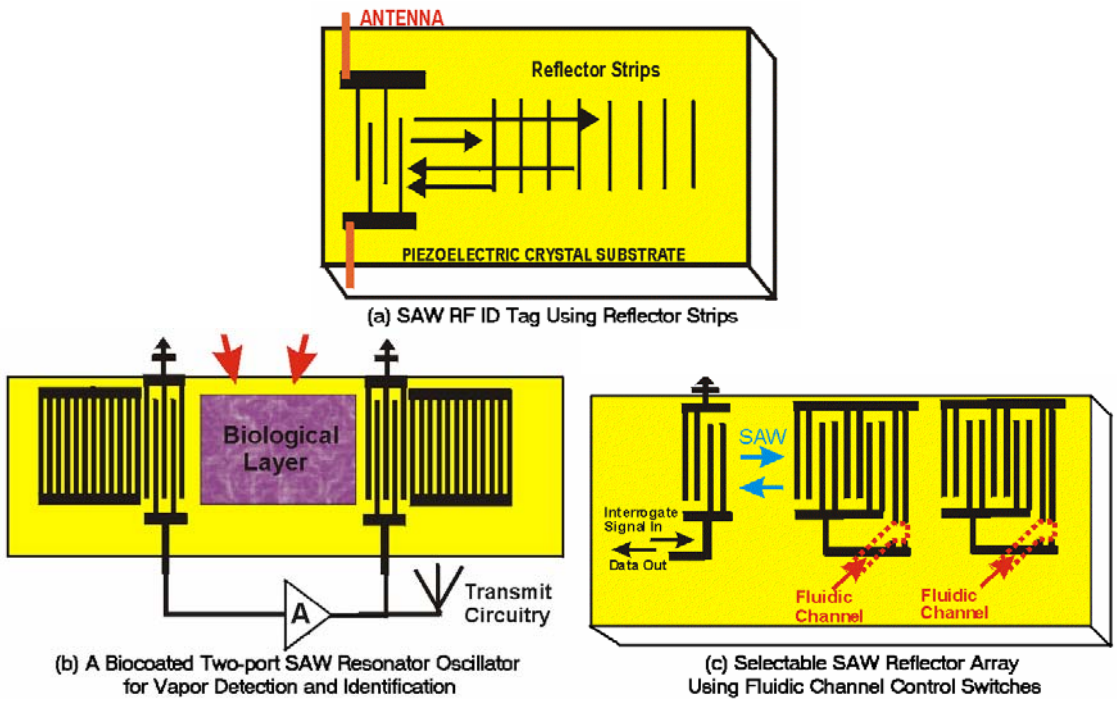


**Figure 2.4.** Some applications of SAW devices as (a) wireless sensor as SAW RF ID tag, (b) biological gas phase sensor, and (c) liquid phase sensor integrated fluidic system [12-14].

For chemical/ biochemical sensing applications, the surface of the delay path is coated with a selective coating which bonds with the target from the gas phase, as sketched in figure 2.4 (b). This causes a molecular immobilization and results in a baseline shift of the oscillator frequency. The normal linear relationship between frequency shift and mass loading of the resonator surface was studied [13]. The most common SAW sensor architecture is the dual delay line oscillator (DDLO) wherein the

effect environmental factors such temperature and stress on the sensor device can be eliminated. Figure 2.4 (c) shows the integration of SAW devices with fluidic system for liquid sensor application [14]. A fluidic channel can be built into the surface structure of a split electrode IDT, to inject a conductive fluid across a split-electrode pair, and thereby short out the IDT in question. Individual split-electrode IDT in an array of these can then be switched on or off, so that the output data from such an array resembles a pulse position modulation (PPM) type of data transfer.

For layered SAW devices, the sensitivity depends on the physical properties of the films and the substrates. ZnO based SAW delay lines can be used as detectors of combustible gases (CO, NO, $H_2$), reactive gas such as $O_2$ and other gases ($CH_4$, $N_2$, Ar) [15]. Recently, S. J. Ippolito *et al.* developed a layered surface acoustic wave (SAW) device for the monitoring of $NO_2$ and $H_2$ in synthetic air which is fabricated on XZ $LiNbO_3$ with a 1.2-μm ZnO guiding layer [16]. The sensors were tested over a range of operating temperatures between 100 and 273 °C. A large response magnitude with fast response and recovery time was observed. S. Ahmadi *et al.* developed inexpensive and miniaturized SAW gas sensors that were highly selective and sensitive [17]. These sensors were implemented with micro-electro-mechanical systems (MEMS) in CMOS technology. C-oriented thin ZnO film was grown on silicon based die. The SAW sensor chip was composed of two SAW devices fabricated on the same substrate in CMOS technology, where one device was coated with a gas absorbent polymer and the second one was sealed to serve as a reference frequency source. Love waves, which are mainly on SH-polarized guided waves, have high sensitivity in liquid. Love mode devices based on ZnO/90˚ rotated ST-cut quartz structure had large electromechanical coupling

coefficient and small temperature coefficient of frequency resulting in significantly high sensitivity [18]. S. Y. Chu *et al.* reported Love wave sensors built on ZnO/90˚ rotated ST-cut quartz system to measure viscosity and conductivity in liquid environment [19].

Recently, ZnO nanostructures have been used for the biosensor applications. Nanoscale structures can greatly enhance the sensitivity of sensors because the depletion and accumulation of carriers upon adsorption occurs in the "bulk" of the nano-scale structure, as opposed to the surface of a planar device. A novel structure consisting of ZnO nanotips grown on a $128^{o}$ Y-cut $LiNbO_3$ SAW delay line was reported by Z. Zhang *et al.* [20]. The ZnO nanotips were grown by MOCVD on the top of a $SiO_2$ layer which was deposited and patterned on the $LiNbO_3$ SAW propagation path. The ZnO nanotip arrays enhanced DNA immobilization by a factor of 200 compared to ZnO films with smooth surface. This device structure possessed the advantages of both traditional SAW sensors and ZnO nanostructures, and showed promising potential for portable sensors in biological and biomedical applications.

## 2.3 Film Bulk Acoustic Resonators and Their Applications

Bulk acoustic wave (BAW) can propagate in any direction within the propagating single-crystal piezoelectric substrate. These can have three components: namely 1) longitudinal bulk waves, 2) fast transverse shear waves, and 3) the slow transverse shear waves. Figure 2.5 shows the basics of one type of film bulk acoustic resonators (FBAR) [21]. The resonator is composed of a piezoelectric layer sandwiched by input and output electrodes, which are excited to implement mechanical resonance. High

quality epitaxial piezoelectric layer with a particular crystal axis orientation for a given piezoelectricity is deposited on top of a highly resistive wafer substrate, such as silicon.

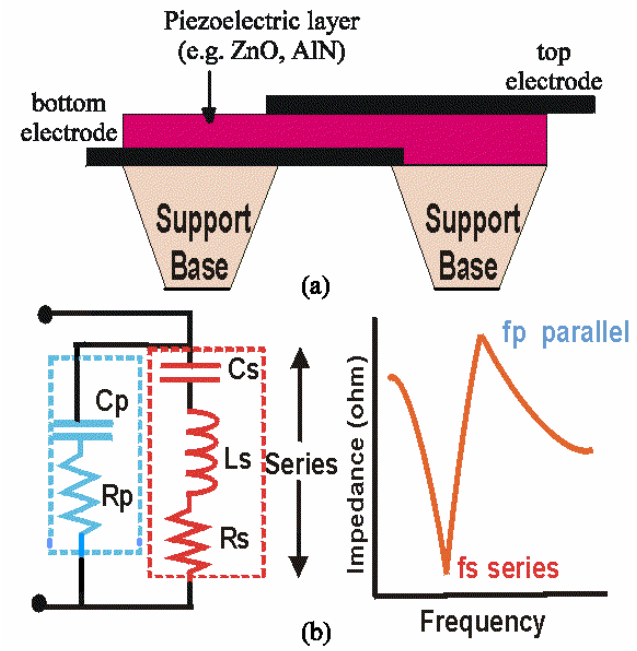


**Figure 2.5.** (a) Film bulk acoustic resonator (FBAR), (b) LCR equivalent circuit and frequency response of FBAR [21, 22].

In figure 2.5 (b), resonator equivalent parameters $C_s$, $L_s$, and $R_s$ establish the series resonance with minimum impedance at notch frequency $f_s$ [22]. But the resonator is also just a capacitor, with parallel capacitance $C_p$ and tan (delta) dissipation loss resistance $R_p$. At frequencies above $f_s$, therefore, $C_p$ and $R_p$ provide a parallel resonance with $R_s$, $L_s$, resulting in an impedance maximum at frequency $f_p$. The series resonance $f_s$ is determined by ratio of the phase velocity, $v_a$, and the thickness of the resonator, $h$:

$$f_s = \frac{v_a}{2h} \tag{2.14}$$

The series and parallel resonances are related to each other via the piezoelectric coupling coefficient, $k_t^2$. For a single piezoelectric layer without metallization:

$$k_t^2 = \frac{\pi}{2}\frac{f_s}{f_p}\tan\frac{\pi}{2}(1-\frac{f_s}{f_p}) \tag{2.15}$$

For a practical FBAR an effective coupling coefficient, $k_{eff}^2$, is defined as:

$$k_{eff}^2 = 1-\left(\frac{f_s}{f_p}\right)^2 \tag{2.16}$$

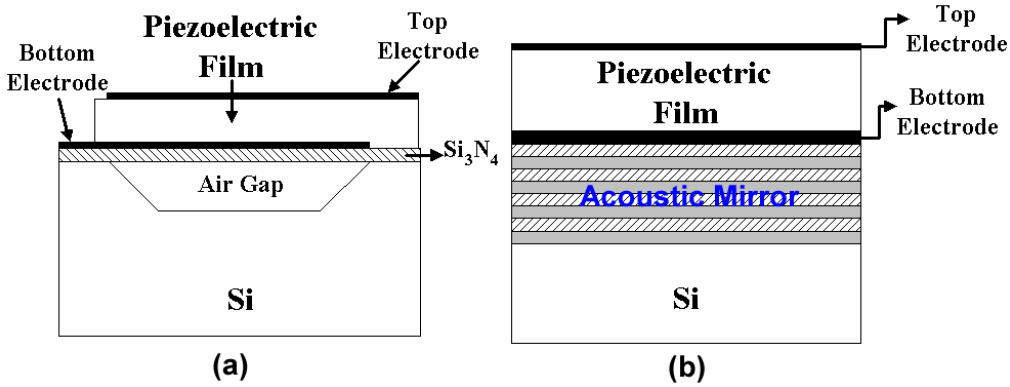


**Figure 2.6.** (a) Micromachined FBAR with air gap and (b) solidly mounted film bulk acoustic resonator (SMR).

In order to minimize mechanical damping, the resonator requires a large acoustic mismatch with outer boundaries. This is achieved by etching away the bottom substrate as sketched in figure 2.5(a), or in the design of figure 2.6(a) by air gap using micro machining or plasma etching. In contrast, the solidly mounted resonator (SMR) structure shown in figure 2.6(b) uses an acoustic mirror to isolate the FBAR from the substrate. The mirror structure is comprised of quarter wavelength reflectors, made of materials

with a large acoustic impedance difference, such as $SiO_2$ and W, Pt and ZnO. The SMR structure is attractive for monolithic integration with RF ICs with low cost and mass-manufacture.

Three important parameters to design FBAR are: i) electromechanical coupling factor ($K^2$), ii) bulk acoustic velocity ($v$), and iii) temperature coefficient of delay (TCD). Higher $K^2$ values mean larger fractional bandwidth capability. Low values of TCD are required for maintaining frequency accuracy over a wide temperature range. Zinc oxide (ZnO), aluminum nitride (AlN), and PZT ($PbZr_xTi_{1-x}O3$) are the piezoelectric materials commonly used for film bulk acoustic resonator applications [23]. ZnO has a larger $K^2$ (~ 8.5%) than AlN (~ 6.4% in an epitaxial film), while PZT has reportedly still-higher $K^2$ values. However, the TCD of ZnO (~ 60 ppm/°C) is not as good as AlN (~ 25 ppm/°C). AlN has a higher acoustic velocity (~ 10,400 m/s) than ZnO (~ 6330 m/s). A higher acoustic velocity means that the device can operate at a higher frequency using the same physical dimensions. However, it is easier to obtain high quality piezoelectric ZnO films in comparison with AlN films. Sputtering is the most common deposition technique, as piezoelectric ZnO is deposited on a metal bottom electrode on insulator ($SiO_2$ or $Si_3N_4$) structure, and therefore has no epitaxial relation with the underlying substrate.

BAW resonators, often associated with communication system applications, have many advantages, such as small size, low insertion loss and lower power consumption. Thin film bulk acoustic resonators (TFBARs) are particularly attractive as they offer the capability of monolithic integration of BAW resonators with RF ICs, leading to miniaturization, reducing circuit foot print and cost. TFBAR technology has attracted increasing interests from the mid-1980s onwards [24, 25], to meet the demands of mobile

and wireless communications. J. Kaitila *et al.* (VTT Electronics and Nokia) demonstrated SMR type ZnO TFBAR filters on glass substrates for the mobile Extended GSM (EGSM) $R_x$ band centered at 942.5 MHz [26]. Y. S. Park *et al.* reported SMR type ZnO TFBARs on Si substrates operating at 2.347 GHz for VCO applications [27]. R. Kubo *et al.* (Murata) demonstrated ZnO FBARs at 5 GHz [28]. Agilent developed AlN TFBAR based CDMA duplexers operating in the 1.85 GHz range for mobile applications, which are thinner and lighter than their ceramic counterparts [29]. A reported 5-GHz AlN FBAR had an unloaded series-resonance $Q_s$ = 913 at 5.173 GHz, with a $K^2$ x $Q_s$ product of 58 in a 5-GHz front-end ladder filter [30], suitable for 5-GHz wireless local area network (WLAN) applications.

In addition to their applications for communications, bulk acoustic wave devices have also been used in biological/chemical agent sensors. Traditional quartz crystal microbalance (QCM) sensors are known to have a limitation in achieving a higher sensitivity due to their low-frequency operation which is several MHz, and they suffer from poor integration into arrays. On the other hand, FBAR can operate at much higher frequencies. In addition, FBAR type sensors are much smaller, and can be readily integrated as arrays. Solidly mounted FBAR sensors can be fabricated on silicon, glass or other substrates using a planar technology. In the case of the Si substrate, the sensors can be integrated with other Si-based electronic components on the same substrate. Another distinct advantage of BAW sensors is that they can be used for wireless distance probing in ecological applications. The sensitivity of a BAW sensor due to the mass loading effect is calculated using the Sauerbrey's formula [31]:

$$\Delta f = -\frac{2 f_0^2}{A\sqrt{c_{66}\rho}} \Delta m = -S_f \Delta m \tag{2.17}$$

where $f_0$ is the reference resonance frequency and $f_0+\Delta f$ is the loaded frequency, $c_{66}$ is a stiffness constant of the piezoelectric material, $\rho$ is its density. In the case of ZnO, $c_{66}$ = 4.43 x $10^{10}$ N/m$^2$ and $\rho$ = 5720 kg/m$^3$.

Thin film bulk acoustic resonators have been used for gas phase and liquid phase sensing. R. Gabl *et al.* reported TFBARs for bio- and gas-detection [32-34]. Solidly mounted ZnO TFBARs with resonant frequency at 2 GHz were fabricated on Si substrates with 3-fold ZnO/Pt acoustic mirror. A schematic cross section of the ZnO TFBAR sensor is shown in figure 2.7. The active vibrating region of the resonator was coated with a receptor layer which was sensitive to the adsorption or absorption of the molecules that were to be detected. The attachment of these molecules lead to an increase of the resonator mass load and thus to a frequency shift of the resonance frequency which can electrically be determined using state of the art RF-circuitry. The quarter wavelength thick bottom electrode acted acoustically as an efficient reflection mirror and ensured a high mass sensitivity as well as a low Ohmic series resistance. The extracted electromechanical coupling coefficient $k_{eff}$ was 19%. The sensitivity reached a maximum of 2.5 Hz cm$^2$/pg, a value which was 2500 times larger compared with typical 20MHz QCM. To test the viability of TFBARs for gas sensing, a humidity absorbing polyimide from E+E Elektronik was spinned on the device surface, as shown in figure 2.7(a). A sensitivity of 6.8 kHz / % r.h. was extracted. To test the feasibility of TFBARs for bio sensing after DNA immobilization and protein coupling, TFBAR sensors with areas ranging from 150μm × 150μm to 500μm × 500μm were demonstrated, as shown in figure

2.7 (b) . The results showed that the resolution of the sensor is sufficient for detection of DNA.

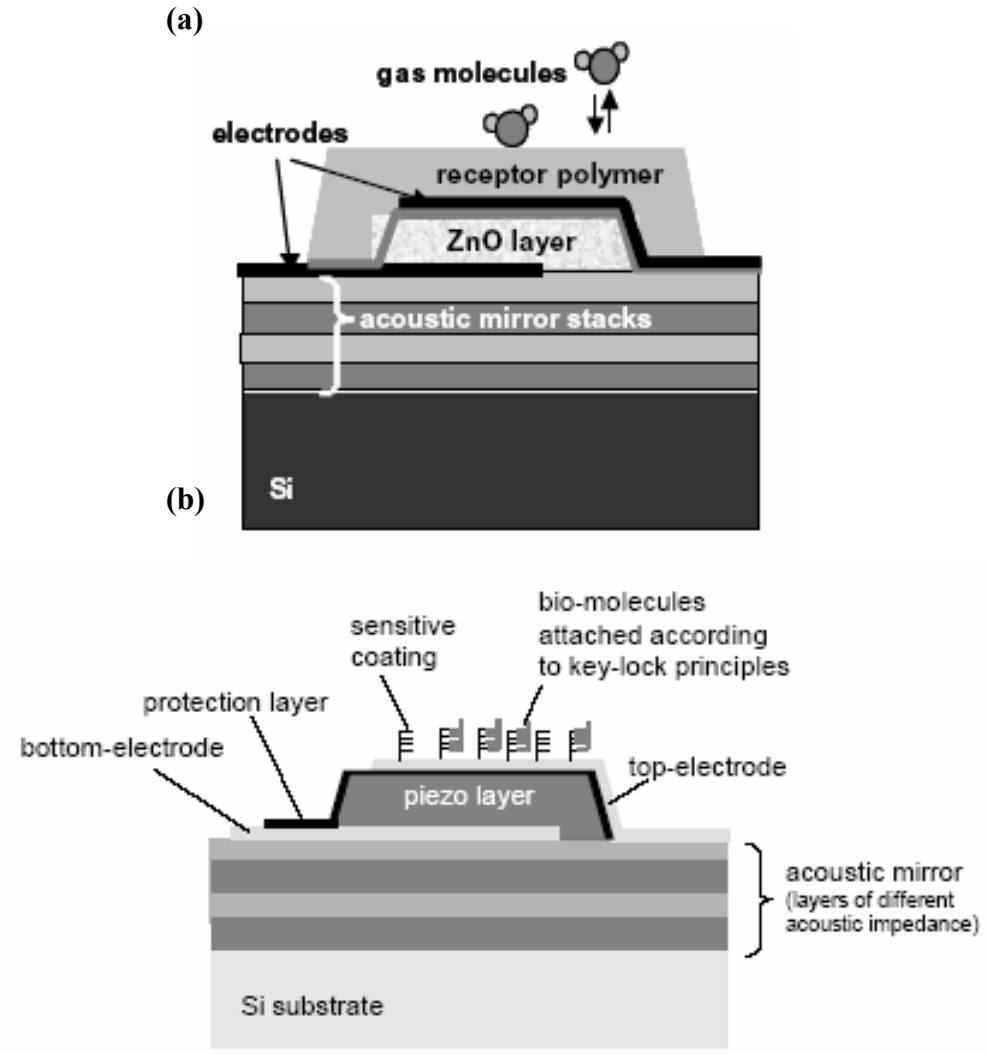


**Figure 2.7.** Schematic of the solidly mounted TFBAR used as (a) gas sensor and (b) bio sensor [32-34].

H. Zhang *et al.* [35] reported an implantable, resonant mass sensor for liquid sensing. The sensor consisted of a FBAR with a piezoelectric 1.6μm thick ZnO film and two 0.2-μm Al layers sitting on a 0.8μm silicon nitride ($Si_3N_4$) diaphragm, which formed the tip portion of an implantable silicon probe for recording neuronal activities in a living

biological tissue. With a low Q value (40) at 2 GHz, a 5 ppm resonant frequency shift was detected, corresponding to $10^{-8}$ g/cm$^2$ mass change on the sensor surface. L. Mai *et al.* demonstrated ZnO-based FBAR devices for an ultra-mass-sensitive (0.057 Hz cm$^2$/ng) sensor application [36]. When piezoelectric ZnO films are deposited on Si substrates, ZnO-based TFBAR sensors can be integrated with other electronic components on the same substrates. Furthermore, such integrated sensors are compatible with small-size microwave aerials, hence can be used for remote wireless sensing.

## 2.4 Material Properties of ZnO, $Mg_xZn_{1-x}O$, AlN, GaN, and SiC

Wide band gap semiconductor materials look increasingly attractive for many applications, where high electron mobility, high current carrying capabilities, and a high breakdown field make them superior to silicon technology. More and more, advanced research and development in microelectronics focuses on new materials that might have significant or ever overwhelming advantageous over silicon in certain applications. Recent progress in epitaxial and bulk growth of wide band gap semiconductors, such as ZnO, GaN, AlN, SiC, and related compounds, make these materials viable contenders for a variety of different applications from light emitters, electronic devices to acoustic devices for applications ranging from power electronics, low-noise microwave amplifiers, high frequency RF filters to high temperature integrated circuits and monolithic microwave integrated circuits.

ZnO is a wide bandgap material with a direct bandgap of ~3.3 eV at room temperature. ZnO has several advantages such as (i) high free exciton binding energy (~60 meV at room temperature), (ii) wet chemical processing is feasible, (iii) low-

temperature epitaxial film growth (below 400$^{o}$C), (iv) high radiation hardness, and (v) single crystalline and well-aligned ZnO nanostructures can be grown on various substrates at low temperatures. ZnO belongs to the hexagonal wurtzite crystal class, with c=5.2069Å and a=3.2495Å. With such properties, ZnO has many applications including optoelectronic devices, acoustic wave devices, piezoelectric MEMS actuators, and sensors. The as-grown ZnO film is usually n-type semiconductor, due to crystal defects [37, 38]. Through proper doping, ZnO film can be made transparent and conducting, piezoelectric, and ferromagnetic. Al-doped or Ga-doped ZnO films were used as transparent electrode in the field of light emitting diode and solar cells [39, 40]. Transition metals (TM), such as Co, Mn and Fe, were reported to dope into ZnO and realize the room-temperature diluted ferromagnetic semiconductor for novel spintronics applications [41-44]. To achieve piezoelectric ZnO films, compensation doping using Li, Ni and Cu were used [45-47].

ZnO is well known as a piezoelectric material used for SAW and BAW devices in wireless communication and signal processing. Piezoelectric ZnO thin films were used in conjunction with low loss and high acoustic velocity substrates, such as sapphire ($Al_2O_3$) [48,49], SiC [50], and diamond [51,52]; with semiconductors, such as Si [53,54] and GaAs [55,56]; and with low coupling coefficient piezoelectric materials, such as quartz [57,58]. Temperature compensated SAW devices were fabricated using ZnO on glass for TV-IF filters [59,60]. ZnO thin films deposited on GaAs [61] and on InP [62] were also used for acousto-optic modulators, where acoustic waves were used to modulate optical signals. ZnO films were used on GaAs to fabricate acoustic charge transport (ACT) devices [63].

Several important parameters associated with the piezoelectricity of ZnO are listed below:

**a) ZnO dielectric coefficients under the constant strain:**

$$\begin{bmatrix} \varepsilon_{11} & 0 & 0 \\ 0 & \varepsilon_{11} & 0 \\ 0 & 0 & \varepsilon_{33} \end{bmatrix} \tag{2.18}$$

**b) ZnO stiffness coefficients ($10^{10}$ N/m$^2$):**

$$\begin{bmatrix} c_{11} & c_{12} & c_{13} & 0 & 0 & 0 \\ c_{12} & c_{11} & c_{13} & 0 & 0 & 0 \\ c_{13} & c_{13} & c_{33} & 0 & 0 & 0 \\ 0 & 0 & 0 & c_{44} & 0 & 0 \\ 0 & 0 & 0 & 0 & c_{44} & 0 \\ 0 & 0 & 0 & 0 & 0 & c_{66} \end{bmatrix}, \text{ where } c_{66} = (c_{11} - c_{12})/2 \tag{2.19}$$

**c) ZnO piezoelectric stress constants (C/m$^3$)**

$$\begin{bmatrix} 0 & 0 & 0 & 0 & e_{15} & 0 \\ 0 & 0 & 0 & e_{15} & 0 & 0 \\ e_{31} & e_{31} & e_{33} & 0 & 0 & 0 \end{bmatrix} \tag{2.20}$$

**d) ZnO piezoelectric strain coefficients ($10^{-12}$ C/N)**

$$\begin{bmatrix} 0 & 0 & 0 & 0 & d_{15} & 0 \\ 0 & 0 & 0 & d_{15} & 0 & 0 \\ d_{31} & d_{31} & d_{33} & 0 & 0 & 0 \end{bmatrix} \tag{2.21}$$

The dielectric constants, elastic stiffness, piezoelectric constants, and density of bulk ZnO and film ZnO are shown in table 2.1.

**Table 2.1.** Material constants of film and bulk ZnO [64-67].

| **Property** | | **ZnO Film** | **ZnO Bulk** |
|---|---|---|---|
| **Density ($kg/m^3$)** | $\rho$ | 5720 | 5665 |
| **Elastic stiffness (GPa)** | $c_{11}$ | 157 | 207.0 |
| | $c_{12}$ | 89 | 117.7 |
| | $c_{13}$ | 83 | 106.1 |
| | $c_{33}$ | 208 | 209.5 |
| | $c_{44}$ | 38 | 44.8 |
| | $c_{66}$ | 34 | 44.65 |
| **Piezoelectric Constant ($C/m^2$)** | $e_{15}$ | -0.45 | -0.48 |
| | $e_{31}$ | -0.51 | -0.57 |
| | $e_{33}$ | 1.22 | 1.321 |
| **Dielectric Permittivity** | $\varepsilon_{11}$ | 7.46 | 7.77 |
| | $\varepsilon_{33}$ | 8.59 | 8.91 |

Alloying ZnO with MgO forms the ternary compound semiconductor $Mg_xZn_{1-x}O$, which has a wider bandgap than ZnO. Cubic MgO has a bandgap of 7.8 eV. The range of direct band gap energies obtainable is limited by the solubility limit of MgO in ZnO. MgO has a NaCl-type structure, which consists of interpenetrating face centered cubic

(f.c.c) Mg and O sub-lattices, while ZnO has a wurtzite structure, which consists of interpenetrating hexagonal close packed (h.c.p) Zn and O sub-lattices. The maximum thermodynamic solubility limit of Mg in ZnO is < 5% (at around 1800°C). In spite of this low equilibrium solubility limit, sputtering, pulsed laser deposition (PLD) and laser-assisted molecular beam epitaxy (MBE) system were used to achieve wurtzite $Mg_xZn_{1-x}O$ films with up to 36% Mg content [68-70], and $Mg_xZn_{1-x}O$ films with 15% Mg content were reported to be stable at temperatures up to 700°C. Sputtering deposited $Mg_xZn_{1-x}O$ films were also reported [71,72]. Using the reported solubility limit for MgO in ZnO with wurtzite phase, the band gap of $Mg_xZn_{1-x}O$ alloy is tunable from 3.36 eV (x = 0) to 4.05 eV (x = 0.35). MgO is a non-piezoelectric material with a rock-salt cubic structure, while piezoelectric ZnO has a wurtzite crystal structure. $Mg_xZn_{1-x}O$ is a piezoelectric material with Mg composition less than 35% (x<35%) [73,74], because the $Mg_xZn_{1-x}O$ (x<35%) crystal has a wurtzite structure. Compared with ZnO, MgO has higher bulk acoustic wave velocities. Therefore, $Mg_xZn_{1-x}O$'s acoustic velocity increases and its piezoelectric coupling coefficient decreases as the Mg content increases, within the piezoelectric range. This allows for piezoelectric device design flexibility, as acoustic wave properties can be tailored by controlling Mg content as well as using $ZnO/Mg_xZn_{1-x}O$ multilayer structures.

High-frequency and low-loss SAW devices using higher order wave modes in layered structures have important applications in communications. It can be achieved by depositing thin piezoelectric films on high acoustic velocity substrates. The efficient generation of Rayleigh waves on these layered structures has allowed SAW devices to impact a wide variety of frequency control systems requiring higher frequency, low loss and temperature stability. Examples include ZnO, GaN, AlN and $Al_xGa_{1-x}N$ thin films on

sapphire, SiC, and diamond substrates. The $SiO_2$/ZnO/diamond structure, which can provide a high acoustic velocity (~$10^4$m/s), a zero temperature coefficient of frequency and a large $K^2$ (~1.2 %), is promising for high-frequency and narrow-band devices, such as resonators and retiming filters for optical communication systems [75]. Extremely high velocity SAW modes with moderate coupling coefficient in AlN and GaN thin films deposited on SiC, diamond or sapphire substrates can be used for gigahertz-band mobile communication applications [76-78]. On the other hand, ZnO films on high-velocity and low-loss substrates, such as sapphire, diamond and SiC, have large-coupling factor, higher-order generalized SAW modes and high-velocity Pseudo-SAW (HVPSAW) modes. For example, high effective coupling coefficient (6%) of the Sezawa wave in ZnO/r-$Al_2O_3$ can be achieved [79]. The Sezawa wave of ZnO/r-sapphire structure was used for low insertion loss SAW filters in the 1.5GHz to 2.5GHz band [80]. Furthermore, these wide band gap materials (ZnO, GaN and AlN) imply a potential for new types of sensors and signal processing devices, in which the optical, electronic, and acoustic features are hybridized. For example, the integration of a SAW device with a metal-semiconductor-metal UV photodetector was demonstrated using AlGaN epilayers on c-plane sapphire [81] and ZnO epilayers on $LiNbO_3$ substrates [82].

AlN (6.2eV), GaN (3.4 eV) and their ternary alloy $Al_xGa_{1-x}N$ have been developed for optoelectronic devices [83], high-power transistors [84], and SAW applications [85]. GaN has become a mainstream wide bandgap semiconductor for fabricating UV/blue LEDs [86]. Many important applications with huge market potential, including new solid-state light sources and displays, are currently under enormous efforts in R&D. Epitaxial grown crystalline AlN and GaN have also been used for SAW devices

and FBARs because of their piezoelectric properties. AlN and GaN have high acoustic velocities and moderate electromechanical coupling coefficients. The AlN/c-$Al_2O_3$ structure had a high SAW velocity of 5,910m/s, a electromechanical coupling coefficient $K^2$ of about 0.3%, and zero-temperature-coefficient-of-delay with proper control of AlN thickness [87, 88]. SAW devices on GaN/c-sapphire with a high velocity of 5803 m/s, relatively low insertion loss of -7.7 dB, and temperature coefficient of frequency of -18.3 ppm/°C in the range of -25 to 50°C were demonstrated [89,90]. The calculated $K^2$ was about 4.36±0.3% for the 2 μm-thick Mg-doped GaN film on c-sapphire. In spite of these developments, several challenges remain for GaN technology, such as relatively high density of defects in GaN films for laser applications, difficult and high temperature deposition processes, non-availability of large size bulk crystals, and difficulty in wet chemical etching.

SiC has outstanding material properties including a large Young's Modulus, excellent physical stability and thermal conductivity. It can survive in harsh conditions and still provide both mechanical and electronic functionality. SiC is more suitable for high temperature gas-sensing application in harsh environments over long periods. Many sensors are based on silicon substrates whose operating temperature is limited to temperatures below 250 ˚C, rendering them incapable of being used for gas-sensing applications in harsh environments over long periods. For instance, automotive exhaust sensors for cylinder specific combustion engine control should be capable of operating at 700 ˚C for at least 4000 h. Schottky diode gas sensors based on SiC substrate can provide rapid detection of low gas concentrations (less than 5 ppm) and can operate at temperature as high as 900 ˚C [91]. The hydrogen and hydrocarbon gases dissociating on

the catalytic metal surface and diffuse through the metal/semiconductor interface results in a dipole layer that changes the Schottky diode's electrical properties in proportion to the concentration of gas. The current focus of SiC-based Schottky diode gas sensors are metal-reactive insulator-SiC (MRISiC) devices which can offer increased sensitivity, selectivity and stability. For example, Pt/$Ga_2O_3$-ZnO/SiC Schottky diode-based hydrocarbon gas sensor were reported [92]. The magnitude of the response of the sensor increased with temperature from 375 ˚C to 525 ˚C. The change in output voltage was directly proportional to the change in propene concentration (oxygen content of the ambient gas mixture) when the forward bias current was fixed at 2 and 8 mA. Kalantar-zadeh *et al.* reported the gas-sensing properties of ZnO toward hydrocarbons, whereby it was found that the material proved to be highly sensitive to concentrations of propane below 100 ppm [93].

The SAW propagation properties of ZnO films on SiC were theoretically and experimentally characterized in the film thickness-to-acoustic wavelength ratio range up to 0.12 [50, 94]. The experimental characterization of the SAW propagation properties was performed with a linear array of IDT structures. The measurements characterized the velocity and propagation loss of two wave modes, a generalized SAW mode with velocities between 6000 to 7000 m/s, and a high velocity pseudo-SAW (HVPSAW) mode with velocities between 8500 to 125000 m/s. The highest piezoelectric coupling of 5.2% was theoretically predicted for the first GSAW mode and for the electrode configuration with the IDT at the film-substrate interface and metallized upper surface.

In order to develop high frequency and low-loss SAW devices, piezoelectricity in ZnO based multilayer structures are investigated, including phase velocity and

electromechanical coupling coefficients. Table 2.2 lists the crystal structure and lattice parameters of ZnO, MgO, AlN, GaN, SiC, and $Al_2O_3$ [95-97].

**Table 2.2**. Crystal structure and lattice parameters of ZnO, MgO, AlN, GaN, SiC, and $Al_2O_3$ [95-97].

| **Crystal** | **Structure** | **Lattice Parameter (Å)** |
|---|---|---|
| ZnO | Wurtzite (hexagonal) | a = 3.249 c = 5.206 |
| MgO | Rock Salt | a = 4.21 |
| AlN | Wurtzite (hexagonal) | a = 3.11 c = 4.98 |
| GaN | Wurtzite (hexagonal) | a = 3.189 c = 5.185 |
| SiC | Wurtzite (hexagonal) | a = 3.0817 c = 15.1183 |
| $Al_2O_3$ | Corundum (rhombohedral) | a = 4.758 c = 12.992 |

Table 2.3 gives the density, elastic stiffness, piezoelectric constants, and dielectric constants, of MgO, AlN, GaN, SiC, and $Al_2O_3$ [1,65,98]. Table 2.4 shows average values of the longitudinal and shear bulk acoustic wave velocities [99] and corresponding propagation loss values [100-102] in decibels per centimeter of high velocity and low loss substrates.

**Table 2.3.** Material constants of MgO, AlN, GaN, SiC-6H, and $Al_2O_3$ [1, 65, 98].

| **Property** | | **MgO** | **AlN** | **GaN** | **SiC-6H** | **$Al_2O_3$** |
|---|---|---|---|---|---|---|
| **Density ($kg/m^3$)** | $\rho$ | 3650 | 3255 | 6095 | 3211 | 3980 |
| **Elastic stiffness (Gpa)** | $c_{11}$ | 286 | 411 | 374 | 500 | 197 |
| | $c_{12}$ | 87 | 149 | 106 | 92 | 164 |
| | $c_{13}$ | | 99 | 70 | 0 | 111 |
| | $c_{33}$ | | 389 | 379 | 564 | 498 |
| | $c_{44}$ | 148 | 125 | 101 | 168 | 147 |
| | $c_{66}$ | | 131 | 134 | 204 | 166.5 |
| **Piezoelectric Constant ($C/m^2$)** | $e_{31}$ | 0 | -0.58 | -0.2 | 0.08 | 0 |
| | $e_{33}$ | 0 | 1.55 | 0.29 | 0.2 | 0 |
| **Dielectric Permittivity** | $\varepsilon_{11}$ | 9.6 | 9 | 9.5 | 6.7 | 8.28 |
| | $\varepsilon_{33}$ | | 11 | 10.4 | 6.52 | 10.2 |

**Table 2.4.** Average bulk-wave longitudinal (L) velocity, and Shear (S) velocity and average propagation loss at 1.0 GHz [99-102].

| Substrate | L-velocity (m/s) | S-velocity (m/s) | L-Loss (dB/cm) | S-Loss (dB/cm) |
|---|---|---|---|---|
| **Silicon** | 9050 | 5420 | 8.3 | 3.0 |
| **Sapphire** | 11000 | 7000 | 0.2 | 0.5 |
| **SiC** | 12500 | 7250 | 0.4 | 0.3 |
| **Diamond** | 18000 | 11000 | 0.6 | 0.3 |

## 2.5 Sputtering Deposition of Piezoelectric ZnO Films

The most common techniques used for depositing piezoelectric ZnO films are pulse laser deposition (PLD) [103,104], metalorganic chemical vapor deposition (MOCVD) [45,105,106], and sputtering [48]. MOCVD growth technologies result in the excellent epitaxial quality and in-situ modulation doping capability. However, the as-grown ZnO films generally show the n-type semiconducting properties, due to the oxygen vacancies and Zn interstitials, as well as other defects and impurities. In order to effectively stimulate the piezoelectric effect, this n-type conductivity has to be compensated. This requires very heavy doping, which can be difficult for MOCVD technologies. Therefore, a post-growth diffusion step is frequently used to achieve piezoelectric ZnO films grown by MOCVD. Sputtering is the common production scale deposition method, due to its relative ease of use and low cost. Sputtering targets can be made to contain the compensated doping species, such as Li, Ni, Cu, etc. T. Mitsuyu *et al.*

added $Li_2CO_3$ to ZnO targets (purity, 99.9%) before the sintering process, in order to obtain high resistivity films [48]. H. Ieki *et al.* obtained a Ni-doped ZnO target by mixing the appropriate quantities of 99.995% pure ZnO powder with 1 ~ 2 % wt NiO power before the sintering process [46]. Therefore, piezoelectricity excitation can be obtained in sputtered ZnO films without post-deposition diffusion.

Sputtering is a popular deposition technique, as it is able to obtain a large size, well-oriented and uniform ZnO films even on amorphous substrates at high deposition rates. On the other hand, sputtering is an economical and relatively fast deposition technique, in particular it has advantage in depositing heavily doped and alloyed ZnO films, which is difficult to accomplish with MOCVD technique due to limited availability of MO-precursors as well as solubility limitations of dopants in equilibrium MOCVD growth. Sputtering as a physical deposition technique is capable of depositing thick piezoelectric ZnO layer with high compensation doping.

Piezoelectric ZnO films have been deposited on various substrates. S. J. Chang *et al.* reported piezoelectric ZnO thin films which were deposited on (100)-oriented InP substrates by RF-magnetron sputtering [107]. An undoped and high purity ZnO target was used for the deposition. The best sputtering condition to achieve a small XRD FWHM of 0.183°, was at room temperature with 200 W RF power, and mTorr gas pressure with a gas ratio of $Ar:O_2 = 2:1$. The resistivity of the deposited films reached $10^{10}$ Ωcm and their refractive index was close to that of bulk ZnO. ZnO/InP based SAW devices were then successfully fabricated [62]. M. Katoda *et al.* reported that ZnO films deposited by electron cyclotron resonance (ECR) sputtering systems showed excellent piezoelectric properties and c-axis orientation [59]. The ECR sputtering system added

magnets to the outside of a cylindrical zinc metal (Zn) target. There was no evidence of column and fiber grains in the cross section of the ZnO films. A ZnO on interdigital transducer (IDT)/glass structure was able to drive a 1.1 GHz fundamental Rayleigh SAW. J. Lee *et al.* deposited ZnO thin films on $SiO_2$/Si(100) substrates by RF planar magnetron sputtering using two-step fabrication methods for SAW applications: the first deposition with argon only for 30 min at 100 W and the second deposition with oxygen in the range $O_2/(Ar+O_2)$ up to 50% [108]. In comparison with films deposited by the one-step fabrication method, these films exhibited a lower insertion loss and a closer agreement between experimental coupling coefficients and the theoretical values. Post-deposition annealing plays an important role in improving the structural and electrical properties of piezoelectric ZnO films. S. Y. Chu *et al*. reported the post-deposition annealing effects on ZnO film quality [109]. When the deposited ZnO films were annealed for 1 hour at 400 °C in vacuum, the stress was relieved, resistivity was increased by one order of magnitude, and the loss factor was kept at minimum. When annealing at 600 °C and above, the loss factor and stress were found to increase. The interface between piezoelectric ZnO films and the substrates, and interface between ZnO film and metal electrodes, are critical important for SAW and BAW device performances. Y. Yoshino *et al.* studied the microstructures of ZnO/substrate interfaces [110]. It was found that an amorphous layer existed at the ZnO/glass interface, while a thicker amorphous layer existed at the ZnO/Al interface. No amorphous layer was observed at the ZnO/Au and ZnO/sapphire interfaces, and direct orientation of ZnO thin films began at the interface of both these substrates. $(01\bar{1}2)$ plane epitaxial ZnO films were deposited on r-plane sapphire substrate at 250 ~ 550 ° by the ECR sputtering process [111]. The ZnO films

deposited on glass or sapphire substrates had a high electrical resistivity ($\rho > 10^{10}$ Ωcm) and strongly generated higher-frequency SAWs with a large electromechanical coupling factor for the Sezawa mode.

## 2.5 Summary

In this chapter, an overview of technical background is presented. The following topics are included: (1) piezoelectricity, (2) surface acoustic wave (SAW) devices and their applications, (3) film bulk acoustic resonators (FBAR) and their applications, (4) material properties of ZnO, $Mg_xZn_{1-x}O$, AlN, GaN, and SiC, and (5) sputtering deposition of piezoelectric ZnO film. In the first part, basic concepts and general equations of piezoelectricity are briefly presented. In the second part, we briefly introduce the principle of SAW devices. The applications of SAW devices in communication and sensor areas are reviewed. Another important acoustic wave device, FBAR, is introduced in the third part. The advantages and applications of FBAR in sensors are also reviewed. In the fourth part, wide bandgap semiconductors (ZnO, AlN, GaN, and SiC) for acoustic wave applications are discussed. The material constants, including dielectric constants, elastic stiffness, piezoelectric constants, and density, are summarized. Finally, we reviewed piezoelectric ZnO film deposition using sputtering technology. The following part of this dissertation will focus on piezoelectricity study in ZnO based multilayer structure for sensor application. High-frequency, low-loss SAW devices can be achieved by depositing ZnO films on AlN, GaN, r-sapphire, and SiC.

# CHAPTER III. TAILORING OF SAW PROPERTIES IN $ZnO/Al_xGa_{1-x}N/c\text{-}Al_2O_3$

High-frequency and low-loss SAW devices can be achieved by depositing thin piezoelectric films on high acoustic velocity substrates. The efficient generation of the surface acoustic waves on these layered structures has allowed SAW devices to impact a wide variety of frequency control systems requiring high frequency, low loss and temperature stability. By combining ZnO and $Al_xGa_{1-x}N/c\text{-}Al_2O_3$ ($0 \leq x \leq 1$), higher order wave modes with large coupling coefficient and high acoustic velocity can be obtained. In this chapter, ZnO films were deposited on $Al_xGa_{1-x}N/c\text{-}Al_2O_3$ using RF sputtering technique. The SAW properties in $ZnO/Al_xGa_{1-x}N/c\text{-}Al_2O_3$ multilayer structures were analyzed using multilayer transfer matrix method. The experimental SAW velocities obtained from test devices were compared with simulation results. The ZnO/AlGaN hybrid structures combine the strengths of ZnO and AlGaN to obtain unique material properties for developing new tunable acousto-opto-electronic devices.

## 3.1. Deposition of Piezoelectric ZnO Films on $Al_xGa_{1-x}N/c\text{-}Al_2O_3$

Piezoelectric AlN and ternary $Al_xGa_{1-x}N$ thin films deposited on (0001) c-plane sapphire substrates using CVD are attractive for low-loss and high frequency surface acoustic wave devices [90]. However, CVD growth of good quality epitaxial AlN films is difficult due to its high temperature and low deposition rate. Piezoelectric ZnO thin films are attractive due to their high electromechanical coupling coefficients. Furthermore, high quality epitaxial ZnO films can be grown at temperatures hundreds of degrees lower than

AlN. Additionally, ZnO and $Al_xGa_{1-x}N$ are wide band gap semiconductors which have broad applications in electronic, optoelectronic and acoustic devices. The combination of ZnO and $Al_xGa_{1-x}N$ provides the potential applications for integration of optoelectronic and acoustic devices.

The undoped $Al_xGa_{1-x}N$ ($0 \leq x \leq 1$) samples were grown on c-plane sapphire substrates (miscut 0.2 degrees towards m-plane) using Veeco D-180GaN (6x2") and D-125GaN (3x2") MOCVD reactors (Veeco TurboDisc, NJ). Precursors for the growth were trimethylgallium, trimethyaluminium, and ammonia. A 150Å AlN buffer was first deposited at 600°C to serve as a buffer layer. Then the growth temperature was raised to 1100ºC for the deposition of $Al_xGa_{1-x}N$ films. Typical growth rates were around 0.5μm/hr.

Sputtering has been the most popular technology for depositing piezoelectric ZnO films for acoustic applications [48, 112]. In this work, piezoelectric ZnO thin films with various thicknesses (0.4μm ~ 1.4μm) were deposited on $Al_xGa_{1-x}N$/c-$Al_2O_3$ ($0 \leq x \leq 1$) using the RF sputtering technique. The targets were prepared by mixing pure ZnO with 2%wt NiO. Ni doping was used to achieve piezoelectricity [46]. As shown in figure 3.1, the sputtering system chamber is equipped with a standard RF power source on the bottom and a substrate holder, substrate heater and substrate rotator on the top. Ar and $O_2$ gases were fed into the chamber from the side. The chamber was maintained at a vacuum level of $5x10^{-6}$ torr before deposition. A mixture of 1:1 Ar and $O_2$ was fed into the chamber during the ZnO deposition. The deposition pressure of the chamber was maintained at $7x10^{-3}$ torr. The substrate temperature was kept at 400 ˚C. In order to achieve better crystal quality and surface morphology, a 200 Å buffer layer was first deposited at a low deposition rate, followed by a higher deposition rate about 0.7μm/hour.

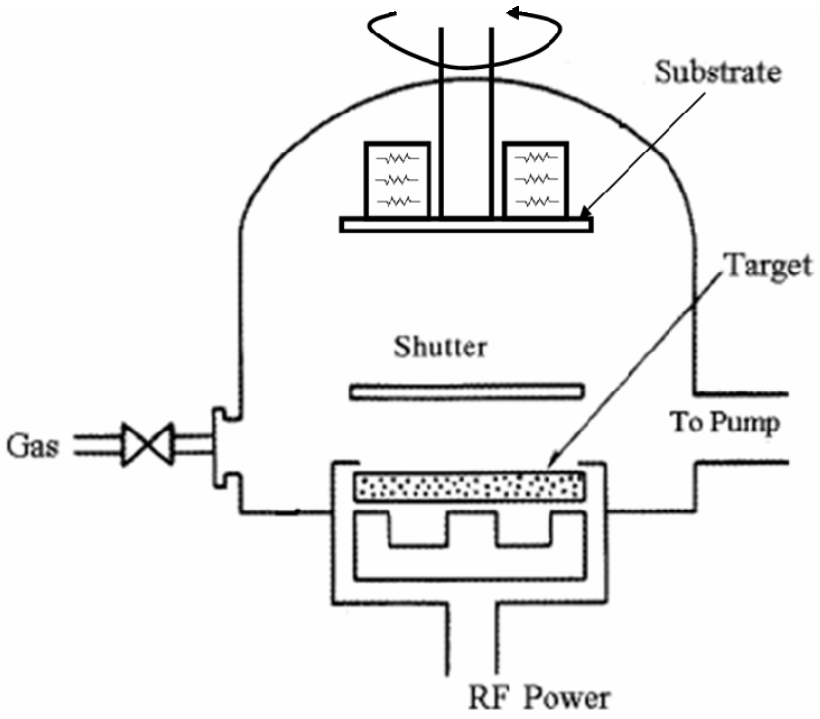


**Figure 3.1.** A schematic diagram of an RF sputtering system in Rutgers MERL.

Piezoelectric ZnO films were characterized for structure, morphology and orientation. A Leo-Zeiss field emission scanning electron microscopy (FESEM) was used for analyzing the surface morphology of the deposited films. A ZnO film deposited on AlN/c-$Al_2O_3$ template (figure 3.2(a)) with a relatively smooth surface is shown in figure 3.2 (b), which is promising to reduce scattering loss as well as for device fabrication. FESEM images show dense and uniform deposition of ZnO films on the samples ($Al_xGa_{1-x}N$ on c-sapphire, $0 \leq x \leq 1$).

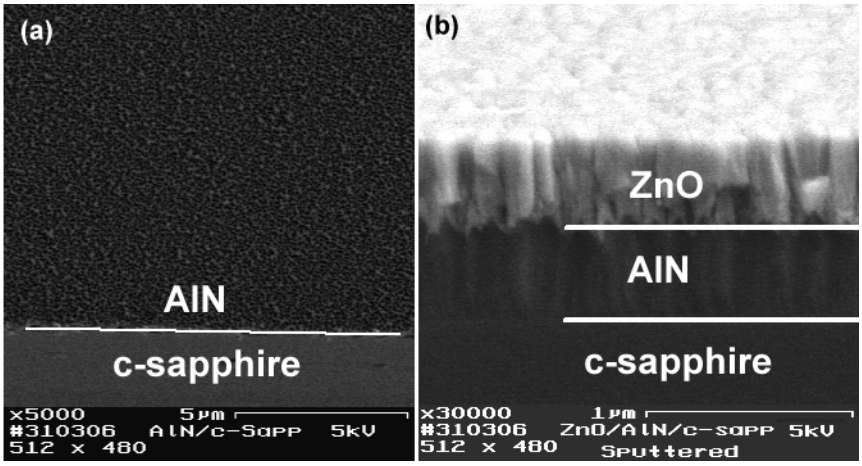


**Figure 3.2**. SEM Imagines of (a) AlN/c-$Al_2O_3$; (b) ZnO/AlN/c-$Al_2O_3$ deposited by RF sputtering system.

X-ray diffraction (XRD) analysis was done using a Siemens D500 Thin Film X-ray diffractometer unit, with monochromated Cu $K\alpha_1$ radiation. XRD scans indicate that the as-grown ZnO films have a predominantly c-orientation with c-axis normal to the surface of the $Al_xGa_{1-x}N$ ($0 \leq x \leq 1$) /c-$Al_2O_3$ substrate. Figure 3.3 (a), (b) and (c) show the x-ray (θ-2θ) scans of samples with piezoelectric ZnO films deposited on GaN, $Al_{0.6}Ga_{0.4}N$/AlN, and AlN films on c-sapphire substrates, respectively. All the scans show the ZnO (002) and (004) peaks, in addition to the peaks from the layers in the template. This indicates that the ZnO films on all the templates are preferably c-axis oriented. The (002) peak of ZnO is found to overlap with the GaN (002) peak (figure 3.3 (a)), due to the small difference between the c-lattice parameters of ZnO (5.20 Å) and GaN (5.18 Å). Figure 3.3 (b) shows the scan of a ZnO film on $Al_{0.6}Ga_{0.4}N$/AlN/c-$Al_2O_3$ (AlN as growth buffer layer). The AlN (002) peak in figure 3.3(c) is shifted towards the right compared to the ZnO (002) peak, due to the lower c-lattice parameter of AlN (4.98 Å). The $Al_{0.6}Ga_{0.4}N$ peak is between the θ-2θ peak positions for GaN and AlN, due to relatively

linear variation of c-lattice parameter with Al composition, with the hexagonal crystal structure being retained during incorporation of Ga in AlN.

## 3.2 SAW Propagation in $Al_xGa_{1-x}N$/c-$Al_2O_3$ and ZnO/c-$Al_2O_3$

Piezoelectric thin films on high velocity substrates possess dispersive characteristics and provide flexibility for SAW filter design in various applications. In the multilayer structures, not only acoustic velocity and piezoelectric coupling coefficient can be functions of the film-thickness ($h$) to wavelength ($\lambda$) ratio ($h/\lambda$) but also high-coupling factor, higher-order generalized SAW modes and high velocity Pseudo-SAW modes can be excited.

In general, there will be velocity dispersion in a material system composed of a thin film layer on a substrate, when the film has a slower acoustic velocity compared to the substrate. The energy of a SAW decays exponentially with depth, and is thus mostly confined within one wavelength of the surface. Therefore, in a system composed of a high SAW velocity substrate and a thin film with a slower acoustic velocity, when $h/\lambda$ is small (i.e. wavelength is much larger than the film thickness), most of the energy is transported in the substrate. As a result, the acoustic velocity will be slower than, but close to, the substrate velocity. When $h/\lambda$ is approximately equal to 1, most of the energy is trapped within the film itself. And the velocity will be close to, but somewhat larger than, the film velocity. When $h/\lambda$ is much greater than 1, almost all of the energy is trapped within the film, and the thin film can practically be viewed as the sole transport layer. Acoustic velocity is the thin film acoustic velocity.

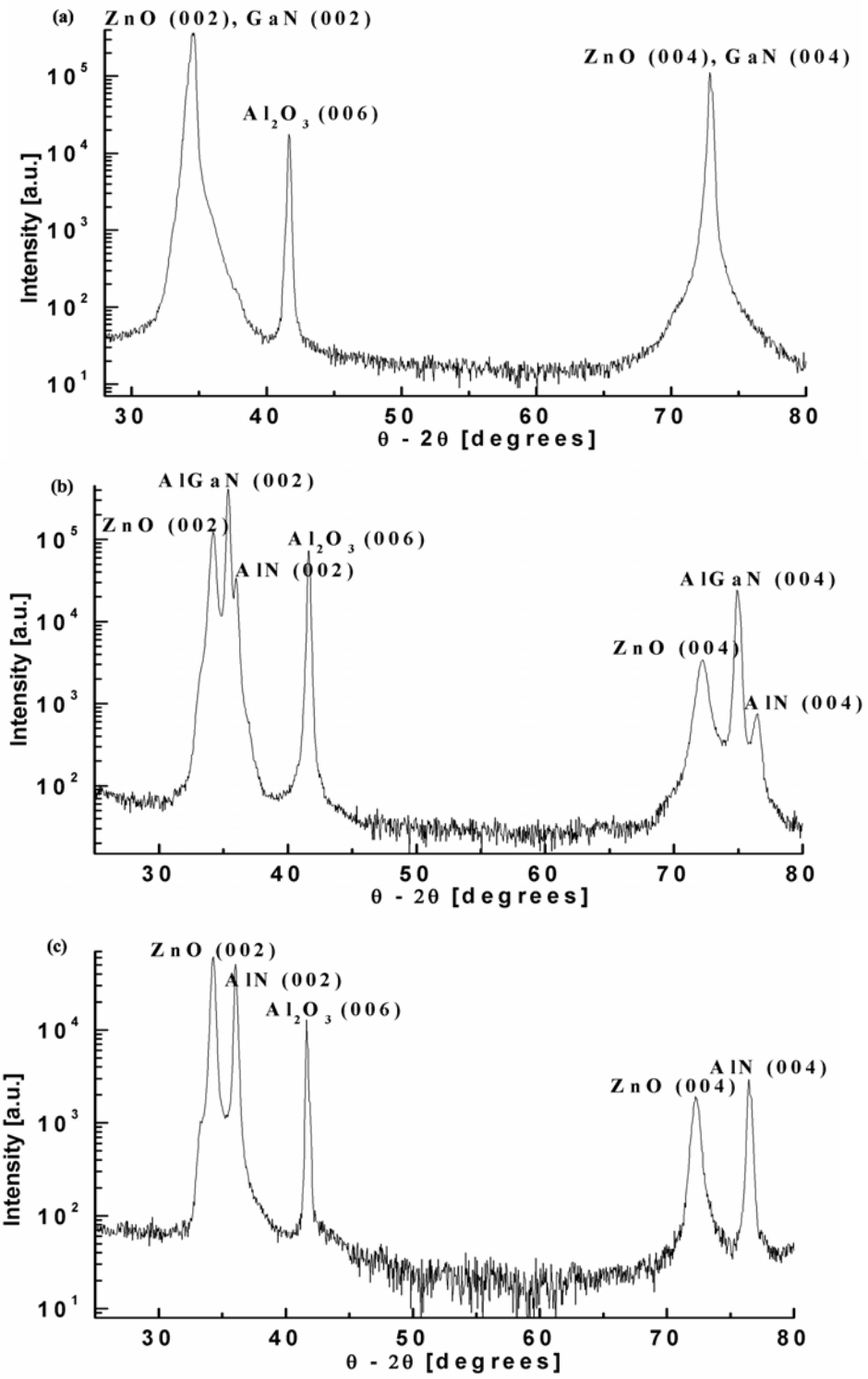


**Figure 3.3.** XRD (θ-2θ) scans of ZnO/$Al_xGa_{1-x}N$/c-$Al_2O_3$ structures, (a) ZnO (34.5°) on GaN (34.6°); (b) ZnO (34.2°) on $Al_{0.6}Ga_{0.4}N$ (35.4°); (c) ZnO (34.3°) on AlN (36.05°) on c-sapphire substrates.

The SAW properties of the $ZnO/Al_xGa_{1-x}N$ ($0 \leq x \leq 1$)/c-$Al_2O_3$ structures, including acoustic velocity ($v$) and electromechanical coupling coefficient ($K^2$), were simulated using Adler's transfer matrix method [113]. In Adler's transfer matrix method, the piezoelectric equations of state are presented in matrix format. The reference axes for the layered material structure are shown in figure 3.4. $x_1$ is the direction of propagation, while the different layers are stacked in the $x_3$ direction. No propagation is assumed in the $x_2$ direction, which is normal to the page. The equations of state – containing the variables **T**, the stress tensor, **v**, particle velocity vector**,** $D_3$, the surface normal component of the dielectric displacement vector, and $\Phi$, the potential associated with the acoustic wave – are expressed in matrix form as:

$$\frac{d\boldsymbol{\tau}}{dx_3} = j\omega \mathbf{A}\boldsymbol{\tau} \tag{3.1.a}$$

where $\boldsymbol{\tau}$ is the state vector:

$$\boldsymbol{\tau} = \begin{bmatrix} T_{13} & T_{23} & T_{33} & D_3 & v_1 & v_2 & v_3 & j\omega\phi \end{bmatrix}^T \tag{3.1.b}$$

and **A** is a matrix obtained by manipulating the material constants $c$, $e$ and $\varepsilon$. The differential equation 3.1.a has the solution:

$$\boldsymbol{\tau}(x_3 + h) = \exp(j\omega \mathbf{A} h)\boldsymbol{\tau}(x_3) = \boldsymbol{\Phi}(h)\boldsymbol{\tau}(x_3) \tag{3.2}$$

The transfer matrix $\boldsymbol{\Phi}$ for each layer of the material system is chain multiplied to get an overall transfer matrix for the entire system. The chain multiplication implicitly ensures that the boundary conditions at all of the interfaces will be satisfied. $\boldsymbol{\Phi}$ is an 8x8 matrix, thus it has eight eigen vectors which correspond to wave solutions. Of these eight eigen vectors, four decay with depth and correspond to SAW solutions. The decay with depth means that the energy of the wave is confined to the surface.

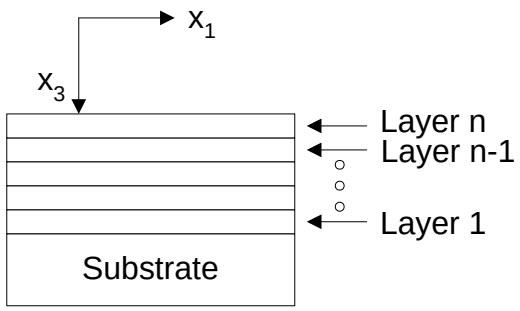


**Figure 3.4.** Reference coordinate axes used in Adler's transfer matrix method [113].

The boundary conditions at the surface and layer interfaces are formulated for either the electrically open (free) or short case (metallized), depending on which SAW velocity is being calculated. Figure 3.5 shows the four possible boundary conditions for the case of a single layer on a substrate, where (a) there is no metallization is present (free-free); (b) there is a conductor on the surface (metallized-free); (c) there is a conductor at the layer-substrate interface (free-metallized); and (d) there are conductors both at the surface and the layer-substrate interface (metallized- metallized). Once the transfer matrices are calculated and the appropriate boundary conditions chosen, a search over a range of acoustic velocities is performed to find the velocities which satisfy the boundary conditions for the material system at a given frequency. The transfer matrix method was implemented using MATLAB scripts.

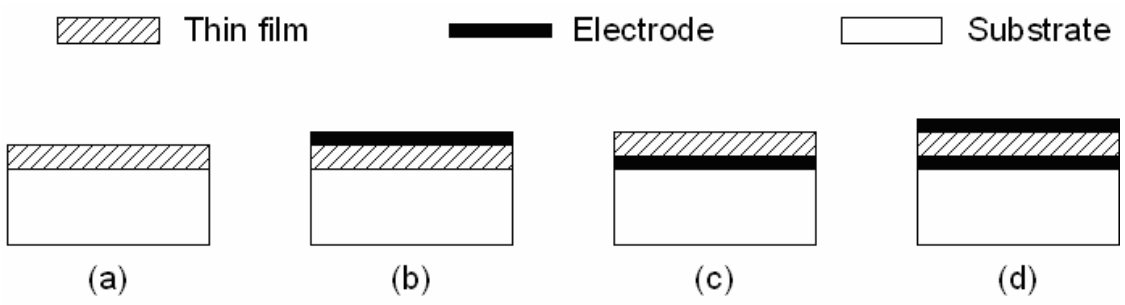


**Figure 3.5.** The four possible boundary conditions: (a) free-free; (b) metallized-free; (c) free- metallized; and (d) metallized- metallized.

The piezoelectric properties of $Al_xGa_{1-x}N$ ($0 \leq x \leq 1$) films on c-$Al_2O_3$ substrates can be tailored by adjusting the Al composition of $Al_xGa_{1-x}N$. The material constants used in the simulation are listed in table 2.1 and 2.3. However, experimentally determined values for $Al_xGa_{1-x}N$ material constants ($\rho$, *c*, *e*, and $\varepsilon$) are not yet available. The material constants of $Al_xGa_{1-x}N$, including density, stiffness, piezoelectric and dielectric constants, are approximated using Vegard's law with AlN and GaN material constants:

$$C_{Al_xGa_{1-x}N} = xC_{AlN} + (1-x)C_{GaN} \tag{3.3}$$

Figure 3.6 shows the calculated acoustic wave velocity and electromechanical coupling coefficient dispersion versus thickness-frequency product *hf*, where *h* is the piezoelectric $Al_xGa_{1-x}N$ film thickness and *f* represents the center frequency. The velocity in the $Al_xGa_{1-x}N$/c-$Al_2O_3$ system increases with increasing Al content, while the coupling coefficient decreases. The maximum electromechanical coupling coefficient is 0.31% for GaN/c-$Al_2O_3$ and 0.15% for AlN/c-$Al_2O_3$, as shown in figure 3.6 (a). The acoustic velocity ranges from 3800 m/s for GaN/c-$Al_2O_3$ to 5750 m/s for AlN/c-$Al_2O_3$, as shown in figure 3.6 (b). The ZnO/c-$Al_2O_3$ structure can propagate higher order wave modes

(HOWMs) of generalized SAW (GSAW) with larger coupling coefficients. The maximum coupling coefficient for the basic wave mode in ZnO/c-$Al_2O_3$ is about 1.16%. In comparison with ZnO/c-$Al_2O_3$, AlN/c-$Al_2O_3$ has higher acoustic velocity with a single base wave mode.

## 3.3 Tailoring of Piezoelectricity in ZnO/$Al_xGa_{1-x}N$/c-$Al_2O_3$ Structures

The SAW properties of the ZnO/$Al_xGa_{1-x}N$/c-$Al_2O_3$ structures can be tailored by controlling Al composition in $Al_xGa_{1-x}N$ and the film thickness ratio of ZnO to $Al_xGa_{1-x}N$.

### *3.3.1 Tailoring by Varying Al composition in $Al_xGa_{1-x}N$ Layer*

Figure 3.7 presents the calculated acoustic velocity curves versus *hf*, for the generalized SAW in the ZnO ($h_1$)/$Al_xGa_{1-x}N$ ($h_2$) (x=0, 0.5, and 1) grown on c-$Al_2O_3$ substrate. In this figure, $h$ is the total thickness of two piezoelectric films, $h = h_1 + h_2$, with $h_1 = h_2$. As shown in figure 3.7(a), the phase velocities of the base and 1st higher order wave mode (HOWM) in ZnO/AlN/c-$Al_2O_3$ structure are higher than those of the ZnO/GaN/c-$Al_2O_3$ structure in the low thickness-frequency range ($hf < 3000$), while at higher *hf* the wave velocity approaches that of ZnO, as most of energy of the wave is transmitted in the ZnO layer. The velocity difference between ZnO/AlN/c-$Al_2O_3$ and ZnO/GaN/c-$Al_2O_3$ becomes more obvious in higher wave modes as shown in figure 3.7(b), because AlN/c-$Al_2O_3$ offers higher velocities than GaN/c-$Al_2O_3$ does (figure 3.6(b)). The velocity dispersion curves of the first two HOWMs come very close but do not cross.

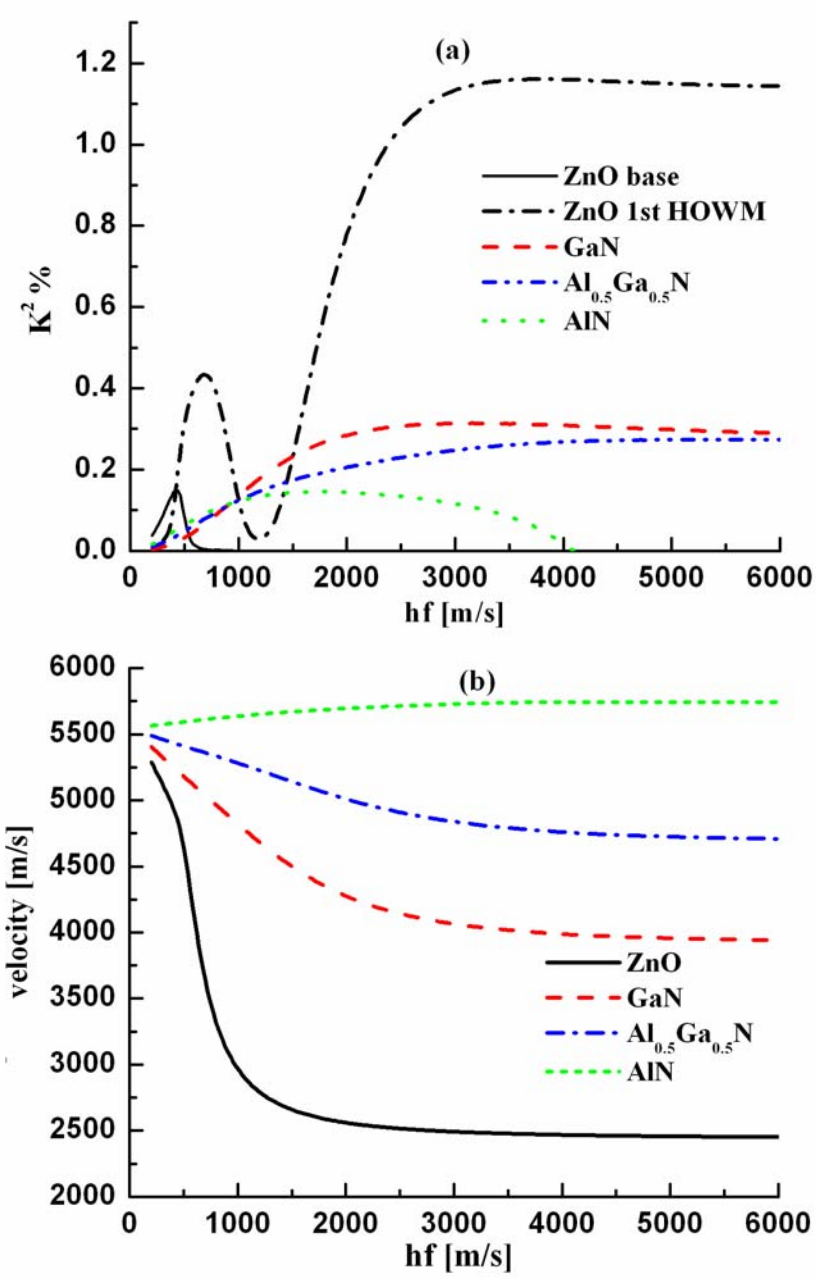


**Figure 3.6.** (a) Piezoelectric coupling coefficient ($K^2$) and (b) SAW velocity ($v$) of the base wave mode in $Al_xGa_{1-x}N$/c-$Al_2O_3$ (x=0, 0.5, and 1) system. For comparison, $K^2$ and velocities of the base and 1st higher order wave modes (HOWM) in ZnO/c-$Al_2O_3$ structures are also plotted.

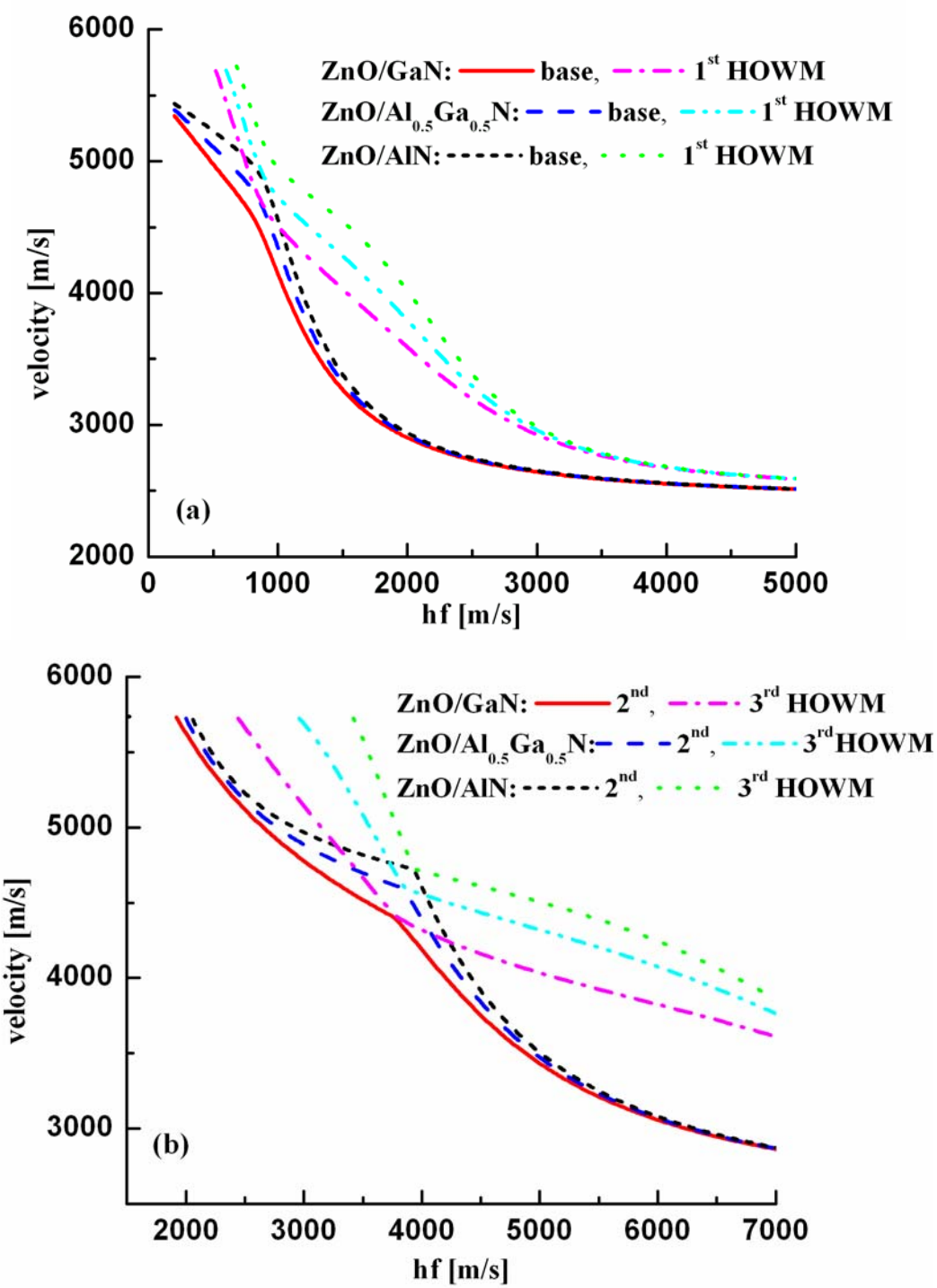


**Figure 3.7.** Velocity dispersion curves for the first four wave modes propagating in the ZnO ($h_1$)/$Al_xGa_{1-x}N$ ($h_2$)/c-$Al_2O_3$ ($h_1 = h_2$, $h = h_1 + h_2$) system, with x=0, 0.5, and 1: (a) the base and 1st HOWM; (b) the 2nd and 3rd HOWM.

As shown in figure 3.8 (a), the electromechanical coupling coefficient ($K^2$) of the basic wave mode increases with decreasing Al mole composition for low *hf* values. As shown in figure 3.8 (b), the $K^2_{max}$ of the second HOWM is estimated to be 4.26% for ZnO/GaN/c-$Al_2O_3$, and 3.79% for ZnO/AlN/c-$Al_2O_3$. The *hf* region where the coupling coefficient is close to $K^2_{max}$ broadens with increasing Al content. The *hf* bandwidth of the second HOWM, in which the coupling coefficient is within ±0.3% of $K^2_{max}$, is calculated to be 820 *hf* for ZnO/GaN/c-$Al_2O_3$, and 1340 *hf* for ZnO/AlN/c-$Al_2O_3$ respectively. The *hf* bandwidth of third HOWM for ZnO/AlN/c-$Al_2O_3$ is about 2280 *hf*. The coupling coefficient of the third HOWM increases and the maximum coupling coefficient region flattens with increasing Al composition. In comparison with a single $Al_xGa_{1-x}N$ layer, a multilayer structure can generate multiple wave modes and broaden *hf* bandwidth of the second and third higher order waves. These properties are very useful to develop high frequency and low loss SAW devices.

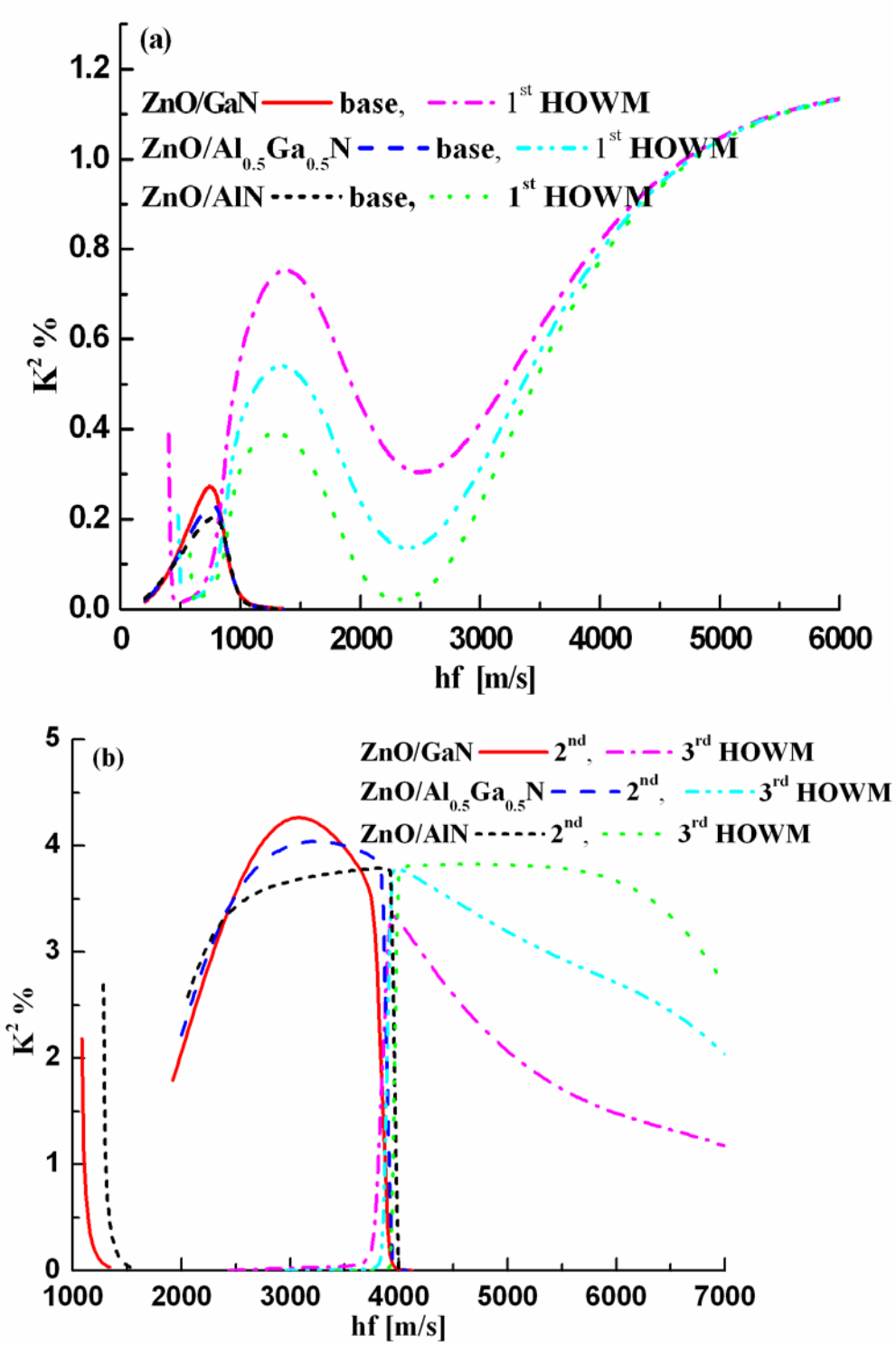


**Figure 3.8.** Piezoelectric coupling coefficients of the first four wave modes propagating in the ZnO ($h_1$)/$Al_xGa_{1-x}N$ ($h_2$)/c-$Al_2O_3$ ($h_1 = h_2$, $h = h_1 + h_2$) system, with x=0, 0.5, and 1: (a) the base and 1st HOWM; (b) the 2nd and 3rd HOWM.

*3.3.2 Tailoring by Varying Thickness Ratio of ZnO to $Al_xGa_{1-x}N$ Layer*

The effect of the ZnO to $Al_xGa_{1-x}N$ film thickness ratio ($h_1/h_2$) on SAW properties was also investigated. It is well known that the ratio of the film thickness $h$ to SAW wavelength $\lambda$ governs the excitation of SAW wave modes in layered structures. For $\lambda >> h$, most of the acoustic energy is transferred in the substrate. As the wavelength gets smaller, a large portion of the acoustic wave propagates in the thin film. For a layered structure in which the top layer has a lower acoustic velocity, an increasing $h/\lambda$ ratio results in a lowering of the acoustic velocity. When $\lambda << h$, the SAW is confined to the thin film layer, and the interface effect due to the reflection of the acoustic wave from the substrate becomes important.

As seen in figure 3.9(a), the calculated coupling coefficient increases with the thickness ratio of AlN to ZnO in low $h_{ZnO}f$ values for the first two wave modes because velocity of AlN/c-$Al_2O_3$ is higher than that of ZnO/c-$Al_2O_3$. In the high $h_{ZnO}f$ region, velocity curves are merged where most SAW energy propagates in the top ZnO film. For the second and third HOWMs shown in figure 3.9 (b), the $h_{ZnO}f$ bandwidth where coupling coefficient is close to the maximum coupling coefficient $K^2_{max}$ broadens with the decreasing thickness ratio of ZnO to $Al_xGa_{1-x}N$. When the thickness ratio of ZnO to AlN ($h_1/h_2$) is 0.5, the widest thickness-frequency product ($h_{ZnO}f$) region is obtained because the coupling curves of the two higher order wave modes come very close and cross when the thickness ratio decreases. By properly selecting the ZnO film thickness, SAW devices with a constant and large coupling coefficient over a wide frequency range can be fabricated and applied to communications and sensor-related systems.

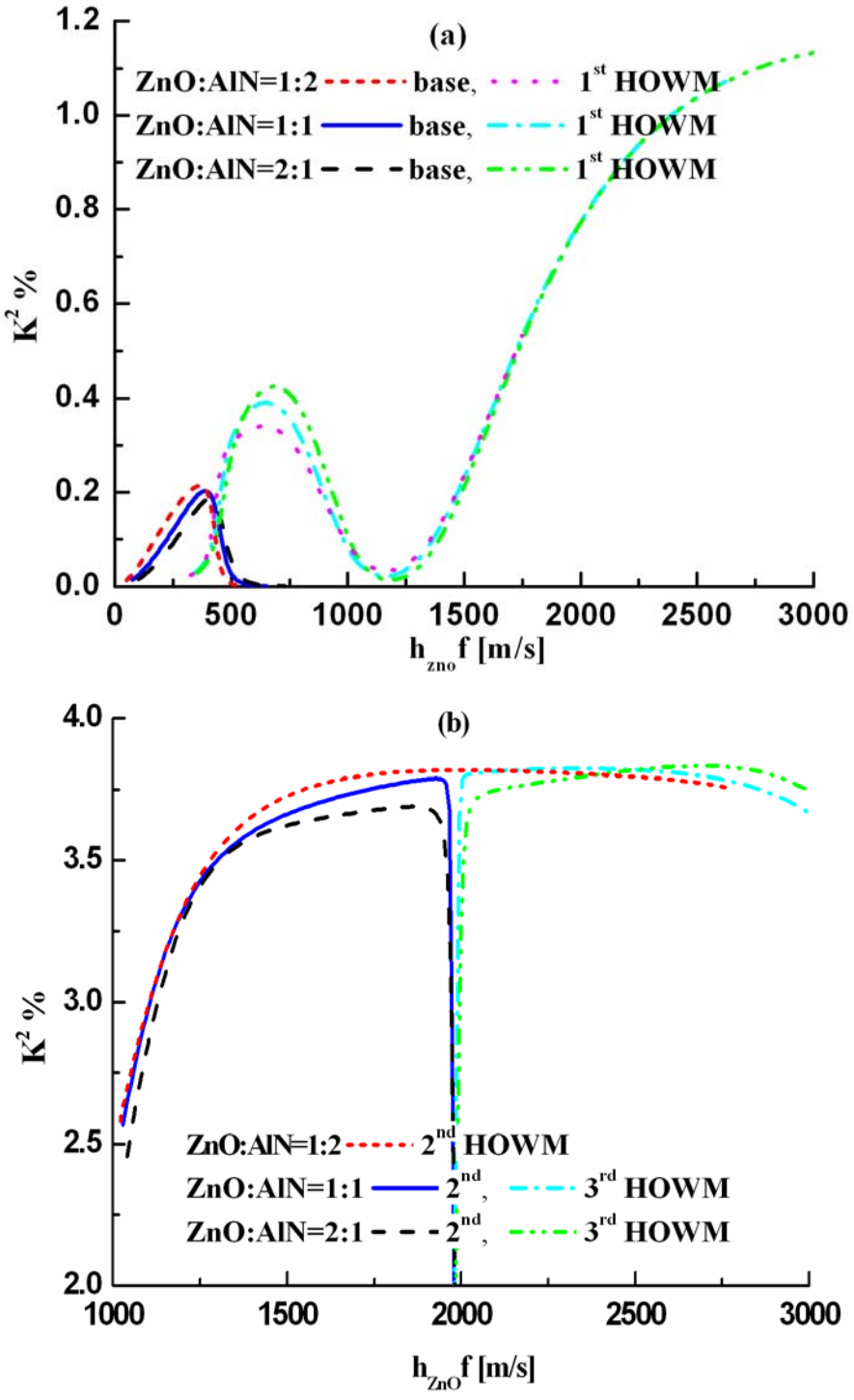


**Figure 3.9.** Piezoelectric coupling coefficients of the first four wave modes propagating in the ZnO ($h_1$)/AlN ($h_2$)/c-$Al_2O_3$ system, with thickness ratio $h_2/h_1$ = 0.5,1 and 2: (a) the base and 1st HOWM; (b) the 2nd and 3rd HOWM.

The effect of the $Al_xGa_{1-x}N$ film compositional variations on the SAW properties was investigated. In commercial foundries, the $Al_xGa_{1-x}N$ film composition variance is less than 2%. As an example, for $Al_{0.5}Ga_{0.5}N$ with a compositional error of ±1%, acoustic velocity of the base wave mode varies less than ±0.19% and its coupling coefficient has a variation less than ±0.66%. For the first higher order wave mode, the velocity variance is less than ±0.26% and the coupling coefficient's variance is less than ±4.3 %. For the 2nd HOWM, the variances in the velocity and coupling coefficient are less than ±0.10% and ±0.12 %, respectively, in the *hf* region of interest where the coupling is close to its maximum value. Therefore, the impact of the $Al_xGa_{1-x}N$ compositional variations will have a negligible effect on the device performance.

## 3.4 Fabrication of Testing Devices

Figure 3.10 shows the photo image of a basic SAW test structure, consisting of a delay line design using quarter-wavelength and split electrode inter-digital transducers (IDTs). Devices with different wavelengths were placed on the same mask set to facilitate the analysis of various film thickness-frequency products. The basic SAW test structure set consists of two delay lines with 1mm and 2mm delay length. The inter-digital transducers have wavelengths of 6, 8, and 10 μm for the λ/4 electrode IDTs, and 12, 16, and 20 μm for the split (λ/8) electrode IDTs, with 40 electrode pairs. The device fabrication process consists of e-beam evaporation of Al film (1500Å), followed by photolithography and Al etching to form the IDTs.

The SAW devices were characterized using an HP 8573D network analyzer (Agilent Technologies, Palo Alto, CA) and a Cascade Microtech probe station (Cascade

Microtech Inc. Beaverton, OR). All measurements were made on-wafer under untuned conditions. The schematic of SAW device testing setup is shown in figure 3.11.

The experimental acoustic velocities $v_{\exp}$ were estimated by the relation: $v_{\exp} = \lambda_0 f_c$ , where $f_c$ is the center frequency of the tested devices' transmission parameter $S_{21}$, and $\lambda_0$ is the SAW wavelength determined by the IDT period. The accuracy in the measurement of $f_c$ was limited by the degradation in the sinc shape of the IDT frequency response, due to second-order effects, such as electrical feed through, triple transit, and internal reflections within IDT electrodes, etc. By using split-electrode transducers to reduce inter-electrode reflections, and by judiciously choosing the gating time slot, their effects on the final analysis can be considerably reduced. The transfer parameter $S_{21}$ of the test devices was measured. The dispersive velocities were compared with the simulation results.

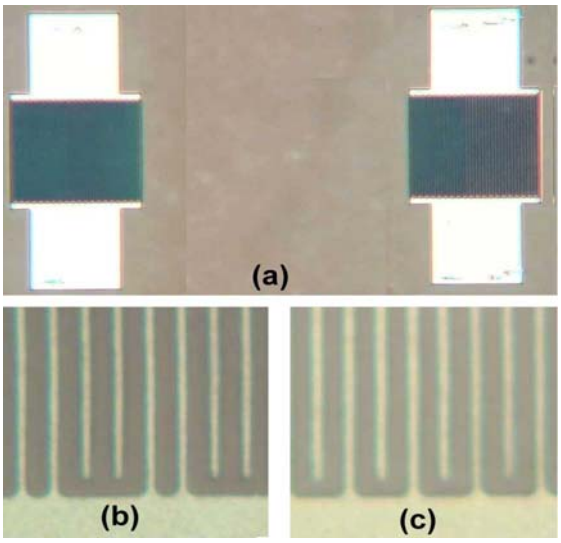


**Figure 3.10.** SAW testing device: (a) SAW delay line filter; (b) split electrode IDT structure; and (c) quarter-wavelength IDT structure.

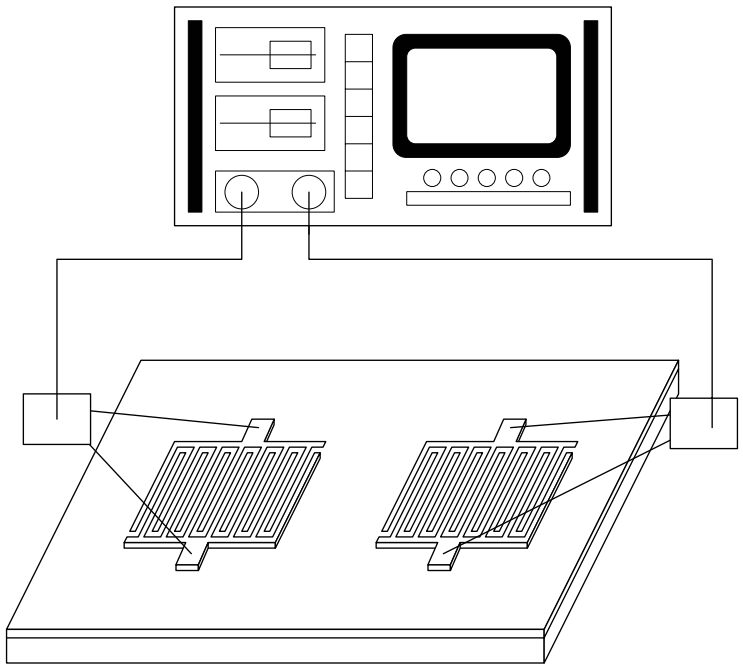

**Figure 3.11**. The schematic of SAW testing setup.

## 3.5 Measurement Results and Discussion

Piezoelectric ZnO thin films with various thicknesses were deposited on $Al_xGa_{1-x}N/c\text{-}Al_2O_3$ using the RF sputtering technique. SAW test devices were fabricated on ZnO films on $Al_xGa_{1-x}N/c\text{-}Al_2O_3$. In these devices, AlN film thickness was 0.35~0.5 μm, GaN film thickness was about 2.9 μm, and ZnO film was 0.28~1.35 μm.

In figure 3.12 (a), the solid line represents calculated velocities in GaN(2.9μm)/c-$Al_2O_3$ and the "Δ" is the measured velocities. The dash line represents velocity dispersion in ZnO(0.28 μm)/GaN(2.9μm)/c-$Al_2O_3$ while the testing results are marked with "*". The measured data fit the theoretical predictions closely for the GaN and ZnO/GaN samples. In figure 3.12(b), velocity dispersion curve in AlN/c-$Al_2O_3$ is the solid line and velocity dispersion curve in ZnO(0.28 μm)/AlN(0.4 μm)/c-$Al_2O_3$ is the dash line. The measured

data of AlN/c-$Al_2O_3$ and ZnO/AlN/c-$Al_2O_3$ are marked with “x” and “o”, respectively. In the case of AlN and ZnO/AlN, the measured velocities are higher than the predicted values, primarily due to the thickness fluctuation and inaccuracies in the AlN material constants used for the simulation.

Figure 3.13 presents the acoustic velocity dispersion versus thickness-frequency product *hf*. The thickness ratio of ZnO to $Al_xGa_{1-x}N$ was maintained approximately at 1.2 while Al mole composition in $Al_xGa_{1-x}N$ film was changed. “o” marks the velocities of the base wave mode and “□” represents the first higher order wave mode in the ZnO(0.66μm)/AlN(0.54μm) structure. “∇” and “Δ” represent the velocities of the base and first higher order wave mode of the ZnO(0.64μm)/$Al_{0.65}Ga_{0.35}N$(0.51μm) structure, respectively. The simulated velocities of the ZnO/AlN/c-$Al_2O_3$ structure are larger than those of the ZnO/GaN/c-$Al_2O_3$ which can be verified by experimental measurements.

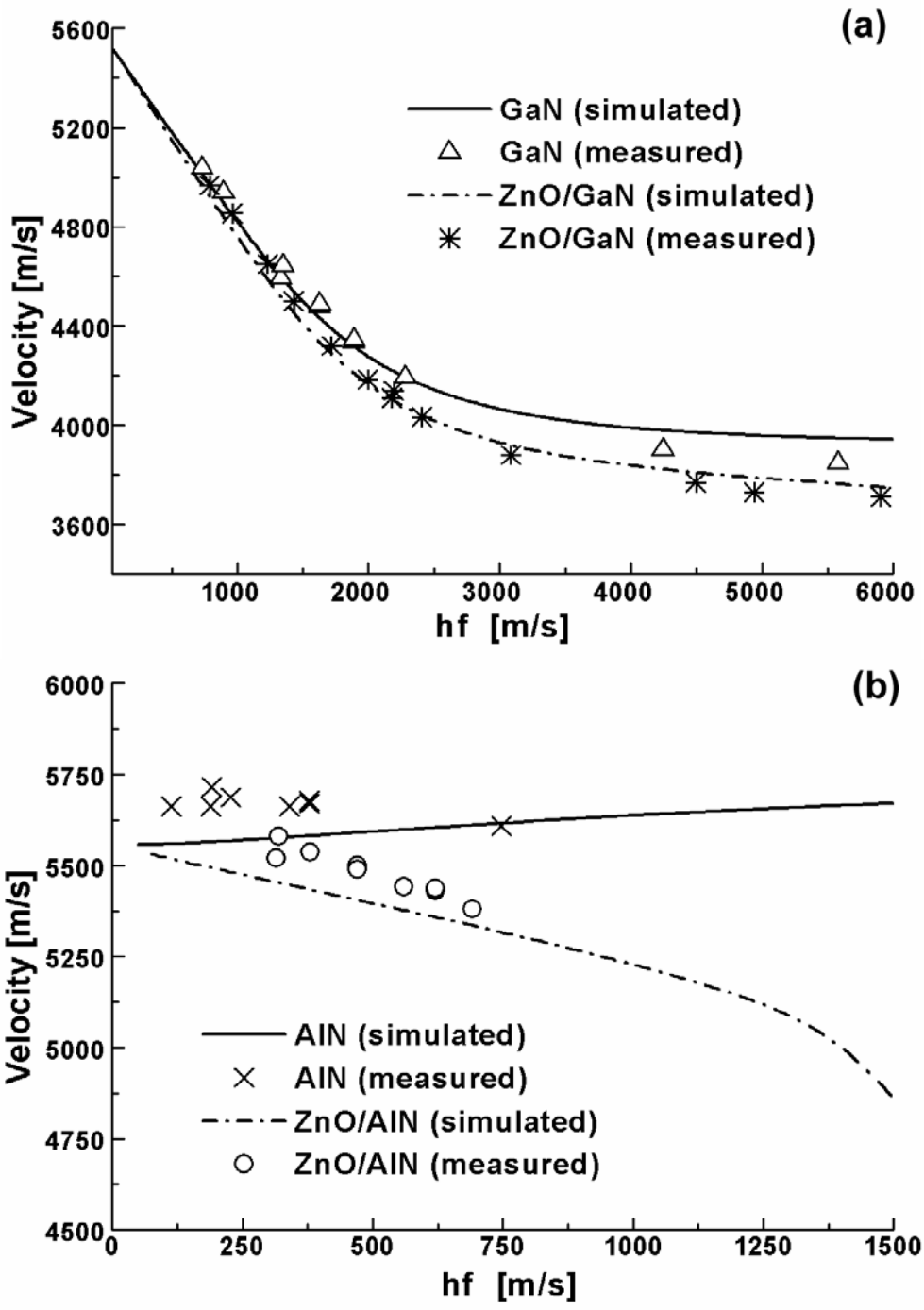


**Figure 3.12.** Comparison of simulated and measured acoustic velocities of the base wave mode for (a) GaN/c-$Al_2O_3$ and ZnO/GaN/c-$Al_2O_3$, (b) AlN/c-$Al_2O_3$ and ZnO/AlN/c-$Al_2O_3$.

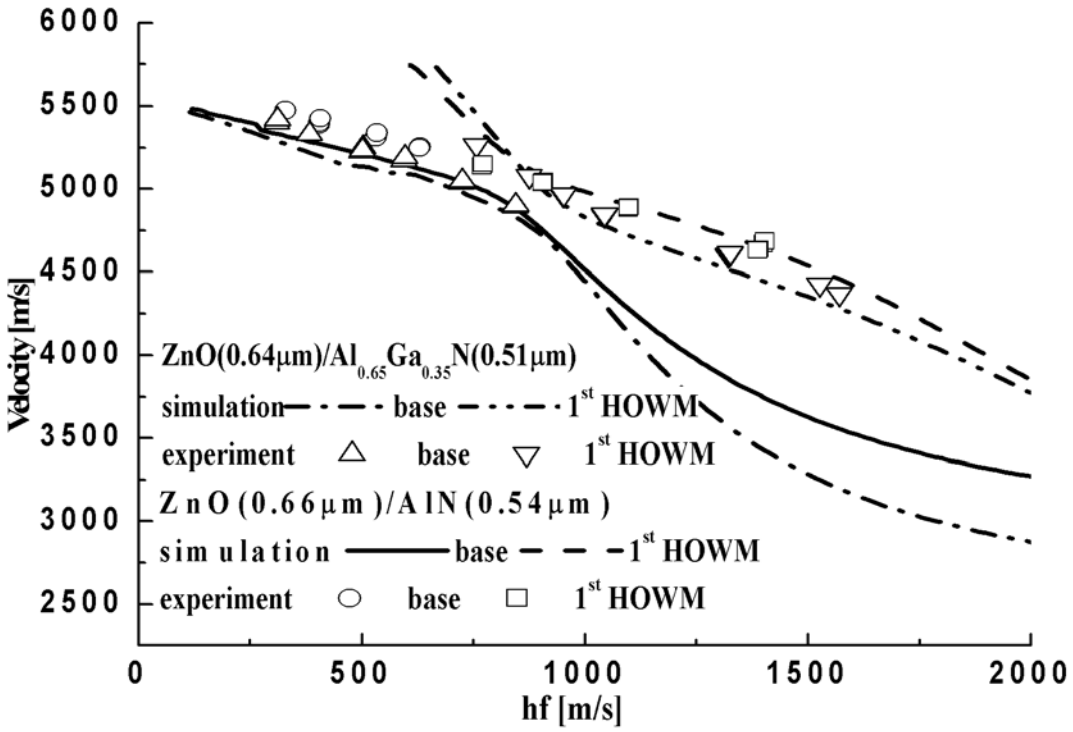


**Figure 3.13.** Comparison of simulated and measured acoustic velocities of the base and 1st HOWM for ZnO($h_1$)/$Al_xGa_{1-x}N$ ($h_2$)/c-$Al_2O_3$, with x=0.65, 1, and fixed film thickness ratio ($h_1/h_2$=1.2).

In figure 3.14, the thickness ratio of ZnO to $Al_xGa_{1-x}N$ was kept at 0.55. "∇" marks the velocities of the first two wave modes in the ZnO(0.37μm)/AlN(0.54μm)/c-$Al_2O_3$ system, while "o" the represents velocities in the ZnO(0.37μm)/$Al_{0.60}Ga_{0.40}N$(0.67μm)/c-$Al_2O_3$ system, and "Δ" is the velocities of the ZnO(1.35μm)/GaN(2.9μm)/c-$Al_2O_3$ system. The phase velocities of the basic and 1st higher order wave modes increase as the Al content in $Al_xGa_{1-x}N$ increases. The measured velocities are in agreement with the simulated results.

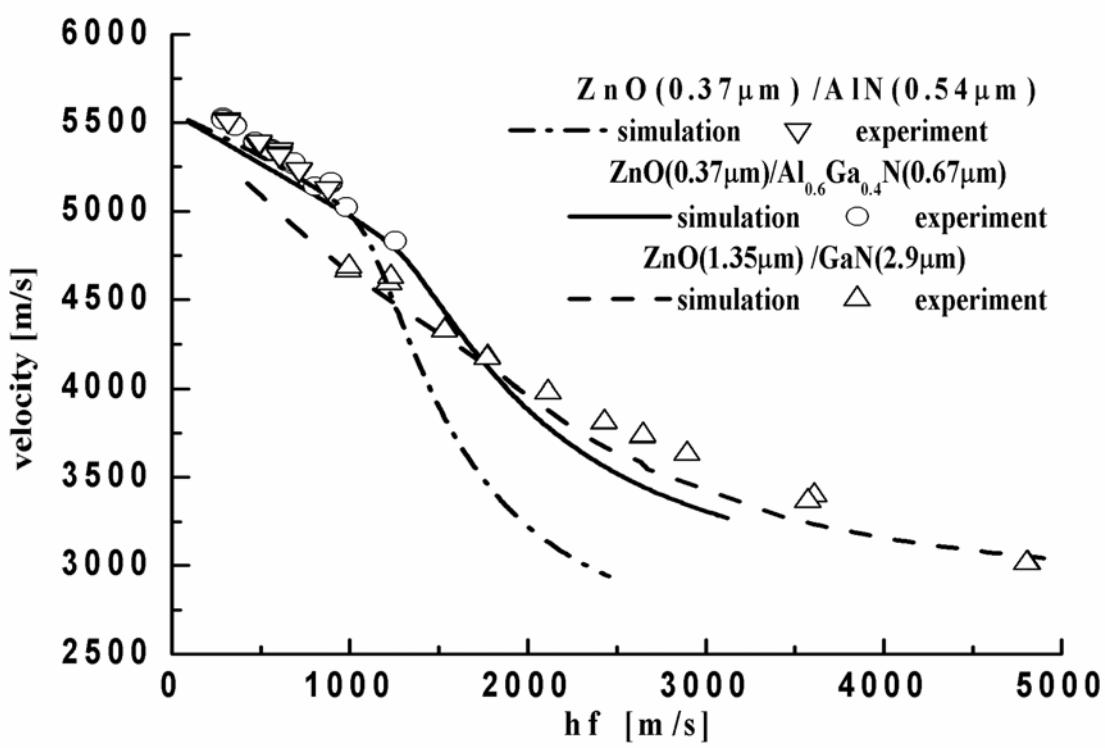


**Figure 3.14.** Comparison of simulated and measured acoustic velocities of the base wave mode for ZnO($h_1$)/$Al_xGa_{1-x}N$ ($h_2$)/c-$Al_2O_3$, with x=0, 0.65, and 1.

The effect of ZnO film thickness in ZnO/$Al_xGa_{1-x}N$/c-$Al_2O_3$ was tested by fixing the Al composition, x. In figure 3.15**,** "o" marks velocities varied with the ZnO thickness-frequency product ($h_{ZnO}f$) when the thickness ratio of ZnO to GaN is 0.15. "☆" represents velocities as the thickness ratio is 0.26. "∇" and "Δ" represent velocities while the thickness ratio is 0.46. The measured results are well matched with the simulation curves for the ZnO/GaN/c-$Al_2O_3$. The acoustic velocities for the first two wave modes increase with the ZnO films thickness.

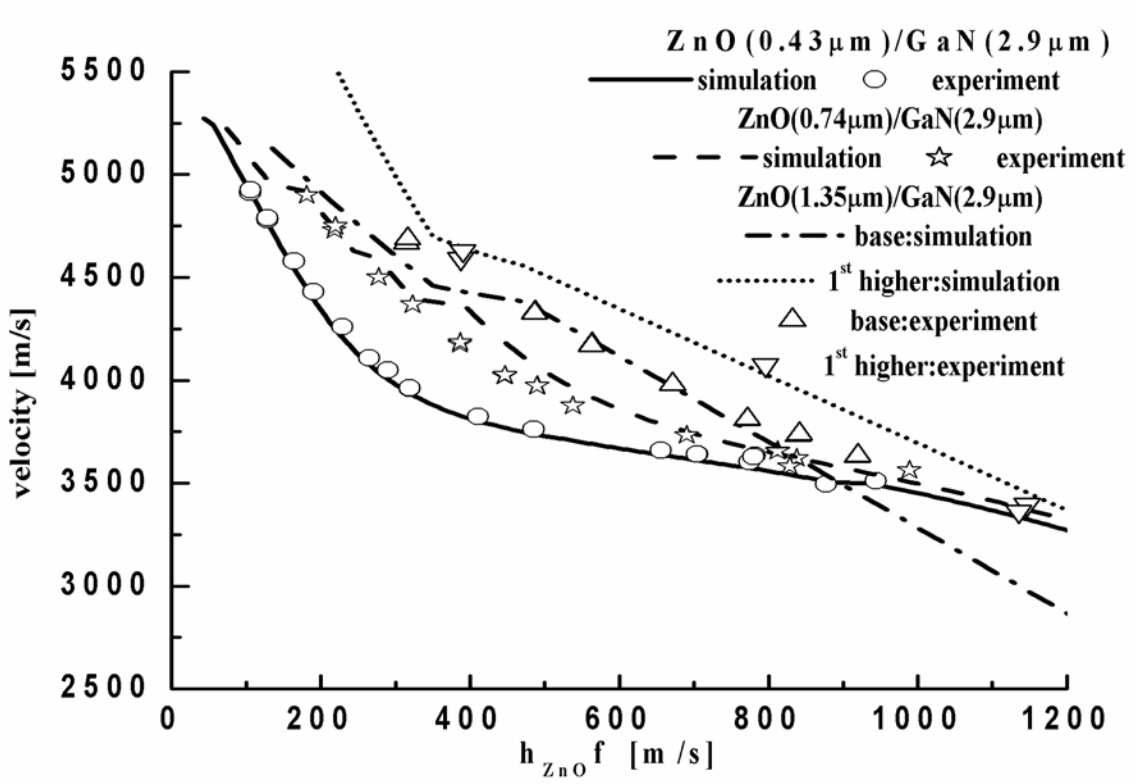


**Figure 3.15.** Comparison of simulated and measured acoustic velocities for the first two wave modes propagating in the ZnO ($h_1$)/GaN ($h_2$)/c-$Al_2O_3$ system, with thickness ratio $h_2/h_1$ =0.15, 0.26 and 0.46.

## 3.6 Summary

Piezoelectric ZnO thin films were deposited on $Al_xGa_{1-x}N$/c-$Al_2O_3$ using RF sputtering technique. The film quality was verified using X-ray diffraction and FESEM. The ZnO films were well oriented along the c-axis and uniform. The layered structure ZnO/$Al_xGa_{1-x}N$/c-$Al_2O_3$ ($0 \le x \le 1$) provides the flexibility to tailor acoustic properties by controlling the Al composition, *x*, in $Al_xGa_{1-x}N$, and the thickness ratio of ZnO to $Al_xGa_{1-x}N$. The simulation results showed the dispersive properties of phase velocity and piezoelectric coupling coefficient versus the thickness-frequency product (*hf*). The

acoustic wave velocity increased and piezoelectric coupling decreased with increasing Al composition in the ZnO/$Al_xGa_{1-x}N$/c-$Al_2O_3$. The *hf* region where the coupling coefficient of the 2nd and 3rd higher order wave modes were close to the maximum value ($K^2_{max}$) broadened with increasing Al content, while $K^2_{max}$ decreased slightly. In addition, the calculated coupling coefficient increased with the film thickness ratio of $Al_xGa_{1-x}N$ to ZnO in low *hf* values for the first two basic wave modes. The $h_{ZnO}f$ bandwidths of the second and third higher order wave modes broadened with the increasing thickness ratio of $Al_xGa_{1-x}N$ to ZnO. Theoretically calculated and experimentally obtained velocities in ZnO/ $Al_xGa_{1-x}N$/c-$Al_2O_3$ were found to be in good agreement. This multilayer structure is promising for the development of high velocity, low loss and wide bandwidth SAW devices, which can be used in both the communications and sensors fields.

# CHAPTER IV. SAW CHARACTERISTICS IN $Mg_xZn_{1-x}O$/r-$Al_2O_3$

In this chapter, the novel hybrid deposition technology was presented to achieve the piezoelectric a-plane $Mg_xZn_{1-x}O$ ($0 \le x \le 0.3$) films on r-plane $Al_2O_3$. In the hybrid deposition process, a thin ZnO buffer layer with a minimum thickness of ~10nm was grown by MOCVD, followed by sputtering deposition of a thick piezoelectric Ni-doped $Mg_xZn_{1-x}O$ films. High frequency and low-loss SAW test devices were fabricated on the piezoelectric a-plane $Mg_xZn_{1-x}O$ films. The effects of the thin ZnO buffer layer and the post-deposition annealing condition on SAW properties were studied. Piezoelectric properties were found to be enhanced by post-deposition annealing process which improves the crystallinity of the films. Anisotropic piezoelectric properties in these multilayer structures were also investigated. The velocities of the Rayleigh wave in $Mg_xZn_{1-x}O$ films with different Mg composition were simulated and compared with the measured data.

## 4.1. Hybrid Deposition of Piezoelectric ZnO and $Mg_xZn_{1-x}O$ Films on r-$Al_2O_3$

Piezoelectric ZnO is promising for fabrication of high frequency and low-loss surface acoustic wave devices, bulk acoustic wave resonators, and microelectronic mechanical systems. By alloying ZnO with MgO, a ternary $Mg_xZn_{1-x}O$ is formed. $Mg_xZn_{1-x}O$ is piezoelectric in the range of Mg composition where it retains the wurtzite crystal structure, $0 \le x \le 0.33$. The acoustic velocity in piezoelectric $Mg_xZn_{1-x}O$ ($0 \le x \le$

0.3) increases with the Mg composition, while the electromechanical coupling coefficient ($K^2$) decreases. This property provides the flexibility to tailor SAW properties by changing the Mg composition, in addition to adjustment of the film-thickness to wavelength ratio $h/\lambda$, where $h$ stands for the film thickness and $\lambda$ represents the SAW wavelength.

Sapphire is non-piezoelectric material, but has high acoustic velocity and low acoustic attenuation loss. An r-plane $(01\bar{1}2)$ sapphire (r-$Al_2O_3$) is used for this study instead of the commonly used c-sapphire due to the overall lower lattice mismatch between $Mg_xZn_{1-x}O$ and r-$Al_2O_3$ [95]. In addition, $Mg_xZn_{1-x}O$ films grown on r-$Al_2O_3$ substrates possess the in-plane anisotropic properties, which can be used for multi-mode SAW generation. Furthermore, $Mg_xZn_{1-x}O$/r-$Al_2O_3$ system has higher electromechanical coupling coefficients, $K^2$, up to 6% for certain wave modes.

ZnO films have been deposited on sapphire substrates by MOCVD, pulsed laser deposition, and sputter deposition. MOCVD is widely used for epitaxial growth of semiconductor thin films. It has proved successful for high quality semiconductor device manufacturing, especially for III-V compounds, and oxides. The MOCVD grown $Mg_xZn_{1-x}O$ ($0 \le x \le 0.33$) films on r-plane sapphire substrates have c-axis in-plane of the substrate [95]. There is a reduced lattice mismatch (1.53%) along the c-axis, i.e. the [0001] direction, in comparison with a large mismatch (18.3%) perpendicular to the c-axis, i.e. the $(1\bar{1}00)$ direction. However, MOCVD grown ZnO and $Mg_xZn_{1-x}O$ generally show n-type conductivity due to various native defects. It is difficult to realize the piezoelectricity in $Mg_xZn_{1-x}O$ films using MOCVD technique due to limited availability of MO-precursors for in-situ compensation doping. Furthermore, solid solubility of

dopants is often limited in near equilibrium MOCVD growth. The post-deposition compensation doping is required to achieve piezoelectricity [73]. Also MOCVD grown $Mg_xZn_{1-x}O$ films show cracks when the film thickness above 1 μm. In contrast, sputtering is a popular technique for depositing thick piezoelectric ZnO layers with high compensation doping density on various substrates for SAW and BAW applications; however, the crystallinity of such films is generally poor in comparison to the MOCVD deposited films. Thus, a combination of MOCVD grown thin ZnO buffer and sputtering deposited thick Ni-doped piezoelectric $Mg_xZn_{1-x}O$ can be used to achieve a piezoelectric film with high structural quality and good SAW characteristics.

Key issues for $Mg_xZn_{1-x}O$ SAW device fabrication include the control of the film quality and thickness uniformity. MOCVD grown ZnO buffer ensures deposition of wurzite $Mg_xZn_{1-x}O$ on r-sapphire substrate. Furthermore, ZnO buffer prevents Mg diffusion to the r-sapphire substrate. Highly crystalline ZnO buffer layers were grown on the r-sapphire substrates in a vertical-flow, rotating disc MOCVD reactor [114]. Diethylzinc (DEZn) and oxygen were used as the Zn metal-organic source and oxidizer, respectively, and argon was used as the carrier gas. Typical growth temperatures of the ZnO buffer ranged from 400°C - 500°C. The growth rate was reduced to 60-100 nm/hr for better thickness control and higher crystallinity of the ZnO buffer. The buffer film thickness was found to be ~15nm, as measured by x-ray reflectivity. Subsequently, $Mg_xZn_{1-x}O$ films with thicknesses in the range of 1.0 to 2.4μm were deposited using RF sputtering. The high coupling coefficient can be achieved by using thick piezoelectric $Mg_xZn_{1-x}O$ films with good epitaxial quality. The sputtering targets for piezoelectric film deposition were prepared by mixing appropriate composition ratio of ZnO and MgO

powders to form $Mg_xZn_{1-x}O$, while NiO (2 wt%) powder was added for compensation doping. During the RF sputter deposition, the substrates were heated to 420 ~ 450°C. The deposition was carried out in a controlled ambient mixture of Ar and $O_2$ in 1:1 ratio with typical deposition rate ranging from 400 - 700 nm/hr. The as-deposited $Mg_xZn_{1-x}O$ films were annealed in an $O_2$ atmosphere for 2.5 hours at temperatures ranging from 600 ~ 700°C, to improve film quality.

## 4.2 Material Characterizations

The surface morphology of the $Mg_xZn_{1-x}O$ ($0 \leq x \leq 0.3$) films was analyzed using a Leo-Zeiss field emission electron microscope (FESEM). High-resolution x-ray diffraction (XRD) analysis was carried out using a Bruker D8-Discover four-circle x-ray diffractometer with four bounce Ge (220)-monochromated Cu $K\alpha_1$. X-ray reflectivity measurements were done to measure the buffer thickness. A highly collimated and monochromated x-ray beam was shone on the sample surface at low grazing incident angles over an angular range between 0 to 4 degrees. The accuracy of film thickness determination was typically a few angstroms. In-plane orientation of the hybrid deposited films was analyzed by φ-scans. Rutherford back scattering (RBS) was performed using a probe beam of 1.99 MeV $He^+$ ions and a standard surface detector positioned at 165° for compositional analysis of the deposited films.

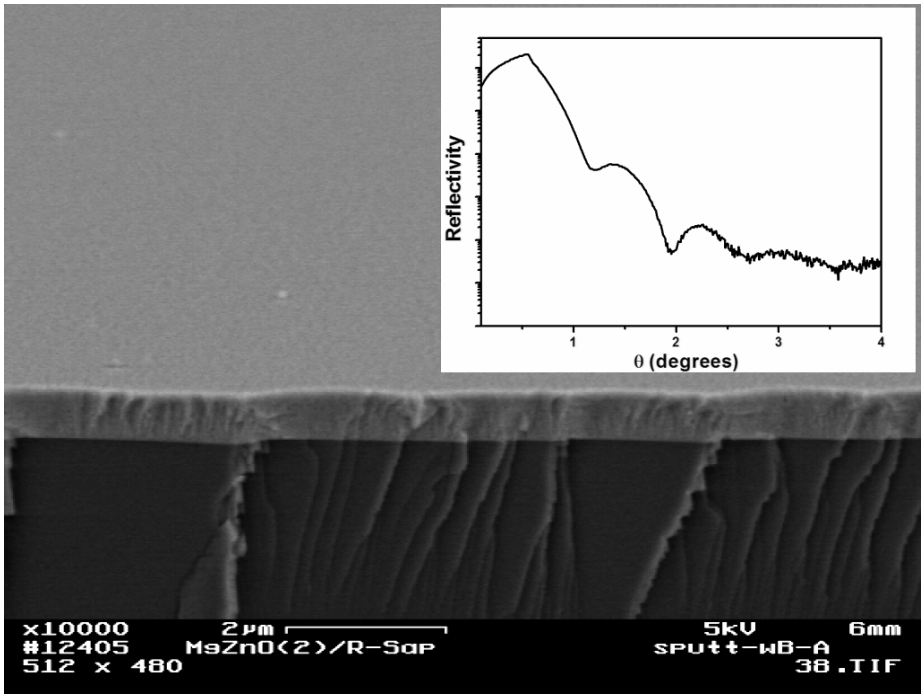


**Figure 4.1.** FESEM image of hybrid deposited $Mg_{0.2}Zn_{0.8}O$ films on r-$Al_2O_3$ substrates, followed by post-annealing at 700°C for 2 hours. Inset, shows a grazing incidence X-ray reflectivity measurement, angular range 0 – 4°, of MOCVD deposited ZnO buffer.

Shown in figure 4.1, is the FESEM image of a piezoelectric $Mg_{0.2}Zn_{0.8}O$ film deposited by the hybrid deposition technology, followed by annealing in $O_2$ atmosphere at 700°C for 2 hours. The annealing temperature for this study was chosen to be below 750 °C to prevent possible formation of a $ZnAl_2O_4$ spinel at the $(11\bar{2}0)$ ZnO/ r-$Al_2O_3$ interface [115]. It is observed that the film is dense and uniform with smooth surface morphology. Inset of figure 4.1 shows X-ray reflectivity measurement of the MOCVD grown ZnO buffer on r-sapphire substrate. The thickness of the ZnO buffer was calculated to be ~9 nm.

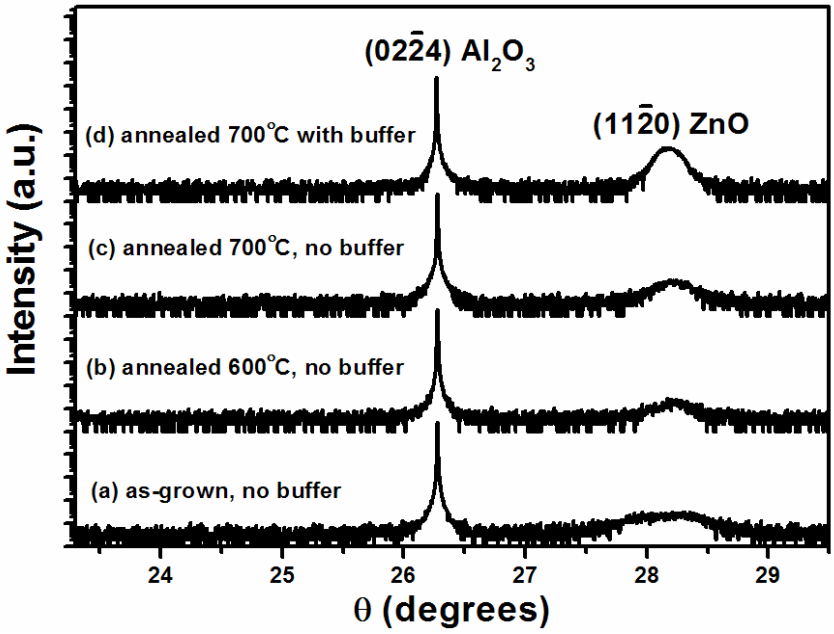


**Figure 4.2.** X-ray diffraction of 1.7μm thick ZnO films on r-sapphire substrates, a) as-deposited without a buffer, b) post-annealed at 600°C without a buffer, c) post-annealed at 700°C without a buffer, and d) with a buffer (hybrid deposition) post-annealed at 700°C.

Figure 4.2 (a) to (c), shows the XRD of the piezoelectric ZnO films directly sputtered on r-sapphire substrates without MOCVD grown ZnO buffer, (a) as-deposited, (b) annealed at 600°C and (c) annealed at 700°C. It is observed that the as-deposited sputtered films have the expected a-axis $(11\bar{2}0)$ orientation, however, the crystallinity is poor as indicated by the large FWHM of the $(11\bar{2}0)$ ZnO reflection. Post-annealing improves the crystallinity, with the highest temperatures giving the best results. Figure 4.2 (d), shows XRD scan of hybrid deposited piezoelectric ZnO film on r-sapphire substrate, post-annealed at 700°C for 2 hours. It is observed that the MOCVD grown

ZnO buffer greatly improves the FWHM and the intensity of the $(11\bar{2}0)$ ZnO diffraction peak of the following sputtering deposited films.

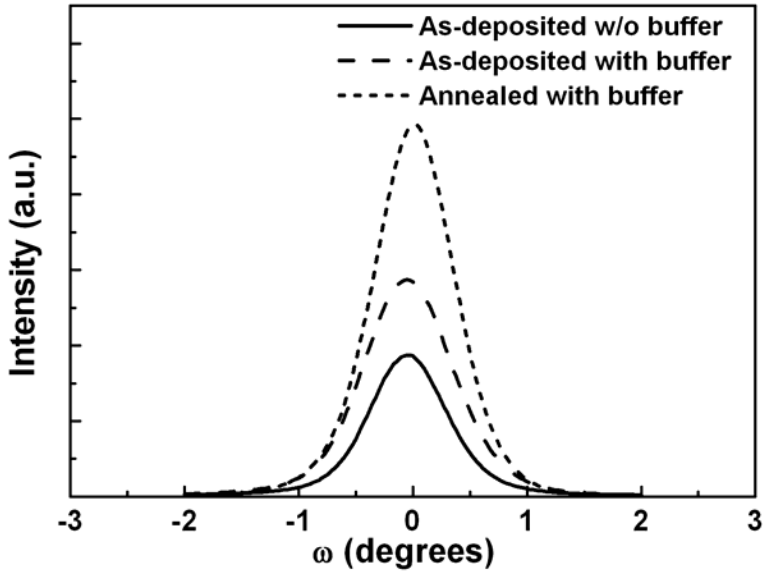


**Figure 4.3.** Omega rocking curves comparison for as-deposited ZnO film without a MOCVD buffer, as-deposited ZnO film with a MOCVD buffer, and ZnO film with a MOCVD buffer and being post-deposition annealed.

Figure 4.3 shows a comparison of omega rocking curves of as-deposited ZnO film without a MOCVD layer, as-deposited ZnO film with a MOCVD buffer layer, and ZnO film with a MOCVD buffer layer and being post-deposition annealed. A reduction in the full-width at half maximum (FWHM) of the omega rocking curves indicates that the hybrid deposited film followed by post annealing treatment has lower mosaic spread compared to both as-deposited and non-annealed films.

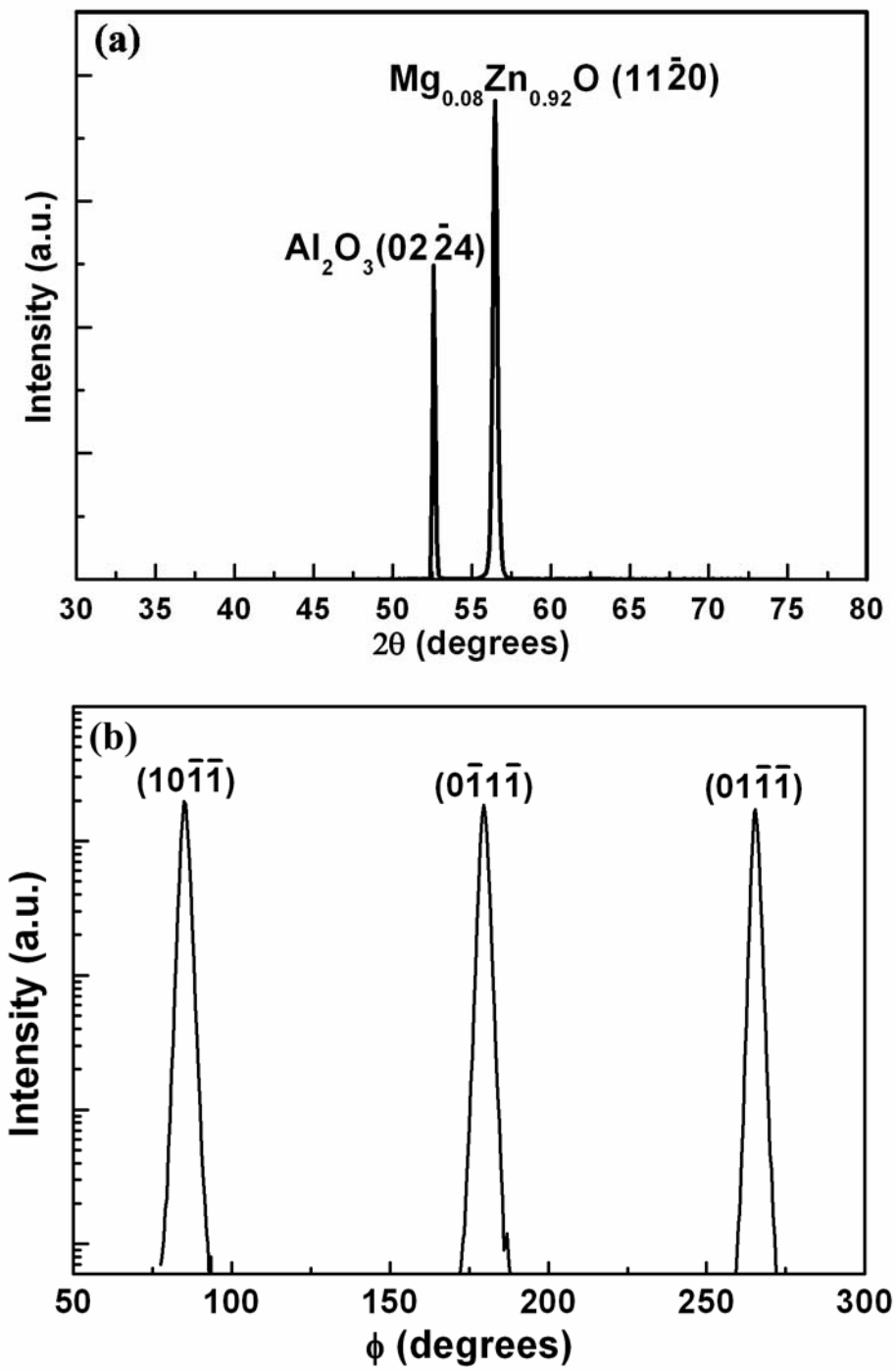


**Figure 4.4.** X-ray diffraction: (a) θ-2θ scan and (b) Phi scan of $\{10\bar{1}1\}$ family of planes of hybrid deposited and annealed $Mg_{0.08}Zn_{0.92}O$ film with thickness 2.15μm.

Figure 4.4 shows XRD of the $Mg_{0.08}Zn_{0.92}O$ film: (a) θ-2θ scan and (b) Phi scan around {10-11} family of planes. The φ-scan confirms the in-plane registry of the deposited film with the r-sapphire substrate. The epitaxial relationship between the a-$Mg_{0.08}Zn_{0.92}O$ film and the r-sapphire substrate is retained as $(11\bar{2}0)$ MgZnO || $(01\bar{1}2)$ $Al_2O_3$ and $[0001]$ MgZnO || $[0\bar{1}11]$ $Al_2O_3$, identical to the epitaxial relationship reported for MOCVD grown $Mg_xZn_{1-x}O$ films on r-plane $Al_2O_3$ substrates [95].

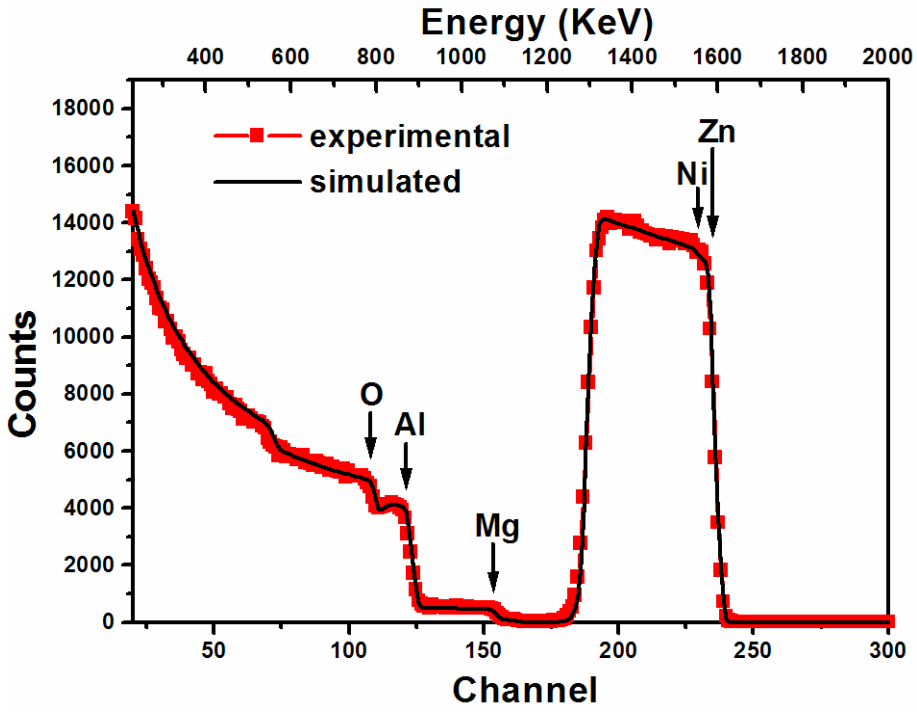


**Figure 4.5.** Rutherford Back Scattered (RBS) spectra for Ni-doped (~2.5%) $Mg_{0.16}Zn_{0.84}O$ film deposited on r-sapphire substrate.

Figure 4.5 shows the RBS spectra of a piezoelectric $Mg_{0.16}Zn_{0.84}O$ film deposited on r-$Al_2O_3$ substrate. The Mg and Ni compositions were determined from fitting the simulated profile to the experimental data. Mg and Ni composition in the deposited film

was found to be similar to the molar ratio of MgO, NiO and ZnO powders in the sputtering target.

The hybrid deposition technique enables the growth of high quality thick piezoelectric ZnO films (>2.0 μm) on r- $Al_2O_3$ without cracks, while keeping the in-plane piezoelectric anisotropy for multi-mode acoustic wave generation. A voltage controlled tunable surface acoustic wave phase shifter was made of a ZnO based semiconducting/piezoelectric dual-layer structure on an r-$Al_2O_3$ substrate by using the MOCVD-sputtering hybrid deposition technology [116]. Figure 4.6 (a), shows the FESEM images of the dense and uniform piezoelectric ZnO template, the inset shows x-ray phi scan of the film on r- $Al_2O_3$ substrate. Then, a 100 nm thick semiconducting ZnO layer was deposited on top of the piezoelectric layer using MOCVD at 450 – 550 °C, with a growth rate of ~0.5 μm/ hr. Figure 4.6 (b) shows the FESEM image of the smooth and dense re-grown ZnO layer. The inset represents a coupled x-ray θ-scan of the ZnO dual-layer structure. It clearly shows that both of the semiconducting and piezoelectric ZnO layers are along the $(11\bar{2}0)$ a-plane. Piezoelectric and semiconducting ZnO layers are used for SAW excitation and n-type conducting channel and $SiO_2$ serves as the gate insulator. The acoustic velocity of the device can be tuned by changing the n-channel conductance with a DC bias.

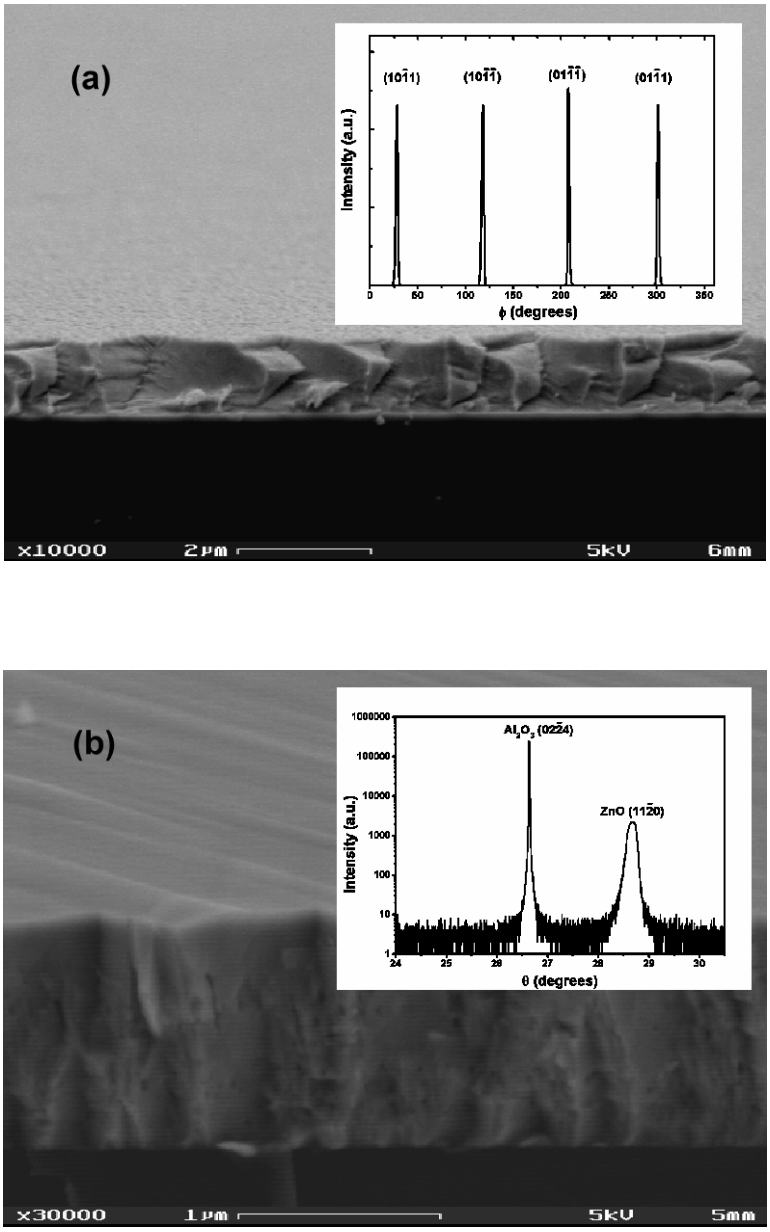


**Figure 4.6.** (a) FESEM image of the hybrid MOCVD-sputtering deposited piezoelectric ZnO layer on r-$Al_2O_3$ substrate. The inset shows X-ray φ-scan of the film; (b) semiconducting/piezoelectric ZnO dual-layer structure. The inset shows coupled X-ray θ-scan of the semiconducting ZnO film re-grown on the piezoelectric template.

## 4.3 Piezoelectric Characterizations

The epitaxial relationship between wurzite a-plane $Mg_xZn_{1-x}O$ and r-plane sapphire causes in-plane structural, optical, and acoustic anisotropy, making it useful for the devices based on acousto-optical and acousto-electrical interactions. In the a-$Mg_xZn_{1-x}O$/r-$Al_2O_3$ structure, c-axis lies in the growth plane; therefore, the Rayleigh-type and the Love-type surface acoustic waves can be excited. The Rayleigh-type wave modes have the maximum electromechanical coupling for propagation parallel to the c-axis of the film, whereas the Love-type wave modes have the maximum electromechanical coupling for propagation perpendicular to the c-axis of the film. The Rayleigh-type wave mode along the [0001] direction has a higher phase velocity than the Love-type wave mode in the $[1\bar{1}00]$ direction. Particularly, the Sezawa wave is more attractive for SAW device applications because of its high velocity and large electromechanical coupling coefficient. In particular, the in-plane anisotropic property of a-$Mg_xZn_{1-x}O$ films grown on r-sapphire has unique applications for SAW sensors: the Rayleigh wave mode (shear-vertical) for gas-phase sensing and the Love wave mode (shear-horizontal) for liquid-phase sensing.

Figure 4.7 shows schematic and optical images of the SAW test pattern on $Mg_xZn_{1-x}O$/r-$Al_2O_3$ structure. Two sets of SAW test devices were fabricated on $Mg_xZn_{1-x}O$ films. One set of delay lines had quarter-wavelength electrode inter-digital transducers (IDTs) with wavelength $\lambda$ = 6, 8 and 10 μm, and the other set of delay lines had split electrode IDTs with $\lambda$ = 12, 16 and 20 μm. A delay line with IDT center to center distance of 1 mm was used for each wavelength, with open-circuit and short-circuit surface (Al pattern on the propagation path). IDT apertures were 180μm for all devices. To excite the Rayleigh-type waves, the test devices were aligned parallel to the c-axis of

the $Mg_xZn_{1-x}O$ film along [0001] direction; while for the Love-type waves, the test devices were aligned perpendicular to the c-axis of the $Mg_xZn_{1-x}O$ film in the $[1\bar{1}00]$ direction. The device fabrication process consists of electron-beam evaporation of ~1400Å Al, followed by photolithography and Al etching to define the IDTs.

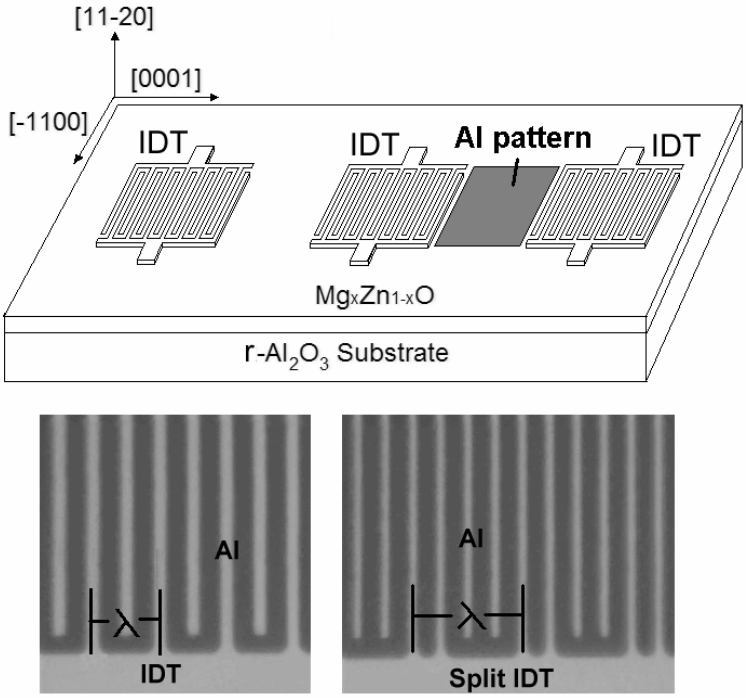


**Figure 4.7.** Schematic and optical images of the SAW test pattern on the a-$Mg_xZn_{1-x}O$/r-$Al_2O_3$ structure. The coordinate axis is identified based on the crystal orientation of the epitaxial a-plane $(11\bar{2}0)$ $Mg_xZn_{1-x}O$ films grown on r-plane $(01\bar{1}2)$ sapphire substrate.

The SAW frequency responses of the devices were measured using an HP 8753D network analyzer and a Cascade Microtech probe station. All the measurements were made on-wafer. The acoustic velocities were calculated from the frequency values at the point of the lowest insertion loss and the fixed wavelength imposed by the inter-digital

pattern modified by the corresponding harmonic number. The error in the velocity calculation is less than 2%.

Shown in figure 4.8 are the time-gated measurement data ($S_{21}$) of a 16-μm SAW test device built on piezoelectric ZnO films. Figure 4.8 (a) shows the effect of post-deposition annealing on the Rayleigh-type SAW characteristics. ZnO films were directly deposited on r-$Al_2O_3$ (without a thin buffer layer) by RF sputtering. Then, the films were annealed in $O_2$ ambient at 600 °C for 2.5 hours. The solid line represents the frequency response of the test device on an as-deposited 1.2-μm thick ZnO film. The center frequency of the Rayleigh wave is 334.4MHz and the insertion loss (IL) is -56.6 dB. The phase velocity of the Rayleigh wave is 5344 m/s. After thermal annealing, the insertion loss of the Rayleigh wave mode decreases and the first harmonic mode of the Rayleigh wave showed up. The dotted line represents the frequency response of the device built on a 1.15-μm thick ZnO film annealed at 600 °C. Here, the center frequency of the Rayleigh wave is 338.7 MHz with IL = - 45.64 dB. The phase velocity of the Rayleigh wave is 5420 m/s. The first harmonic of the Rayleigh wave appears at 1.05 GHz with IL = -24.1 dB. The epitaxial quality of the ZnO film is preferred for SAW propagation as it has low acoustic attenuation loss. The thermal annealing leads to re-crystallization in the film, and therefore improves the film quality. As the result, it decreases the insertion loss of the Rayleigh wave mode and excites high order wave mode.

Figure 4.8 (b) also shows the improved Rayleigh-type SAW characteristics achieved by the hybrid deposition with a ZnO thin buffer layer grown by MOCVD. The sputtering deposited ZnO film thickness is in the range from 1.1μm to 1.2μm. Compared to as-deposited ZnO film without a thin buffer (solid line), as-deposited film with a thin

buffer (dashed line) shows that the insertion loss of the Rayleigh wave mode decreases sharply, and the first harmonic mode of the Rayleigh wave appears at 1.01 GHz with IL = -31.5dB. The best result is obtained from the SAW devices fabricated on a piezoelectric ZnO film with a thin MOCVD buffer and with post-deposition annealing (dotted line), where the peak response of the first harmonic of the Rayleigh wave is 1.05 GHz and the insertion loss is -23.4 dB. It is demonstrated that the MOCVD grown thin buffer provides the template for the subsequent sputtering deposition of a thick piezoelectric a-plane ZnO film while the post deposition annealing further improves crystalline of the sputtered ZnO film. These two factors lead to improving of the SAW performance.

$Mg_xZn_{1-x}O$ allows for flexibility in SAW device design, as its piezoelectric properties can be tailored by controlling the Mg composition. The SAW test devices were fabricated on 2.15-μm thick ZnO, 2.35-μm thick $Mg_{0.08}Zn_{0.92}O$, and 2.2-μm thick $Mg_{0.16}Zn_{0.84}O$ films, all with the MOCVD grown ZnO buffer/r-sapphire structure and post-deposition annealing process. Figure 4.9 shows the measured $S_{21}$ parameters from the network analyzer for a SAW $\lambda$ = 10-μm device built on a piezoelectric $Mg_{0.08}Zn_{0.92}O$ film. The peak response of the Rayleigh wave is 462 MHz; the peak response of the first higher-order Rayleigh mode (the Sezawa wave) is 576 MHz; the peak response of the Love wave is 386 MHz. Correspondingly, the measured SAW velocity for the Rayleigh wave is 4620 m/s, for the Sezawa wave is 5760 m/s, and for the Love wave is 3860 m/s.

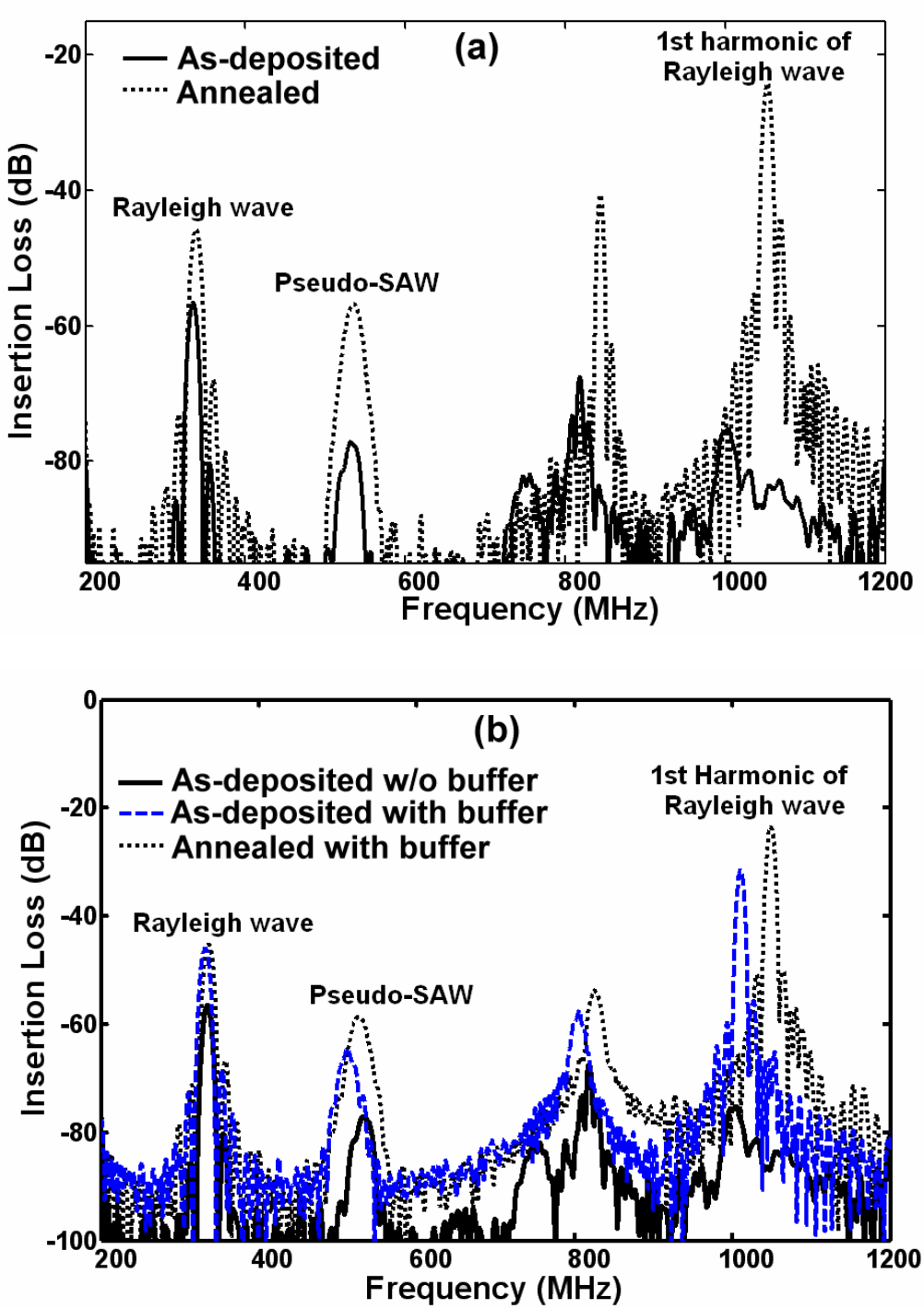


**Figure 4.8.** The time-gated measurement data ($S_{21}$) for the λ = 16-μm SAW test device built on a-ZnO/r-$Al_2O_3$, (a) post-deposition annealing effect without use of a MOCVD grown ZnO buffer; (b) effect from a MOCVD grown thin buffer layer.

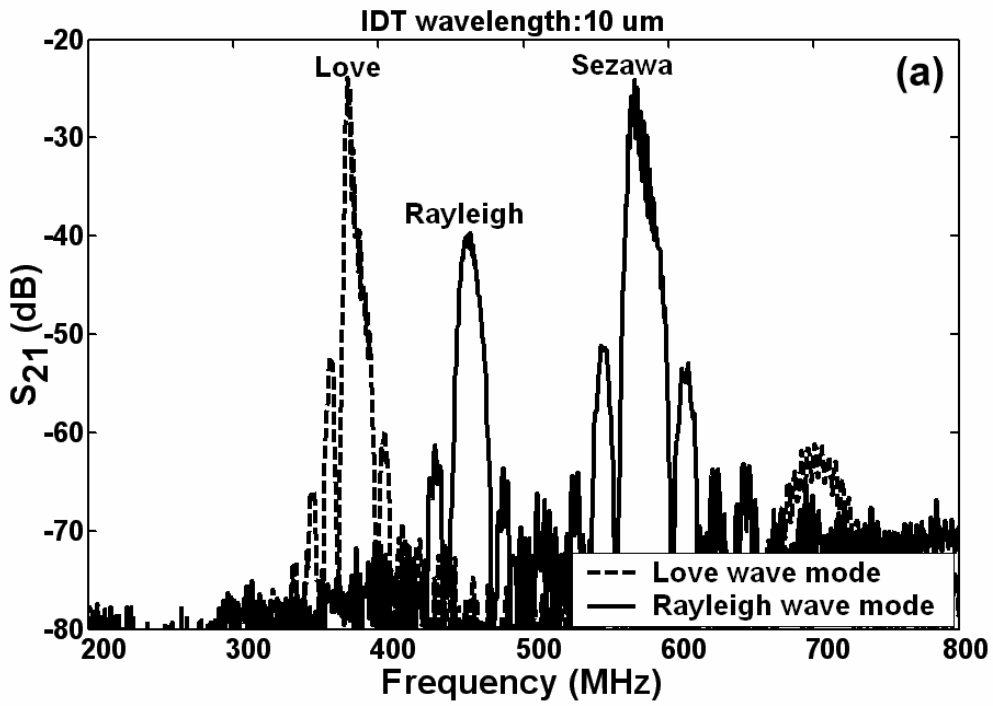


**Figure 4.9.** The measurement data ($S_{21}$) for the $\lambda$ = 10-μm SAW test device built on a-$Mg_{0.08}Zn_{0.92}O$/r-sapphire with a MOCVD grown ZnO buffer and being post-deposition annealed.

Figure 4.10 compares the simulated velocity dispersion and measured velocities of the Rayleigh-type waves in ZnO, $Mg_{0.08}Zn_{0.92}O$, and $Mg_{0.16}Zn_{0.84}O$ films, versus the thickness-frequency product, *hf*. The acoustic velocities of the $Mg_xZn_{1-x}O$/r-$Al_2O_3$ were simulated using Alder's transfer matrix method [113]. The material constants for ZnO, MgO and r-$Al_2O_3$ were obtained from previously published values [117]. Simulation results are plotted with a solid line for ZnO, a dashed line for $Mg_{0.08}Zn_{0.92}O$, and a dotted line for $Mg_{0.16}Zn_{0.84}O$, while the measurement results are plotted with '■' for ZnO, '○' for $Mg_{0.08}Zn_{0.92}O$, and 'Δ' for $Mg_{0.16}Zn_{0.84}O$. It shows that the acoustic velocity increases with the increasing Mg composition in $Mg_xZn_{1-x}O$ films. The in-plane anisotropic

acoustic properties of $Mg_xZn_{1-x}O$/r-$Al_2O_3$ are particularly useful for SAW sensor application: the Rayleigh-type wave is used for gas phase sensing and the Love-type wave for liquid phase sensing.

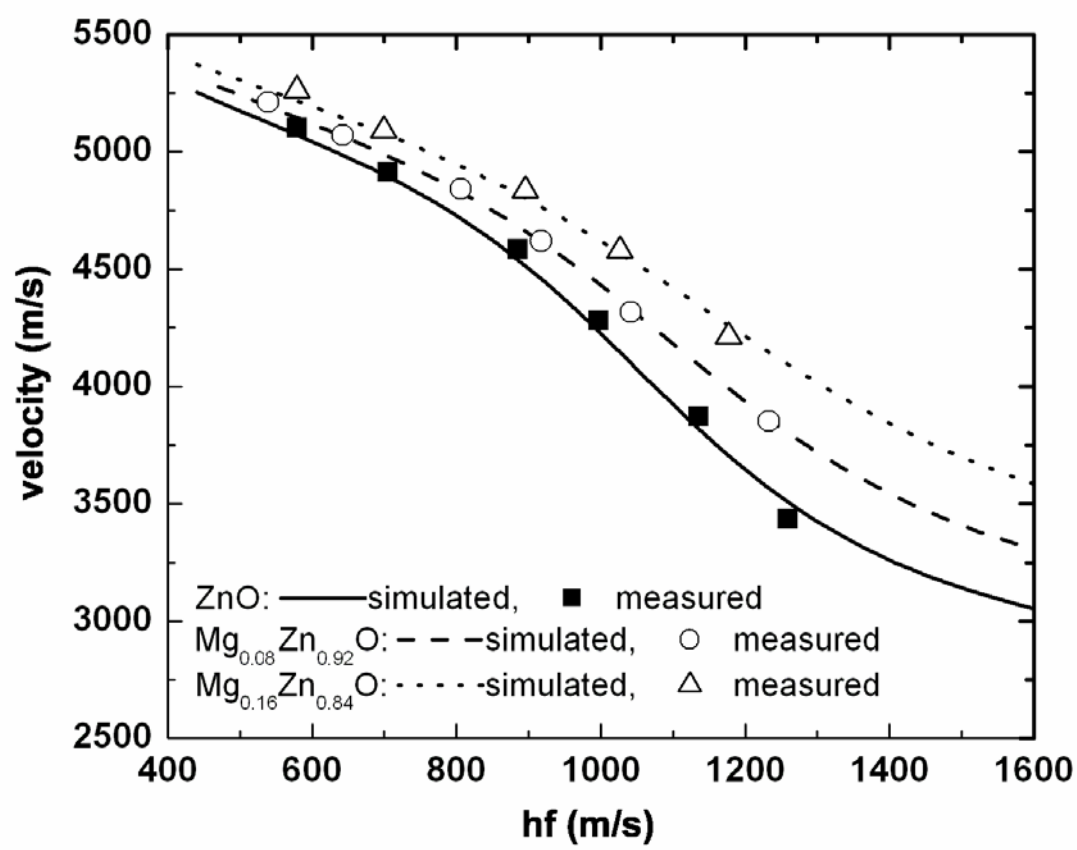


**Figure 4.10.** Comparison of the Rayleigh wave velocities obtained from a 2.15-μm thick ZnO film, 2.35-μm thick $Mg_{0.08}Zn_{0.92}O$ film, and 2.2-μm thick $Mg_{0.16}Zn_{0.84}O$ film deposited on r-$Al_2O_3$ substrates using the hybrid deposition technology.

## 4.4 Summary

The novel hybrid deposition technology which combines the MOCVD and sputtering was developed to deposit piezoelectric a-plane ZnO and its ternary alloy $Mg_xZn_{1-x}O$ films on r-plane $(01\bar{1}2)$ sapphire ($Al_2O_3$) substrates. In the hybrid deposition

process, an ultra-thin ZnO buffer was first grown on r-$Al_2O_3$ by MOCVD technique, followed by a thick piezoelectric $Mg_xZn_{1-x}O$ ($0 \leq x \leq 0.3$) film deposited using RF sputtering. The sputtering targets were made by mixing ZnO and MgO powders in appropriate composition ratio, and NiO powder (2 wt%) was added as the compensation dopants to achieve piezoelectricity. The as-deposited $Mg_xZn_{1-x}O$ films had a-plane $(11\bar{2}0)$ orientation in a wurtzite crystal structure. The crystallinity of the films was further improved by post-annealing at 600°C - 700°C in oxygen ambient. It was found that a ZnO thin buffer layer and post-deposition annealing process significantly improved the film's piezoelectric properties. The c-axis of the $Mg_xZn_{1-x}O$ film lies in the plane of the substrate, resulting in the in-plane anisotropy of the piezoelectric properties. SAW devices were fabricated on the piezoelectric a-plane $Mg_xZn_{1-x}O$ films. The Rayleigh-type waves propagate parallel to the c-axis while the Love-type waves propagate perpendicular to the c-axis. The SAW characteristics in the $Mg_xZn_{1-x}O$/r-$Al_2O_3$ structure were tailored by changing the Mg mole composition in $Mg_xZn_{1-x}O$. Simulation results of the SAW properties were found to be in close agreement with the experimental results. This novel deposition technology improves piezoelectric properties of a-$Mg_xZn_{1-x}O$ ($0 \leq x \leq 0.3$) films on r-$Al_2O_3$ for ZnO based tunable SAW device.

# CHAPTER V. SAW AND ELECTRICAL PROPERTIES IN ZnO/SiC-6H

SiC and ZnO are two main wide band gap semiconductor materials. Due to the low lattice mismatch and similar thermal expansion coefficient between ZnO and SiC, it is technologically possible to grow high quality ZnO/SiC heterostructures. In such structures, the versatility and multifunctionality of ZnO combined with robust physical characteristics of SiC produce many interesting properties, which are suitable for important applications in optoelectronics, RF electronics, MEMS, and sensors, etc. In this chapter, piezoelectric ZnO films were deposited on semi-insulating SiC-6H substrates. The SAW properties in ZnO/SiC-6H were measured and compared with the simulation results. In addition, epitaxial semiconducting ZnO films were grown on c-plane [0001] oriented n-type SiC-6H substrates using MOCVD. The electrical properties in ZnO/SiC-6H heterojunction were studied.

## 5.1 SAW Properties in ZnO/SiC-6H

### *5.1.1 Sputtering Deposition and Film Characterization*

Piezoelectric ZnO films were deposited on the SiC-6H semi-insulating substrates using RF sputtering system for SAW application. As most SAW devices need relatively thick layer of piezoelectric material with compensating doping upto 5%, sputtering deposition offers the advantages to deposit thick films with high deposition rates, and to

obtain heavy compensation doping through the proper target preparation. To achieve good crystal quality and surface morphology, a thin ZnO buffer layer (30nm) was first deposited at a low deposition rate (<10 nm/min) with Ar gas only at ~400 ˚C. Then a thick ZnO film (≥ 1μm) was deposited in the mixed gas atmosphere ($O_2$: Ar = 1:1). Then the samples were annealed at ~600 ˚C in $N_2$ ambient. The SiC-6H substrates were provided by II-VI Incorporated (Pine Brook, NJ).

Figure 5.1(a) shows the FESEM image of a ZnO layer sputtered on SiC-6H semi-insulating substrate, followed by annealing at ~600˚C in $N_2$. A coupled X-ray theta-2theta scan reveals that the film has a primary c-axis orientation, as shown in figure 5.1(b).

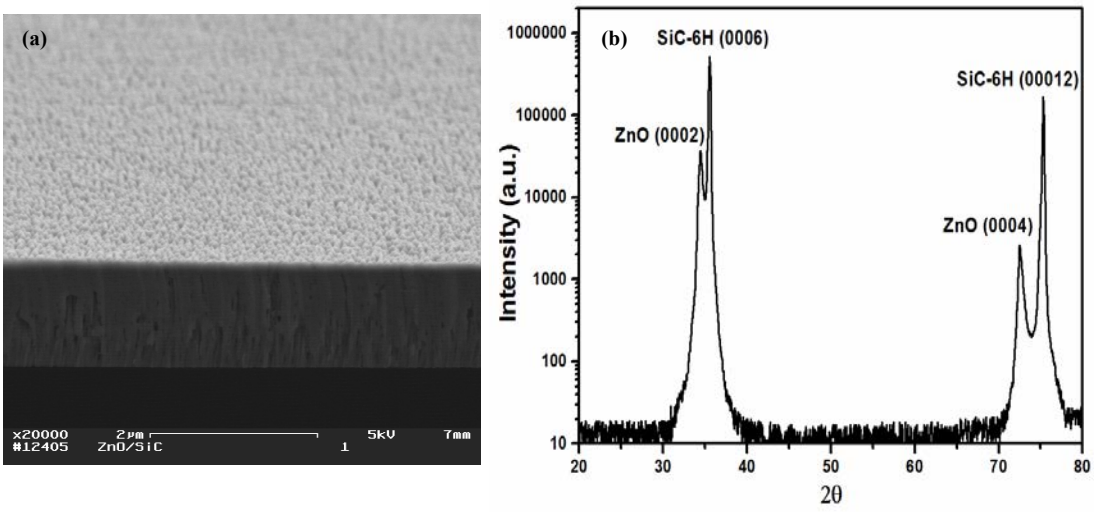


**Figure 5.1.** Structural characterizations of ZnO film deposited on semi-insulating SiC-6H substrates by RF sputtering, (a) FESEM image of dense ZnO film, (b) coupled X-ray scan showing primary c-axis orientation.

*5.1.2 SAW Propagation in ZnO/SiC-6H*

Piezoelectric ZnO films have been used for the excitation of SAW on

nonpiezoelectric substrates for the past 40 years. ZnO films deposited on high SAW velocity and low propagation loss substrates possess several advantages: (i) high coupling coefficient, higher order generalized SAW (GSAW) modes and high velocity pseudo SAW (HVPSAW) modes can be excited; (2) the high frequency SAW filters can be realized using large IDT electrode periodicity with 2μm photolithography tolerance; and (3) this structure is capable of a higher power handling. However, disadvantages of these multi-layer structures are their dispersive velocity characteristic, losses, the added film process control of the SAW properties. Piezoelectric ZnO film on SiC is promising material system for high-frequency SAW device development [50].

Simulation of wave characteristics was performed using a numerical technique developed for multi-layer structures based on a transfer matrix method (as seen in section 3.2). The published material constants of SiC-6H and film ZnO shown in Table 2.1 and 2.3 were used. Both materials, ZnO and SiC-6H are in the point symmetry group 6mm. Figure 5.2 shows the calculated acoustic velocity and electromechanical coupling coefficient v.s. thickness-frequency produce (*hf*), where *h* is the piezoelectric ZnO film thickness and *f* represents the center frequency. The ZnO/SiC-6H structure can propagate high velocity, higher order wave modes (HOWMs) of generalized SAW (GSAW) with larger coupling coefficients.

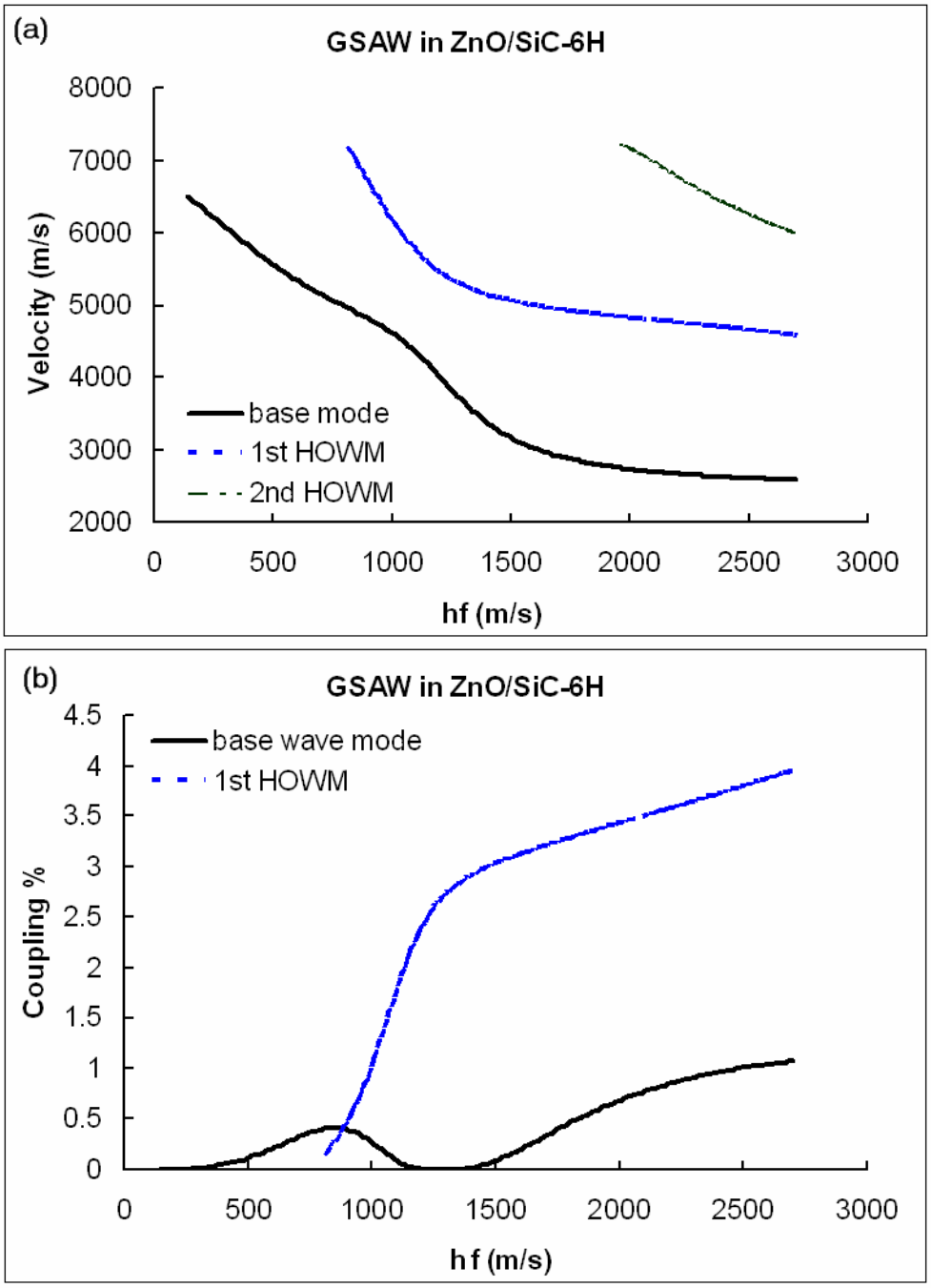


**Figure 5.2.** (a) Acoustic velocity and (b) electromechanical coupling coefficient dispersion v.s. thickness-frequency product of the first two wave modes propagating in the ZnO/SiC-6H system.

Experimental SAW measurements were made with 1.1 ~ 1.4μm thick, sputter-deposited ZnO films on semi-insulating SiC-6H substrates to obtain an initial assessment of the velocity characteristics. The characterization of the SAW propagation properties was performed with a linear array of inter-digital transducer (IDT) structures. Figure 5.3 shows the measured frequency response of a SAW delay line with IDT periodicity of 8 μm and propagation path of 1mm. The 688 MHz peak represents a general SAW mode with velocity about 5500 m/s. The 897MHz peak represents a higher order general SAW mode with velocity about 7176 m/s. The experimental results show dispersion phenomena of SAW velocity in ZnO/SiC-6H structures. The measured velocities of the base GSAW mode range from 5100 m/s to 6200 m/s. The velocities of the second GSAW mode were between 4977 m/s to 6770 m/s. The velocities of HVPSAW were between 7711 m/s to 10,460 m/s. The phase velocities were matched to the previously reported results [50]. The insertion loss can be improved by optimizing the composition and sputtering conditions to achieve low-loss Ni-doped piezoelectric ZnO layers, as well as by using high-resistive SiC-6H substrates.

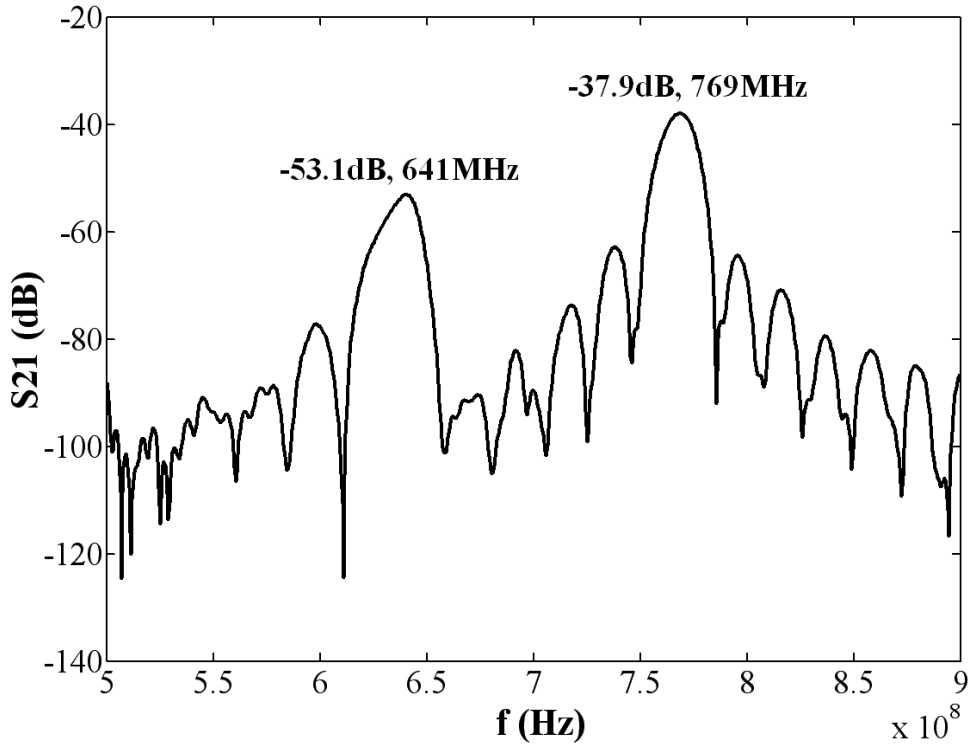


**Figure 5.3.** The time-gated measurement data ($S_{21}$) for the λ = 8-μm SAW test device built on 1.35-μm thick piezoelectric ZnO film on semi-insulating SiC-6H.

Figure 5.4 shows the acoustic velocity dispersion versus thickness-frequency product *hf*. The "Δ" marks the velocities of the base wave mode and "*" represents the first higher order wave mode (HOWM). The experimental velocity dispersion of the GSAW mode is in a good agreement with the results of simulation. The observed discrepancy comes from the resistivity of substrate and unknown material constant $c_{13}$ of SiC-6H.

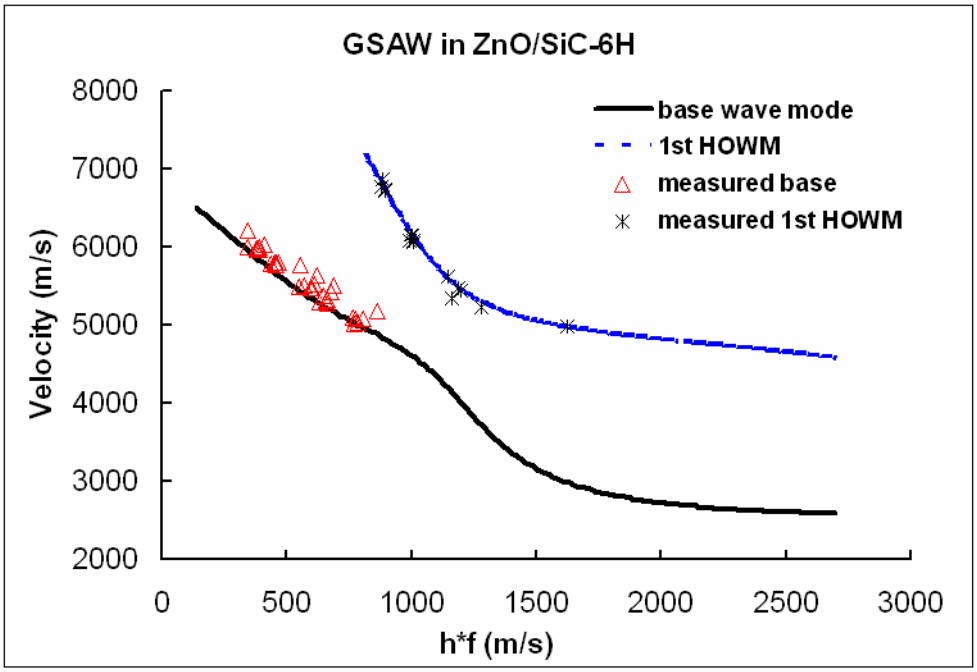


**Figure 5.4.** Comparison of simulated and experimental acoustic velocities of the base wave mode and the first HOWM in ZnO/SiC-6H.

## 5.2 Electrical Properties of ZnO/SiC-6H Heterostructure

*5.2.1 MOCVD and Film Characterization*

SiC-6H has wurzite structure and thermal expansion coefficient similar to ZnO. Lattice mismatch of ZnO on SiC-6H substrate along a-axis is ~5.4% and along c-axis is ~3.3%. Low lattice mismatch of ZnO on SiC-6H substrate should ensure a higher critical thickness of the ZnO thin films before misfit dislocations are produced and the strain relaxation occurs by plastic deformation. This leads to ability of growing high quality ZnO films with low dislocation density. The growth of ZnO thin films on SiC-6H substrate were carried out using MOCVD.

Recently, A. Ashrafi *et al.* reported the ZnO layers grown on 6H-SiC substrates by MOCVD [118]. The as-received 6H-SiC substrates were treated thermally to minimize the nanoscale scratches and fluctuation at 550 ˚C for 30 min by MOCVD. To prevent oxidation of 6H-SiC surfaces, DEZn was supplied during the substrate temperature down to 500 ˚C. The flow rate of DEZn was controlled by adjusting the flow rate of carrier gas $N_2$. The substrate temperature was then increased to a selective temperature of 450 ˚C for successive growth of ZnO layers on the 6H-SiC substrates. The DEZn was flown first for ~10 s and then $O_2$ was flown. The flow rate of DEZn was kept constant to 6.0 sccm while the $O_2$ flow rate was 10 sccm. The epitaxial relationship is (0001) ZnO || (0001)SiC and $[11\bar{2}0]$ ZnO || $[11\bar{2}0]$ SiC. Thickness-dependent strain relaxation and its role on exciton resonance energies of epitaxial ZnO layers grown on 6H-SiC substrates were also reported [119]. Temperature-dependent photoluminescence of ZnO layers grown on 6H-SiC substrate was studied by the same group [120].

ZnO films and nanostructures were grown on n-type SiC-6H substrates at temperatures 400 ~ 500°C. Low-temperature MOCVD growths provide convenience in growth and integration. It is further advantageous to prevent formation of native $SiO_2$ on SiC substrate during pre-exposure to oxygen precursor. We used Rutgers rotating disc MOCVD system to deposit ZnO films on SiC-6H substrates. Diethylzinc ($Zn(C_2H_5)_2$) and oxygen were used as Zn precursor and oxidizer, respectively. One of the primary issues to achieve epitaxial quality films of ZnO is to minimize the native $SiO_2$ thin layer presenting at the surface of the SiC-6H substrate. Due to the presence of native $SiO_2$ the subsequent ZnO growth does not follow the structure of the substrate, resulting in formation of columnar film/tips [121]. However, the formation of columnar ZnO film/

tips can be avoided by substrate pre-treatment and modifying the growth conditions such as gas flow and growth temperature. Native $SiO_2$ can be reduced by treating the SiC substrate with HF solution before the MOCVD growth of ZnO.

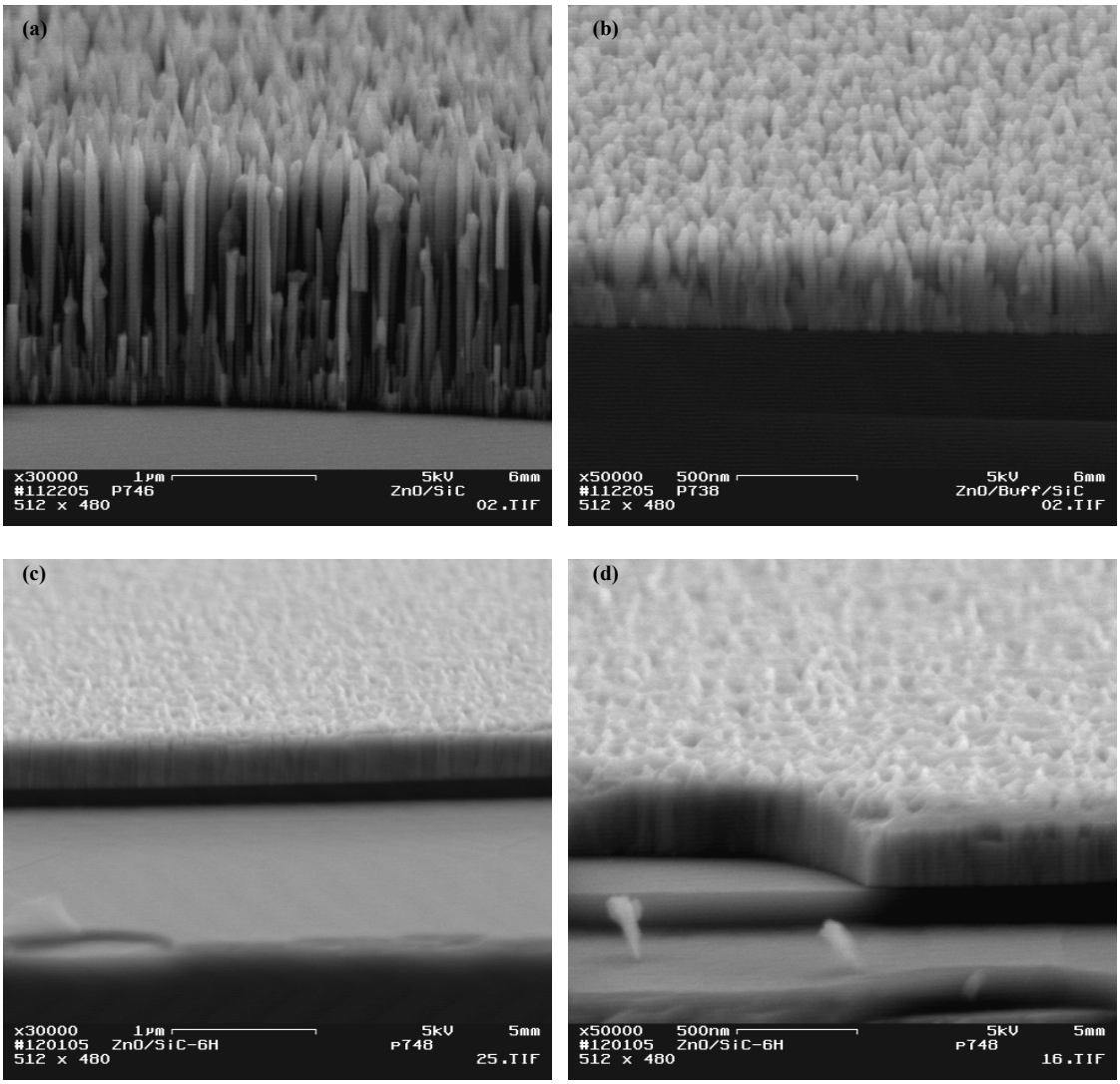


**Figure 5.5.** FESEM images of morphological change in ZnO growth on SiC-6H substrates by MOCVD, a) ZnO nanostructures, b) columnar ZnO film, c) and d) dense and uniform c-oriented polar ZnO films.

ZnO films were characterized for structure, morphology and orientation using FESEM and XRD. Figure 5.5 (a) to (d) shows the FESEM images of the morphological change in ZnO deposited by MOCVD: from c-oriented tip to columnar films, finally leading to formation of dense ZnO epitaxial films. Figure 5.6(a), shows the coupled θ-2θ scan of the ZnO film. The film has primary c-axis orientation and has in-plane registry with the SiC-6H substrate as evidenced by the φ-scan along the {103} family of planes of ZnO shown in Figure 5.6(b). These results indicate that epitaxial quality ZnO films can be achieved on SiC-6H substrates. The large full-width at half maximum (FWHM) of the phi-scan indicates large in-plane mosaic. In-plane mosaic is due to the presence of native $SiO_2$, which can not be completely removed, in the oxygen-based ZnO growth.

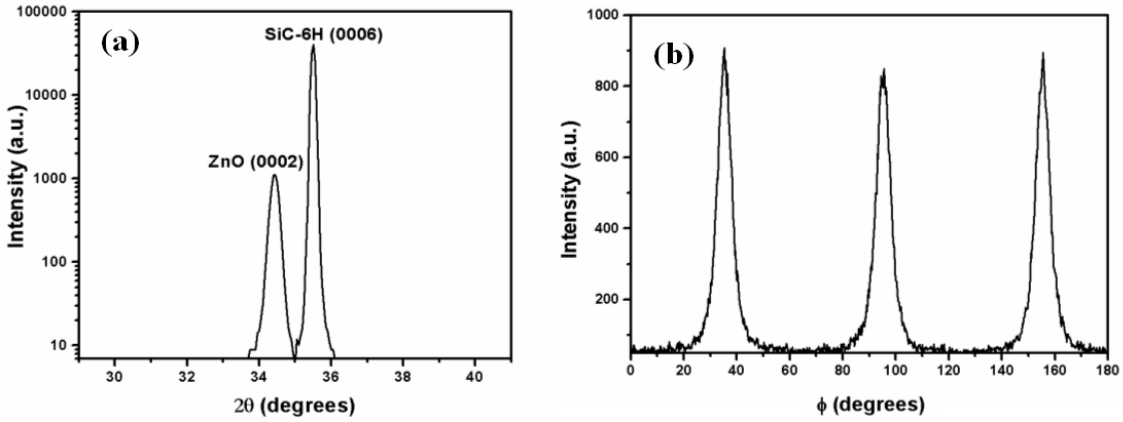


**Figure 5.6.** X-ray characterizations of MOCVD grown ZnO films on SiC-6H substrates, (a) coupled X-ray scan of ZnO films showing the primary-c-axis orientation, (b) X-ray Phi scan along {103} family of planes of ZnO film, indicating in-plane registry with the SiC-6H substrate.

Transparent conducting oxide (TCO) plays a critical role in many optoelectronic devices, such as photovoltaics, liquid crystal displays, plasma displays, and energy efficient windows. ZnO has been emerging as a promising TCO material. In comparison to the popular Indium Tin Oxide (ITO) for the transparent electrodes, Al-doped ZnO (AZO) or Ga-doped ZnO (GZO) offer the advantages such as low cost, non-toxicity and less environmental contamination, chemical stability in hydrogen plasma, ease in processing, and thermal stability. For the first time, we demonstrated GZO films were deposited on n-type SiC-6H substrate to form Schottky barrier diode.

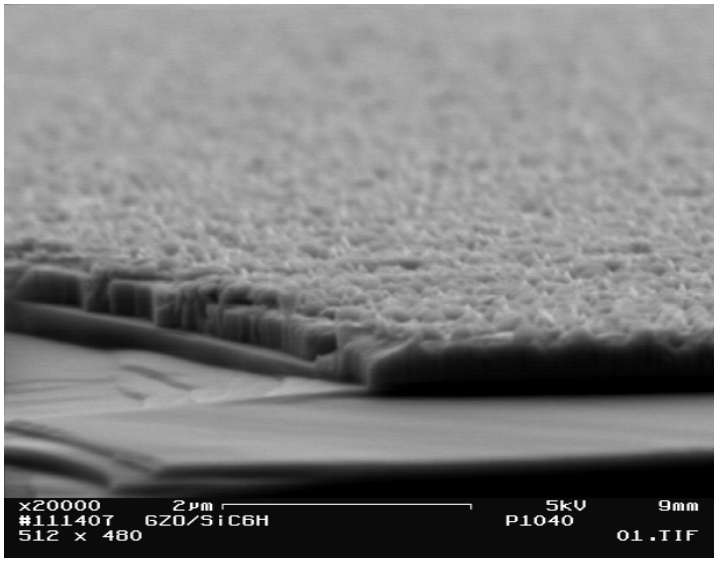


**Figure 5.7.** FESEM image of Ga-doped ZnO film grown on SiC-6H substrates by MOCVD.

The growth of GZO films was carried out in the same MOCVD reactor. Diethylzinc ($Zn(C_2H_5)_2$, DEZn) and oxygen were used as Zn precursor and oxidizer, respectively. Triethylgallium ($Ga(C_2H_5)_3$, TEGa) was used as the Ga doping source. The

metalorganic bubblers were placed in thermal bath tanks and kept at constant temperatures. High purity argon gas flew through the metalorganic bubblers and transported the precursor vapor to the reactor. DEZn and TEGa vapors were premixed before entering the chamber and further diluted by high purity Ar gas. DEZn and TEGa react violently with oxygen and phase reaction may take place even at room temperature. In order to suppress the phase reaction, a high flow of nitrogen was further introduced from the top ceiling of the reactor chamber to push the precursors and oxygen gas downwards to the substrates. A typical morphology of GZO film grown at 480 $^{o}$C is shown in figure 5.7. The GZO films forms a dense film structure with relative smooth surface. Figure 5.8 shows the X-ray theta-2theta scan of GZO films grown on SiC-6H. The intensity of ZnO (0002) is smaller than the intensity of ZnO $(10\ \bar{1}1)$ .

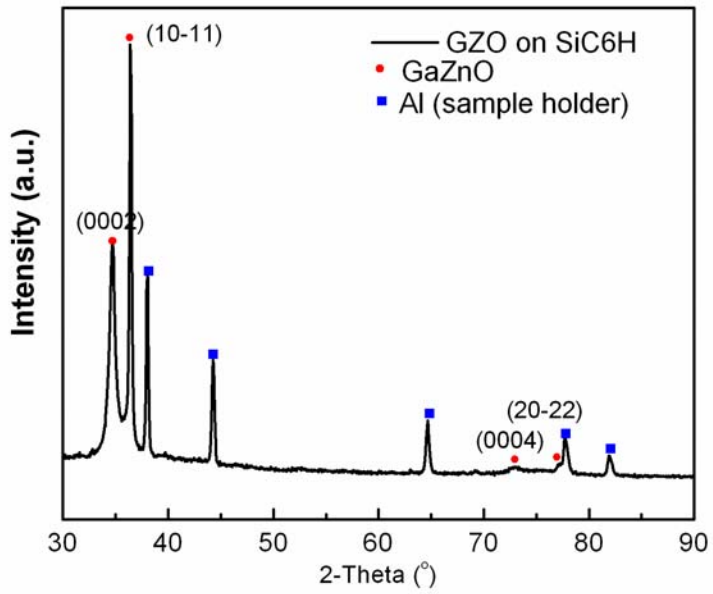


**Figure 5.8.** X-ray scan of MOCVD grown GZO films on SiC-6H substrates.

*5.2.2 Electrical Characterization*

MOCVD grown ZnO films were deposited directly onto the n-type SiC-6H, which served as Schottky contacts. The diode structure, as shown in figure 5.9, consists of ZnO mesa, Ohmic contact onto SiC substrate, and top electrode onto ZnO film. The ZnO mesa structures were fabricated by conventional photolithography method and wet chemical etching using diluted Hydrochloric acid (HCl: $H_2O$ = 1:200). The Ti/Ni two-layer metals were placed on the exposed n-SiC surface as n-type contacts. Finally, Au/Al two-layer metals were deposited on the top of ZnO layer to serve as bonding pads. The diodes were annealed using rapid thermal annealing (RTA) in nitrogen ambience for 1 min at 600 °C. The RTA process used here is to reduce series resistance between Ti/Ni and SiC interface, resulting in better electrical performance. The current-voltage (I-V) characteristics of the fabricated Schottky barrier diode were then measured using an HP4156C semiconductor parameter analyzer.

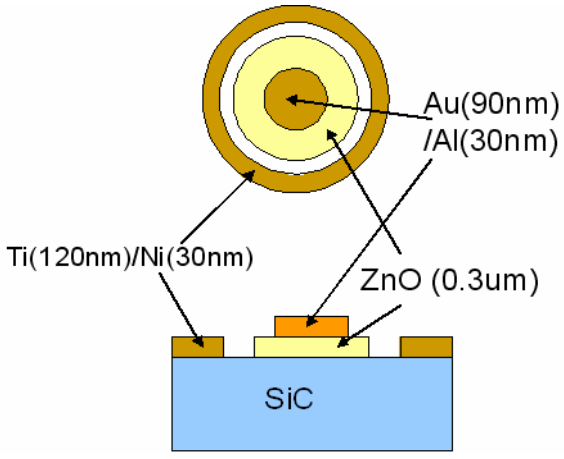


**Figure 5.9.** The schematic of n-ZnO/ n-SiC heterojunction diode.

Figure 5.10 shows the room temperature I-V characteristic of the n-ZnO(450nm) /n-SiC Schottky diode featuring 250μm diameter mesa. The I-V characteristic exhibits a clear rectifying behavior. When the reverse biases are below 5V, the dark currents are well below 2.4 x $10^{-10}$ A. When the forward biases are larger than 2.44V, the forward currents are well above 0.1A. The on-off ratio is about $10^{-7}$. Simulation shows that the diode has an ideality factor of ~1.23. Y. Alivov *et al.* first reported ZnO/SiC-6H heterostructure diodes [122]. The ZnO films were deposited using RF sputtering. The room temperature I-V characteristics exhibited that the forward current at 3V was 0.01 A and the reverse current at -3V was 1 x $10^{-7}$ A. The better performance of our results comes from the epitaxial relationship of MOCVD grown ZnO on SiC and reduced native $SiO_2$ during the deposition.

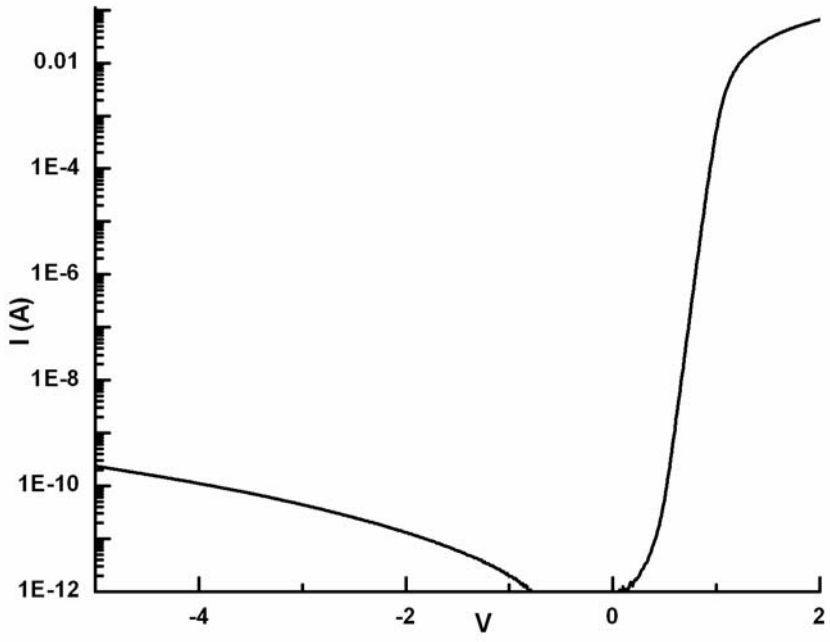


**Figure 5.10.** The room temperature I-V characteristic of n-ZnO/ n-SiC heterojunction diode.

Due to the band offset in a n-ZnO/n-SiC heterojunction, as shown in figure 5.11, which is the sum of the band bending in each material and the Fermi level positions with respect to the conduction band in each material, the room-temperature current-voltage characteristic shows a rectifying heterojunction.

The diode equation is express as:

$$I = I_s[\exp(\frac{qV}{nkT}) - 1] \tag{5.1}$$

where $I_s$ is the saturation current, $n$ the ideality factor, $k$ the Boltzmann constant, and $T$ the absolute temperature. The saturate current in Eq. (5.1) is given by:

$$I_s = A^* T^2 \exp(\frac{-\phi_B}{kT}) \tag{5.2}$$

where $A^*$ is the effective Richardson constant and $\Phi_B$ the barrier height. The forward bias current from Eq. (5.1) was fitted for the saturation current at each temperature. The slope of $\ln(I_s/T^2)$ v.s. $1/kT$ is $-\Phi_B$.

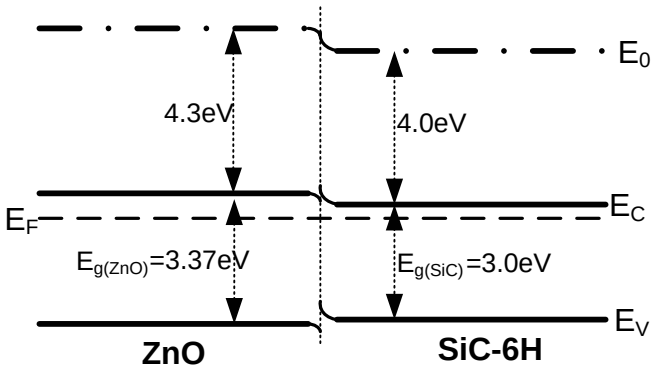


**Figure 5.11.** The schematic of energy band diagram in n-ZnO/n-SiC heterojunction.

The effective barrier heights of n-ZnO/n-SiC can be tentatively determined form the forward I-V-T characteristics. The average value of the reported effective barrier heights was around 1.25 eV [122]. The higher barrier height could be due to the high series resistance caused by the interface status between ZnO and SiC.

Ga-doped ZnO film as a transparent conducting oxide contact was deposited on n-type SiC-6H by MOCVD. Figure 5.12 shows the room temperature I-V characteristic of the GZO(220nm)/n-SiC Schottky diode featuring 350μm diameter mesa. The room temperature I-V characteristic exhibits a clear rectifying behavior, and the forward current at 3V is 0.094A while the reverse current at -3V is 2.25 x $10^{-7}$ A.

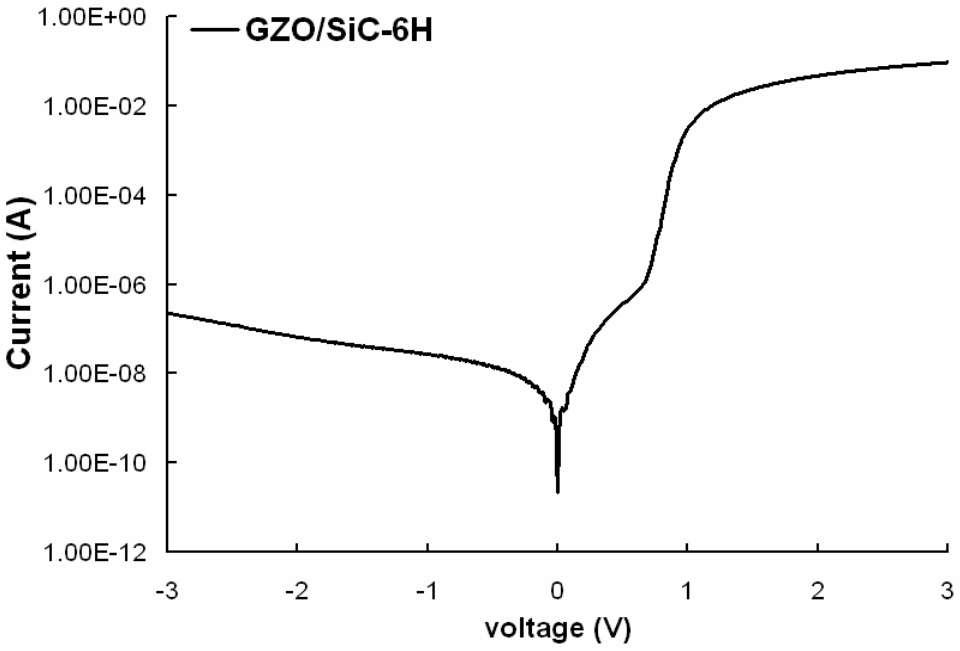


**Figure 5.12.** The room temperature I-V characteristic of GZO/ n-SiC diode.

## 5.3 Summary

In this chapter, we studied heterostructures consisting of the piezoelectric or semiconducting ZnO and SiC. The piezoelectric ZnO films were deposited on semi-

insulating SiC-6H substrates by RF sputtering technique. The SAW propagation properties of ZnO on SiC-6H were theoretically analyzed. The experimental characterization of the SAW velocity properties was performed with a linear array of IDT delay line. The good agreement between the measured and calculated velocities was obtained. ZnO/SiC structure is promising for high frequency SAW devices, which can be used in high-temperature and harsh environments.

In addition, the electrical properties of semiconducting ZnO/SiC heterostructures were studied. The epitaxial ZnO films were grown on SiC-6H substrates by MOCVD. The heterojunction of n-type ZnO film on n-type SiC substrate showed the rectifying characteristics. An Ga-doped ZnO (GZO) film, which serves as a transparent and conductive oxide (TCO) electrode, formed the Schottky contact onto the n-type SiC substrate. Unlike a common Schottky diode which has an opaque metal-semiconductor contact scheme, the top ZnO electrode is transparent, benefiting the optical applications, such as sensors and UV photodetectors. The current results showed the promising potential to integrate the multifunctional (semiconducting, transparent and conducting, and piezoelectric) ZnO and SiC to form the novel devices.

# CHAPTER VI. TFBAR USING $Mg_xZn_{1-x}O$ FILMS ON Si SUBSTRATES

Zinc oxide (ZnO) and its ternary alloy magnesium zinc oxide ($Mg_xZn_{1-x}O$) are piezoelectric materials for bulk acoustic wave (BAW) resonators operating at GHz frequencies. In this chapter, piezoelectric $Mg_xZn_{1-x}O$ based single-mode thin film bulk acoustic resonators (TFBARs) were integrated on Si substrates with an acoustic mirror. First, c-axis oriented piezoelectric $Mg_xZn_{1-x}O$ thin films were deposited on $SiO_2$/Si using RF sputtering technology. Then, the theoretical model of the TFBAR and the concept of tailoring bulk acoustic velocity by controlling Mg composition in the $Mg_xZn_{1-x}O$ film were presented. The feasibility of using ZnO TFBARs for high-mass-sensitive sensor was studied. A prototype of ZnO-TFBAR biosensor integrating with functionalized ZnO nanotips was demonstrated.

## 6.1. Material Growth and Characterization

The c-axis oriented ZnO and $Mg_xZn_{1-x}O$ ($0< x <0.33$) films were deposited using the RF sputtering technique. The sputtering targets were prepared by mixing appropriate quantities of pure ZnO and MgO powders with 2%wt NiO powder. The sputtering process was described in previous chapters. During deposition, the Si substrate was heated at 400 ˚C to achieve good crystal quality and surface morphology.

The surface morphology and geometry of the $Mg_xZn_{1-x}O$ films were characterized using a Leo-Zeiss FESEM. Figure 6.1 shows FESEM images of ZnO and $Mg_{0.2}Zn_{0.8}O$ thin films deposited on the mirror/Si structure. The mirror/Si substrates were provided by

EPCOS(Iselin, NJ). The two-period acoustic mirror structure (750nm $SiO_2$ and 720nm W) is clearly visible, as alternating light and dark layers. The piezoelectric films have a nanocolumnar structure, but are dense and have a sufficiently smooth surface for device fabrication. The image is taken out of the active device region; hence the film is directly on the acoustic mirror, and not on the gold bottom electrode.

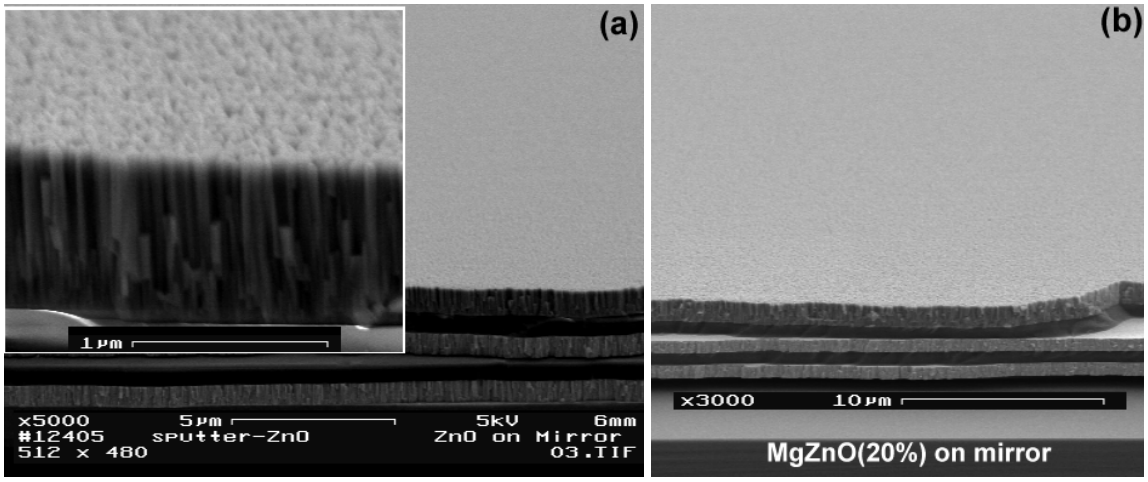


**Figure 6.1.** Cross-sectional FESEM images of (a) ZnO film and (b) $Mg_{0.2}Zn_{0.8}O$ film deposited on the mirror/Si structure. The inset of (a) shows the nanocolumnar ZnO film.

The crystallographic orientation and structural quality of the as-grown films were determined using a Bruker D8 Discover four-circle XRD. Figure 6.2 shows an X-ray θ-2θ scan of ZnO on mirror/Si. With Si (400) peak as reference, ZnO (0002) peak at 2θ about 34.3° is observed, indicating a predominantly c-orientated ZnO (0002) film on the mirror/Si substrate.

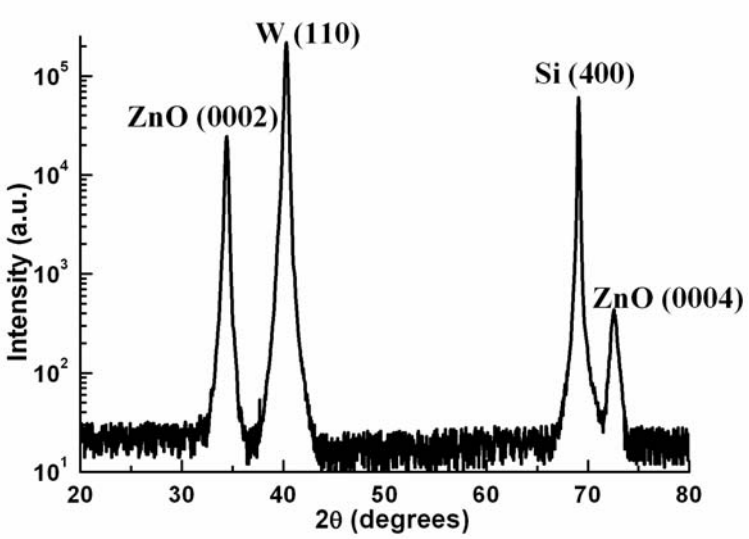


**Figure 6.2.** X-ray θ-2θ scan of piezoelectric ZnO film sputter-deposited on mirror/Si.

The Mg mole composition in the $Mg_xZn_{1-x}O$ film was analyzed using the Rutherford Back-Scattering (RBS) technique. Figure 6.3 shows the RBS spectrum of the $Mg_{0.2}Zn_{0.8}O$ film sputtered on $SiO_2$/Si. The Mg composition, *x*, was determined by fitting the simulated profile to the experimental profile. The mole composition percentage of Mg is about 20%. The mole composition of Ni is 6% in the film.

## 6.2 Fabrication of the Prototype TFBAR

A complete TFBAR device structure consisting of Al/$Mg_xZn_{1-x}O$/Au/acoustic mirror/Si is shown in figure 6.4. Here, Al and Au serve as the top and bottom electrode, respectively. Au is chosen as the bottom electrode as high quality ZnO and $Mg_xZn_{1-x}O$ thin films can be deposited by RF sputtering technique. Al is chosen as the top electrode to minimize electrode mass loading. The acoustic mirror, composed of two periods of alternating quarter-wavelength Bragg reflector, is used to isolate the resonator from the

substrate. RF sputter-deposited $Mg_xZn_{1-x}O$ thin films have a preferred c-axis orientation. When a signal is applied between the top and the bottom electrodes, a longitudinal acoustic wave mode is excited.

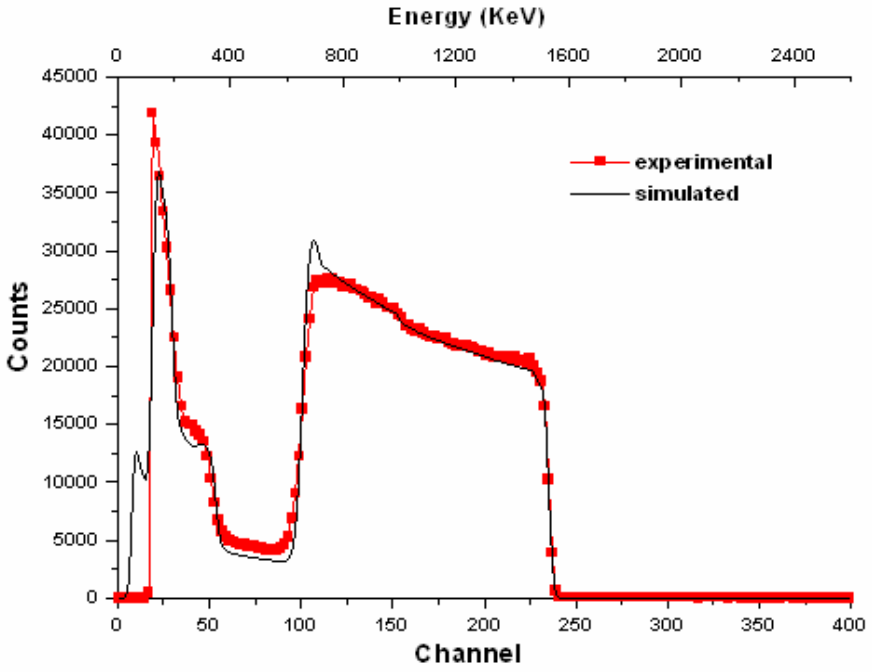


**Figure 6.3.** RBS spectra for Ni-doped $Mg_{0.2}Zn_{0.8}O$ film deposited on $SiO_2$/Si substrate.

The TFBAR fabrication process step is listed as following:

1) Patterning of bottom electrodes on mirror/Si substrate using image reversal photolithography and lift off. A 100nm Au film was deposited on 10nm Cr wetting layer using e-beam evaporation;
2) RF sputtering deposition of Ni-doped ZnO or $Mg_xZn_{1-x}O$ films ( ~ 1.3μm) on patterned substrates;
3) Piezoelectric ZnO or $Mg_xZn_{1-x}O$ mesa formed by wet chemical etching using diluted hydrochloric acid;

4) Deposition of top electrodes (100nm Al) on piezoelectric film using image reversal photolithography and lift off ;

5) Formation of bonding pads (150nm Au) for probe testing.

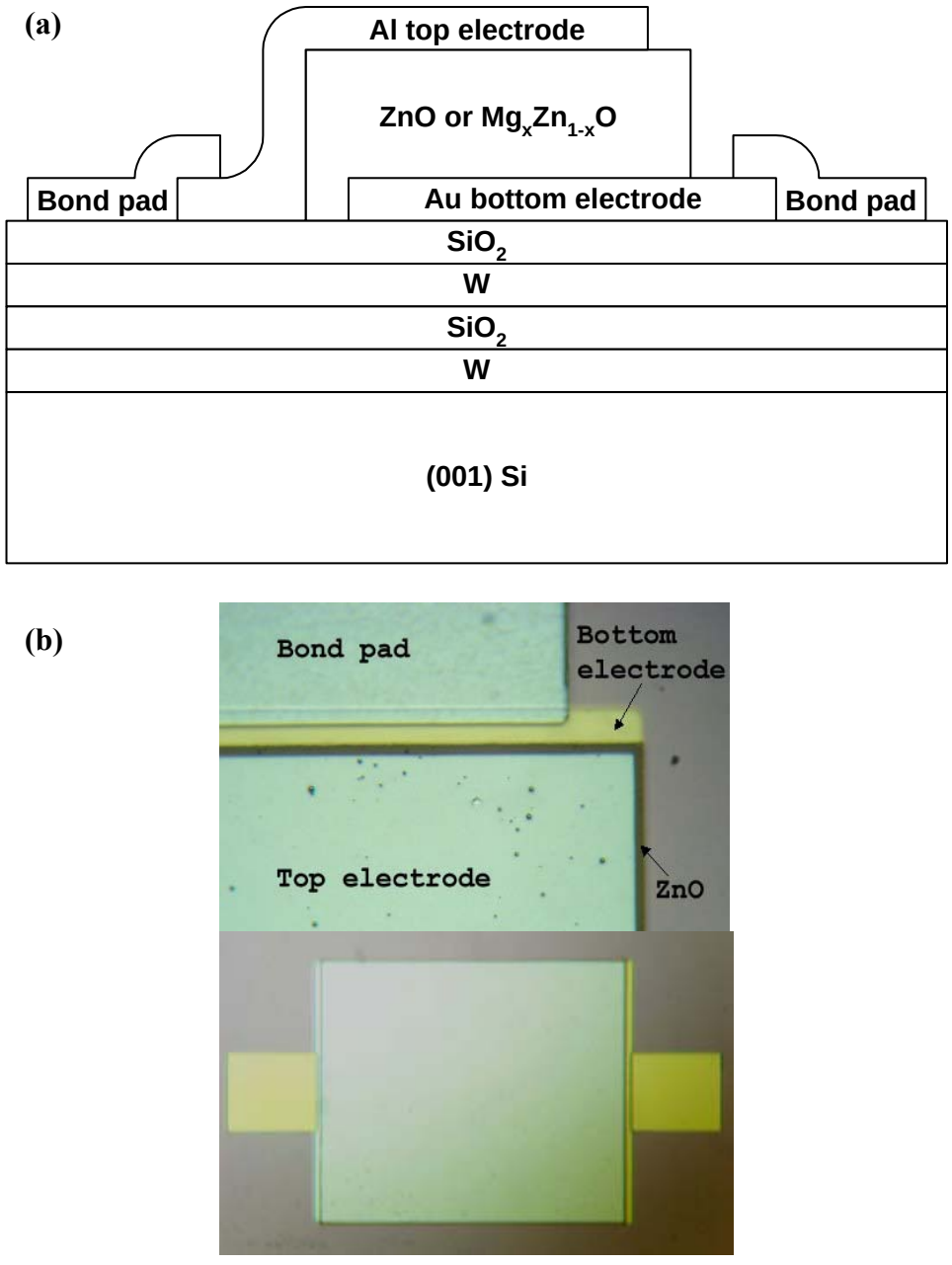


**Figure 6.4.** (a) A schematic diagram of a $Mg_xZn_{1-x}O$ TFBAR structure; and (b) optical microscope pictures and edge details of the TFBAR.

## 6.3 Modeling of Single Mode $Mg_xZn_{1-x}O$ TFBAR on Si

A three-port transmission line analog, in accordance with the Ballato model [123], was used to analyze the acoustic wave behaviors of the $Mg_xZn_{1-x}O$ thin film bulk acoustic resonators on mirror/Si. Figure 6.5 is the representative transmission line model for such a structure. The resonator only excites the longitudinal wave mode. Hence, the circuit model is comprised only of the longitudinal branch. The equivalent circuit model of a composite structure is constructed by a modular building-block approach, wherein each physical entity corresponds to a network feature.

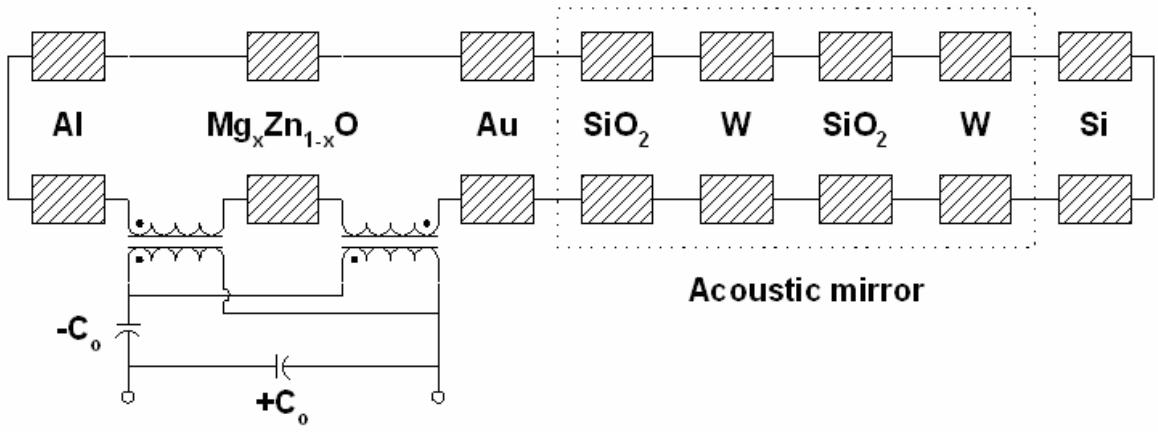


**Figure 6.5.** The transmission line model for the TFBAR structure.

Figure 6.6 shows the simulation for TFBAR structures with and without an acoustic mirror. The piezoelectric ZnO layer is 1.45 μm thick. The active device area is 250μm x 250μm. The dotted line is the input impedance of a ZnO TFBAR on $SiO_2$/Si structure, while the solid line is the impedance of a ZnO TFBAR on mirror/Si structure. As can be seen, the two-period mirror structure isolates the main resonance. However, the simulation suggests that two periods are insufficient to totally suppress spurious

resonances due to the substrate and three-period mirror design is needed. The acoustic impedances of W and $SiO_2$ are 97.40 x $10^6$ kg / (s $m^2$) and 13.25 x $10^6$ kg / (s $m^2$), respectively. The reflectivity of the W – $SiO_2$ interface is:

$$R_{W,SiO2} = \frac{Z_W - Z_{SiO2}}{Z_W + Z_{SiO2}} \approx 0.79 \qquad (6.1)$$

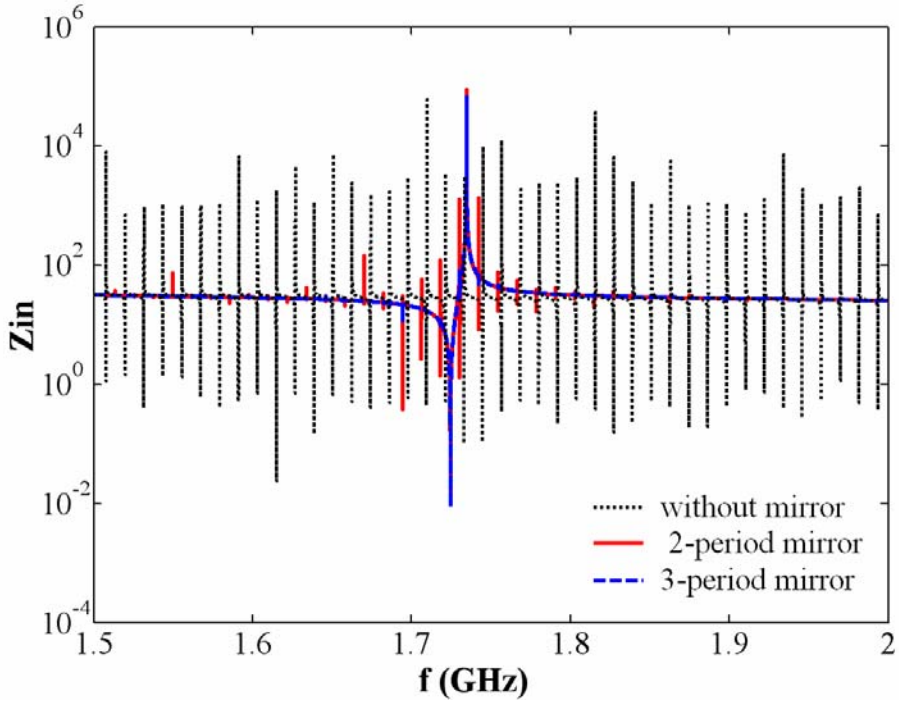


**Figure 6.6.** Impedance of ZnO TFBARs without and with an acoustic mirror on Si substrates.

The frequency response of TFBAR can be tailored by using $Mg_xZn_{1-x}O$ instead of ZnO as the piezoelectric layer. The series resonance frequency is determined by ratio of the bulk acoustic velocity and the piezoelectric film thickness. Figure 6.7 compares the predicted performance of TFBAR (250μm x 250μm) with 1.25μm thick ZnO, $Mg_{0.1}Zn_{0.9}O$ and $Mg_{0.2}Zn_{0.8}O$ piezoelectric layers. The center frequency shifts from 1.91015 GHz for ZnO to 1.9672 GHz for $Mg_{0.1}Zn_{0.9}O$, and to 2.0382 GHz for

$Mg_{0.2}Zn_{0.8}O$. The calculated phase velocity increases 6.7% when the Mg mole composition increases from 0 to 20%.

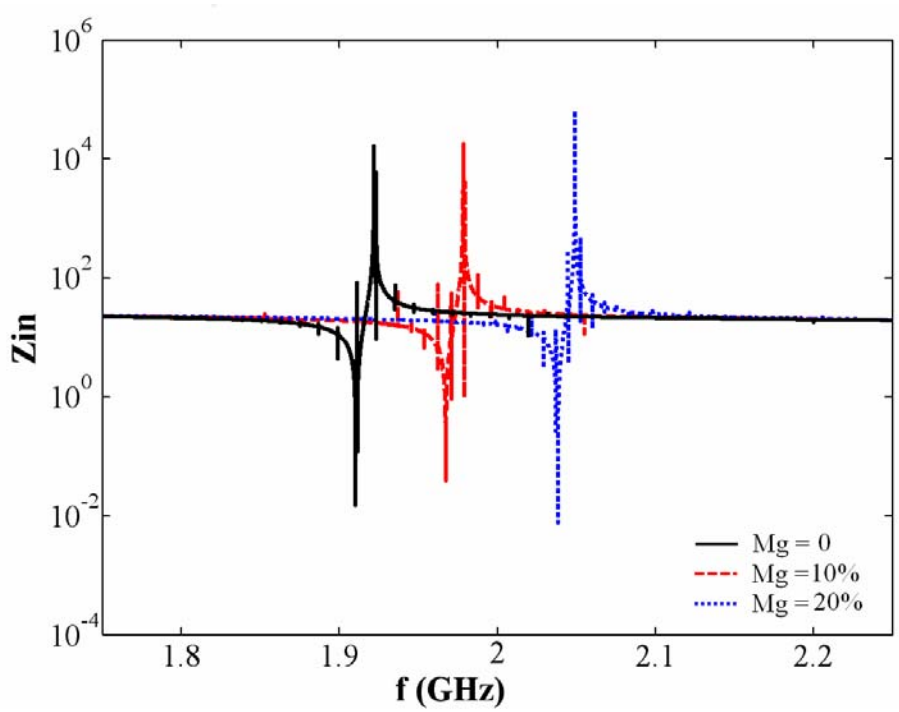


**Figure 6.7.** Impedance of TFBARs using 1.25μm thick ZnO, $Mg_{0.1}Zn_{0.9}O$ and $Mg_{0.2}Zn_{0.8}O$ piezoelectric layers on mirror/Si.

## 6.4 Measurement Results and Discussion

RF characterization of thin film bulk acoustic resonators was conducted using an HP 8573D network analyzer and a Cascade Microtech probe station. The reflection parameter $S_{11}$ of TFBAR was measured and the bulk acoustic velocity was calculated. The frequency shift of measurement error is smaller than 0.04%.

Figure 6.8 shows the $S_{11}$ spectra of $Mg_xZn_{1-x}O$ TFBARs whose device area is 400 μm x 400 μm. The solid line is the frequency response of a TFBAR with 1.12 μm thick

ZnO layer. The resonance frequency is at 2.04875 GHz with $S_{11}$ = -13.14 dB. The dash line represents a TFBAR with 1.25 μm thick $Mg_{0.08}Zn_{0.92}O$ layer. The resonance frequency is at 1.96875 GHz with $S_{11}$ = -21.19 dB. The dotted line presents a $Mg_{0.2}Zn_{0.8}O$ TFBAR with film thickness about 1.38 μm. The resonance frequency is at *f* = 1.916875 GHz and $S_{11}$ = -23.5 dB. The calculated acoustic velocity is 4589 m/s for ZnO, 4922 m/s for $Mg_{0.08}Zn_{0.92}O$, and 5291 m/s for $Mg_{0.2}Zn_{0.8}O$.

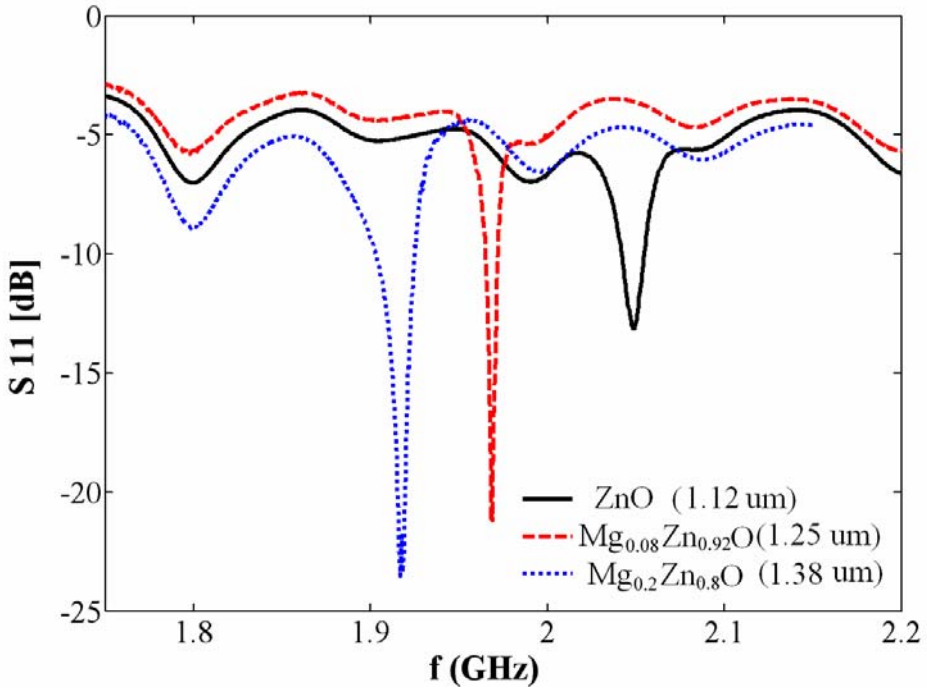


**Figure 6.8.** Measured $S_{11}$ spectra of 400 μm x 400 μm $Mg_xZn_{1-x}O$ TFBARs on mirror/ Si substrates, with x=0, 0.08, and 0.20.

Figure 6.9 shows the simulated performance of TFBAR (400μm x 400μm) with 1.13μm thick ZnO, 1.25μm thick $Mg_{0.08}Zn_{0.92}O$ and 1.37μm thick $Mg_{0.2}Zn_{0.8}O$ layers. The center frequency is 2.0463GHz for ZnO TFBAR, 1.9695 GHz for $Mg_{0.08}Zn_{0.92}O$ TFBAR, and 1.91395 GHz for $Mg_{0.2}Zn_{0.8}O$ TFBAR. Considering that the sputter-

deposited $Mg_xZn_{1-x}O$ film thick variation is ~ 5%, the simulated results are good matched with measurements.

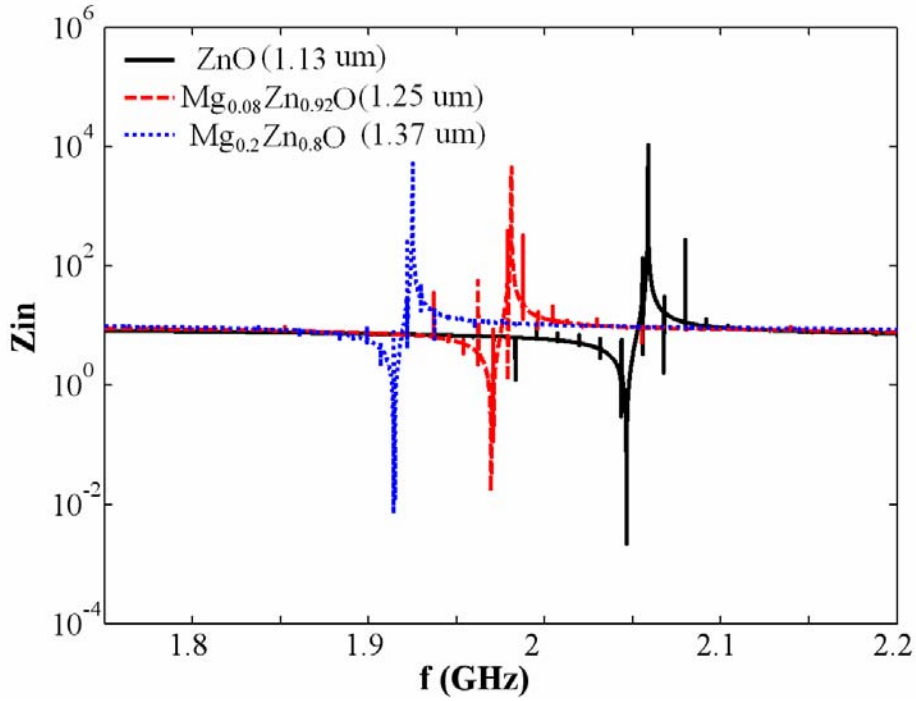


**Figure 6.9.** Simulated impedance of 400 μm x 400 μm $Mg_xZn_{1-x}O$ TFBARs on mirror/ Si substrates, with x=0, 0.08, and 0.20.

## 6.5 Feasibility Study of TFBAR for Biosensor Application

The resonance characteristics of a 150 μm x 150 μm ZnO TFBAR before and after mass-loading is shown in Figure 6.10. The ZnO film thickness is 1.24μm. A 60 nm $SiO_2$ thin film was deposited on the top electrode to investigate the mass-sensitivity. The density of $SiO_2$ deposited by plasma enhanced chemical vapor deposition (PECVD) is 2.3 $g/cm^3$. So $\Delta m/A$ was 13.8 $\mu g/cm^2$. The measured frequency shift ($\Delta f$) was 23.7 MHz. Thus, a mass sensitivity ($S_f$) of 7.6 MHz/ng was achieved.

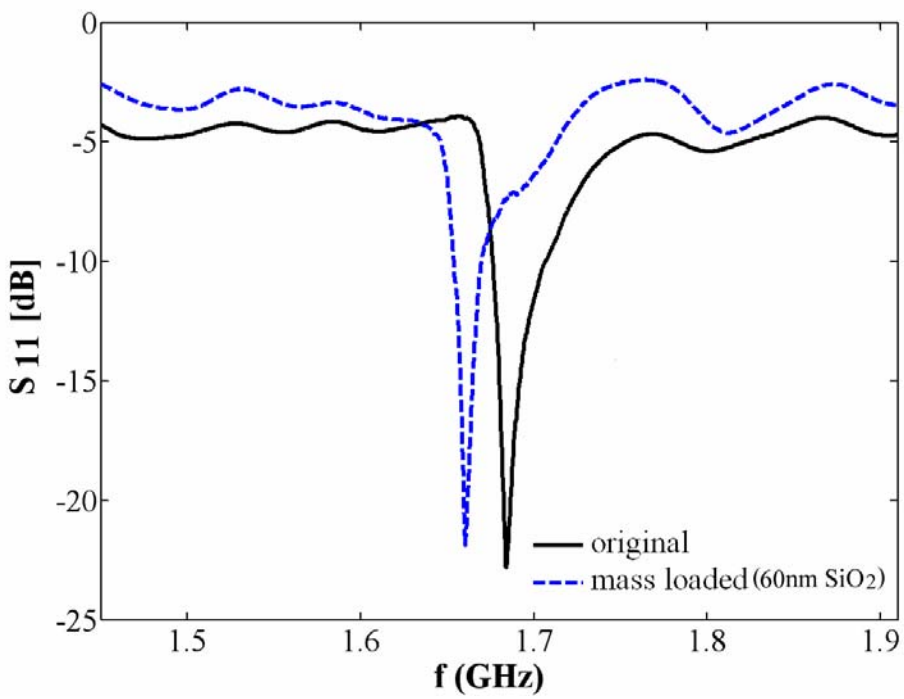


**Figure 6.10.** Measured $S_{11}$ spectra of a 150 μm x 150 μm ZnO TFBAR on mirror/ Si substrate, before and after $SiO_2$ deposition.

Figure 6.11 shows the simulation of mass loading effect. The black solid line represents the impedance before mass is loaded. The blue dotted line is the impedance after 60nm $SiO_2$ layer added. The resonant frequency decreased from 1678.28MHz to 1663.74MHz. The frequency difference was 14.54MHz. The simulated mass sensitivity ($S_f$) was 4.7 MHz/ng. Using Eq. (2.17), the calculated mass sensitivity ($S_f$) was 5 MHz/ng, where $c_{66}$ = 4.43 x $10^{10}$ N/m$^2$, $\rho$ = 5720 kg/m$^3$, and $f_0$ = 1.68394 GHz. So the mass sensitivity ($S_f$*$A$) of the ZnO based 1.67GHz TFBAR was at 5 *KHz cm$^2$/ng* level, which is thousand of times better than that of 10MHz QCM. This ultra-high mass sensitivity is useful for ultra-sensitive-mass loading chemical sensor, biosensor, and environmental sensor applications.

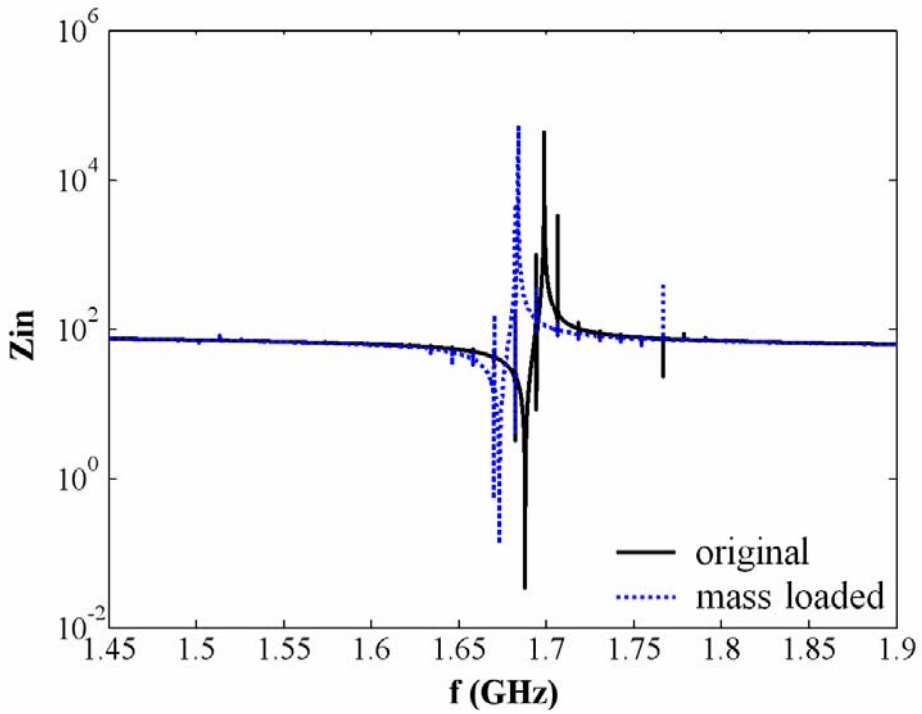


**Figure 6.11.** Simulated impedance of a 150 μm x 150 μm ZnO TFBAR on mirror/ Si substrate, before and after $SiO_2$ (60nm) deposition.

ZnO nanostructures have become one of the most important and useful multifunctional nanostructures. It can be grown at low temperature on various substrates. ZnO nanostructures have been found broad applications in optoelectronics, electronics, catalysts, and especially, for high sensitivity sensor technology. The recent progress in nanoscale science and engineering are promising for the fabrication of novel nano-biosensors with faster response and higher sensitivity and selectivity than that of planar sensor configurations, due to their small dimensions combined with dramatically increased contact surface and strong binding with biological and chemical reagents. Such novel sensors can be used to detect gas absorption and biological molecules interactions of DNA-DNA, DNA-RNA, protein-protein, and protein-small molecules.

ZnO nanostructures were integrated with traditional acoustic devices for gas phase sensing [124-127]. Single crystal ZnO nanobelts were synthesized and deposited onto 36° YX $LiTaO_3$ and 64° YX $LiNbO_3$ SAW devices for gas sensing applications [124]. The sensor response, defined as the change in resonant frequency, showed 3.5 kHz towards 10 ppm $NO_2$ for a 64° $LiNbO_3$ SAW transducer operating at 160°C and 3 kHz towards 1% $H_2$ for a 36° $LiTaO_3$ SAW transducer at 185°C. The ZnO nanowires were distributed onto the electrode surfaces of quartz crystals microbalance (QCM) for ammonia sensing at room temperatures [125]. It was found that the obtained response of the sensors varied with the thickness of the ZnO nanowires layer. ZnO nanowires showed high sensitivity to ammonia in the range of 40–1000 ppm. The response time of the sensor was as fast as ~ 5 s at any concentration (40–1000 ppm) of ammonia gas. ZnO nanorod and nanowire films-coated QCM as a humidity sensor were reported [126,127]. The frequency shift of the ZnO nanostructures coated QCM linearly decreased with increasing humidity. The probe based QCM sensor was equipped with the RF receiver and became a low-cost, real-time wireless QCM gas sensor system, which can be used to monitor the pollutants in harsh environment.

Surface functionalization of ZnO nanostructures in gas or liquid phase has been studied for biochemical sensing application [128]. A nano-SAW sensor, consisting of ZnO nanotips grown on a 128$^o$ Y-cut $LiNbO_3$ SAW delay line was demonstrated [20]. The sensitivity to immobilization was calculated to be $2.2\times10^{-3}$ g/cm$^2$ and the sensitivity to the target second strand DNA oligonucleotide was $1.5\times10^{-3}$ g/cm$^2$. The ZnO nanotip arrays enhanced DNA immobilization by a factor of 200 compared to ZnO films with smooth surface. This device structure possessed the advantages of both traditional SAW

sensors and ZnO nanostructures, and showed promising potential for portable sensors in biological and biomedical applications. A ZnO nanotip-based QCM (Nano-QCM) sensor was developed as a solution for accurate and inexpensive biosensors [129]. The ZnO nanotip coated QCM sensor showed a 10-time larger frequency shift than that of regular QCM sensors, when measuring the same DNA oligonucleotide (5'-AGAAAATCTTAGTGTC-3') solution. Furthermore, the superhydrophilic surface of ZnO nanotip layer significantly boosted the solution taking up ability and enhanced the sensitivity of the QCM sensor.

Compared with QCM, TFBAR has higher sensitivity and can be fabricated in arrays. The reported 2GHz ZnO-based film bulk acoustic resonators for biosensor applications had a higher sensitivity about 2.5 KHz $cm^2$/ng [32, 33, 133]. In addition, acoustic wave sensors integrated with uniformly distributed ZnO nanostructures can efficiently and accurately detect the presence of targets in a given sample due to affinity between molecules and nanostructures. So ZnO TFBAR integrated with ZnO nanotip arrays can be used as biochemical and biomedical sensors with higher sensitivity and selectivity, in comparison with Nano-QCM and traditional TFBAR sensors which use the planar Au sensing surface. ZnO nanostructure-based TFBAR sensors will have new commercial applications, including new methods for the prevention, diagnosis and treatment of diseases; detection of gas phase and liquid phase chemical and biochemical agents, and hazardous chemicals for homeland defense against bioterrorism activities; environmental monitoring and protection.

Figure 6.12 (a) shows the schematic of ZnO nanotips based TFBAR sensor. ZnO nanotips are deposited on the top electrode (Au) of TFBAR. The mass loading effect is

caused by bio-molecules linked on ZnO nanotips, resulting in the resonator frequency shift, as shown in figure 6.12(b). In this work, a prototype of ZnO nanotip based TFBAR biosensor was developed.

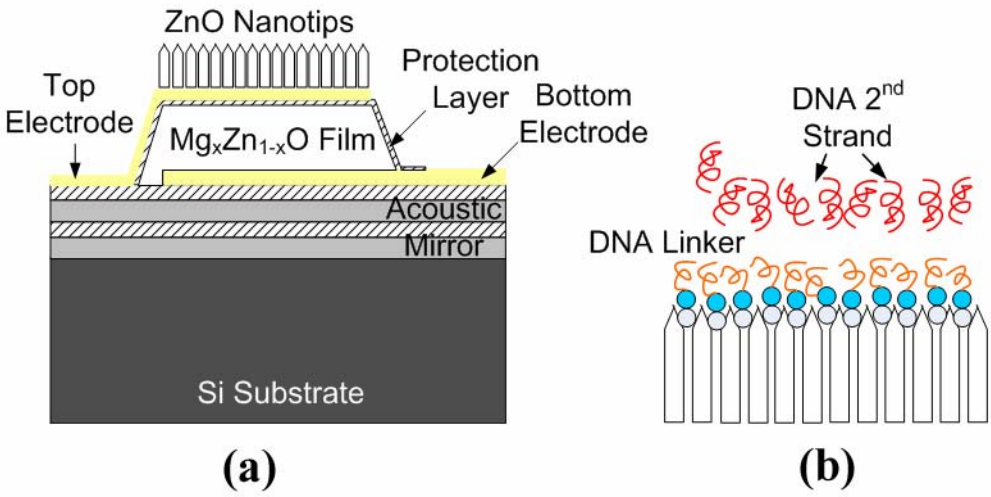


**Figure 6.12** Schematics of (a) ZnO nanotip based TFBAR sensor and (b) DNA immobilization on nanotips.

ZnO nanotips were grown on the top electrode of TFBAR using MOCVD. The ZnO nanotips growth was reported in [130,131]. Figure 6.13 shows the morphology of ZnO layer on Au top electrode of TFBAR. The MOCVD grown ZnO layer is not nanostructure but has rough surface.

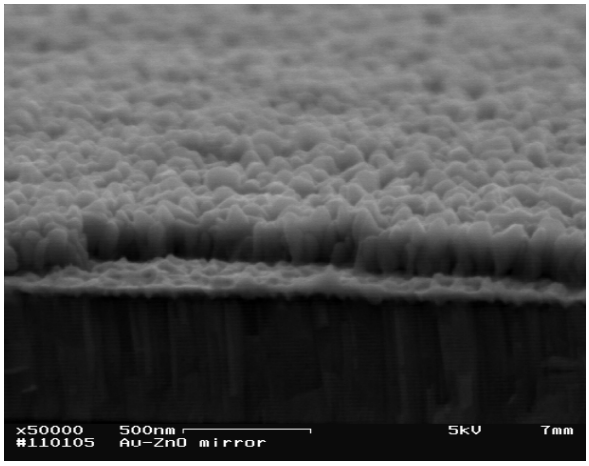


**Figure 6.13.** SEM image of MOCVD grown ZnO layer on Au/piezo-ZnO/Au/mirror/Si.

Figure 6.14 shows the mass loading effect caused by MOCVD grown ZnO layer on TFBAR. The active sensor area of TFBAR was 300μm x 300μm. The black solid line represents the frequency response of original ZnO TFBAR with resonance frequency at 1.664625GHz. The purple dotted line is the frequency response of TFBAR after 60nm thick $SiO_2$ layer deposited on Au by PECVD system. The $SiO_2$ layer was used as the seed layer for ZnO nanotips growth. The resonance frequency is 1.639375GHz. The blue dashed line represents the frequency response of TFBAR with 200nm MOCVD grown ZnO layer. The resonance frequency is reduced to 1.557375 GHz.

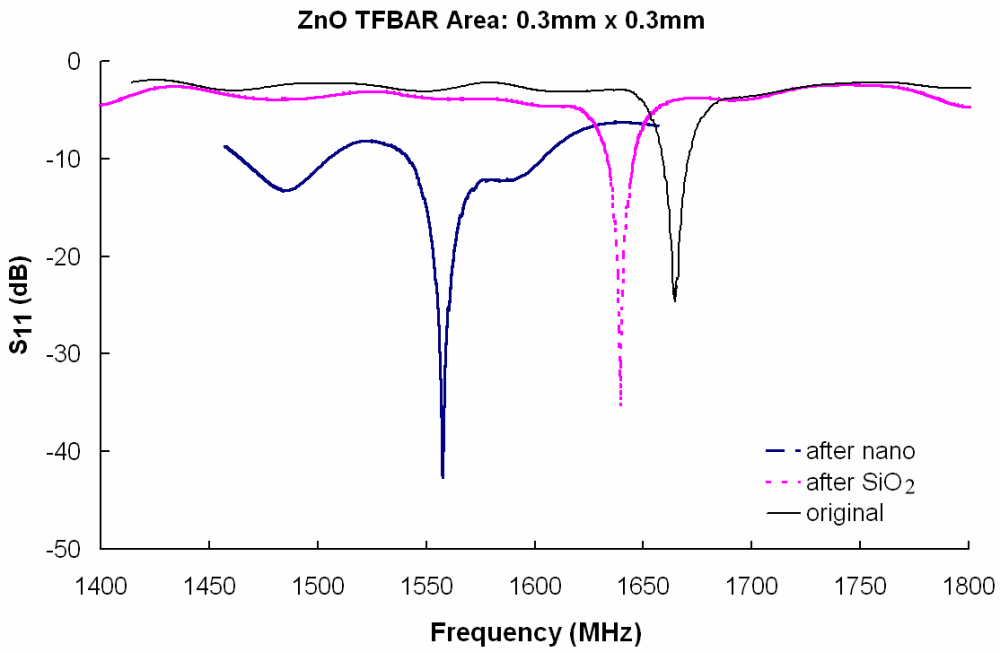


**Figure 6.14.** Frequency shift of ZnO-based TFBAR due to mass-loading effect.

In collaboration with Prof. Elena Galoppini (Chemistry Department, Rutgers University, Newark), a bifunctional linker layer and a biomelecule (DNA) to ZnO nanotips were developed [132]. We used the following schemes and experimental procedures to realize DNA immobilization on ZnO TFBAR.

***Materials:*** 16-Mercaptohexadecanoic acid, 90% (MHDA, Aldrich); Triethanolamine hydrochloride, 99% (TEA-HCl, Aldrich); Reductacryl$^{TM}$ (DTT-resin, Calbiochem); Aldrithiol$^{TM}$-2, 98% (2,2′-dipyridyl disulfide, Aldrich); DIUF water (Fisher); Ethyl alcohol, 200 proof-absolute, Anhydrous, ACS/USP grade (Pharmco); *N*, *N*-dimethylformamide (DMF, Fisher); 1xTE buffer, pH 7.5 (IDTE, IDT Inc), and 1-butanol (Aldrich) were used as received. The 16 bases 5′-thio-modified DNA 5′-/5ThioMC6-D/GTGTTAGCCTCAAGTG-3′ (SH-ssDNA) and complementary 5′-

dye(fluorescein)-modified 5′-/56-FAM/CACTTGAGGCTAACAC-3′ (ssDNA-Fl) DNAs were purchased from Integrated DNA Technologies, Inc.

***Functionalization Scheme 1: SH-based linker:*** In this scheme, the ZnO nanotips were functionalized to attach to thiol-activated DNA, as shown in figure 6.15. We choose 16-mercaptohexadecanoic acid to modify ZnO nanotips and this acid has a relative long molecule for better selective binding for several-step molecule binding.

*Step 1: Formation of sulfhydryl surface with pyridyl groups (figure 6.15. a and b).* Samples were immersed in MHDA + DDT solution overnight (12-15 hr.) in the sealed chamber. The sample was then rinsed thoroughly with butanol and dried in nitrogen.

*Step 2: Immobilization of thiol-activated DNA (figure 6.15. c and d).* For the immobilization step, the samples were immersed in the thiol-activated DNA (ss-DNA) solution for four hours in the sealed chamber. The DNA solution was then rinsed off using PBS buffer (PH=7.5). The sample was dried using nitrogen.

*Step 3: Hybridization with fluorescence-tagged DNA (figure 6.15. e).* The final step was to immerse the samples in fluorescence-tagged ssDNA-Fl solution for 1.5 hours to achieve DNA hybridization. The samples were rinsed with the same PBS buffer and dried under nitrogen flow.

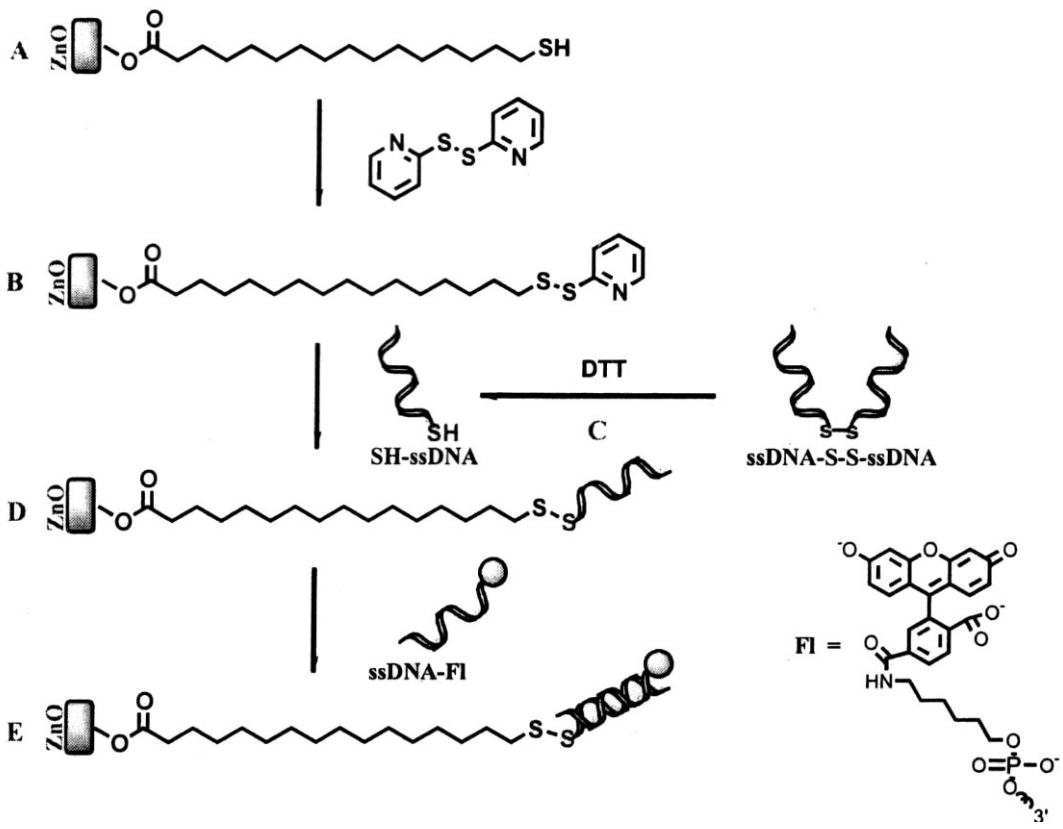


**Fig 6.15.** Schematic presentation of the ZnO nanotips surface modification using SH-based linker: (a) MHDA modified surface (the formation of sulfhydryl surface); (b) an activated sulfhydryl surface with pyridyl groups; (c) a reduction of ssDNA-S-S-ssDNA; (d) an exchange reaction between disulfide surface and sulfhydryl modified DNA (SH-ssDNA); and (e) hybridization of SH-ssDNA modified surface with ssDNA-Fl.

Figure 6.16 shows the frequency shift of ZnO TFBAR using functionalizaiton scheme 1. TFBAR sensing area is 0.25mm * 0.25mm. The solid black line represents the frequency response of TFBAR before step 1. The frequency peak at minimum insertion loss is 1562.8125 MHz. The dashed purple line is the resonance characterization of TFBAR after step1 (SH linker coating). The frequency peak at minimum insertion loss is 1553.75 MHz. The dotted green line is the frequency response measured after step2 (SH-

ssDNA coating). The frequency peak at minimum insertion loss is 1540.9375 MHz. The blue line represents the frequency response measured after step3 (SH-ssDNA-DNAFl). The frequency peak at minimum insertion loss is 1535.9375 MHz. The preliminary results showed that the resonance frequency decreased with increasing mass loaded on top electrode of TFBAR. The total frequency shift was about 26MHz. As the device sensitivity ($S_f$*$A$) is about 1 *KHz* $cm^2/ng$, the loaded mass after step 3 is about 16.25 ng.

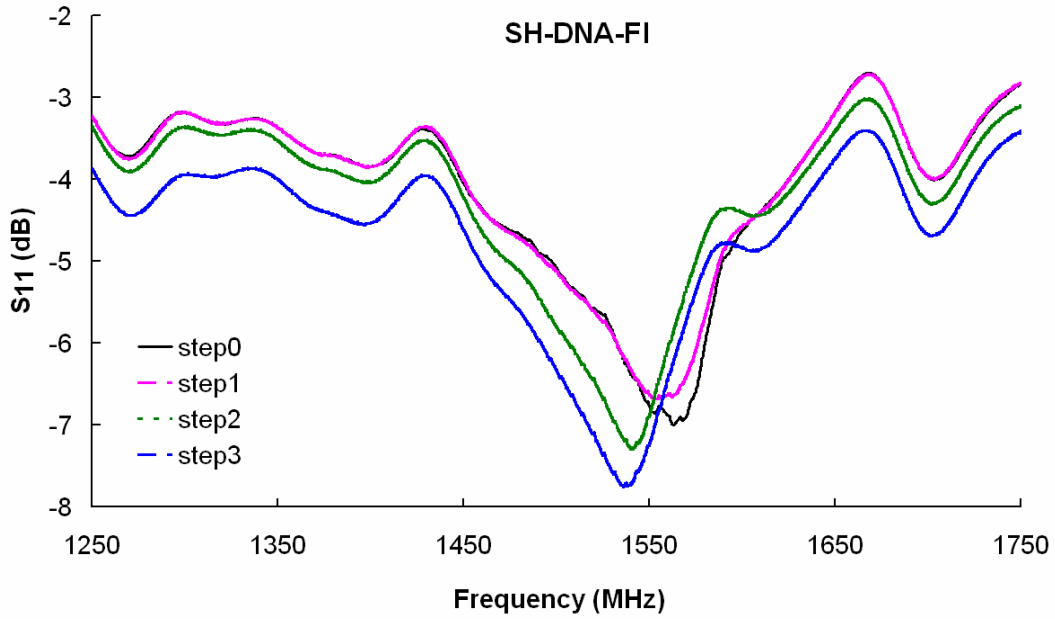


**Figure 6.16.** Frequency shift of ZnO nano-TFBAR where ZnO nanotips were functionalized using SH-based linker.

***Functionalization Scheme 2: $NH_2$-based linker***. An alternative ZnO nanotips surface modification route was shown in figure 6.17.

*Step 1: Formation of N-CPDS-surface (figure 6.16. a).* Samples were immersed in N-CPDS precursor overnight (12-15 h). Afterwards the precursor compound was rinsed thoroughly with butanol. The samples were dried with nitrogen.

*Step 2: Immobilization of amino-modified DNA (figure 6.16. b).* The samples was immersed in amino-activated DNA solution for 4 hours and then rinsed with the same PBS buffer as Scheme 1 and then dried in nitrogen.

*Step 3: Hybridization with fluorescence-tagged DNA (figure 6.16. c).* The final step was to immerse the samples in fluorescence-tagged ssDNA-Fl solution for 1.5 hours to achieve DNA hybridization. The samples were rinsed with the same PBS buffer and dried under nitrogen flow.

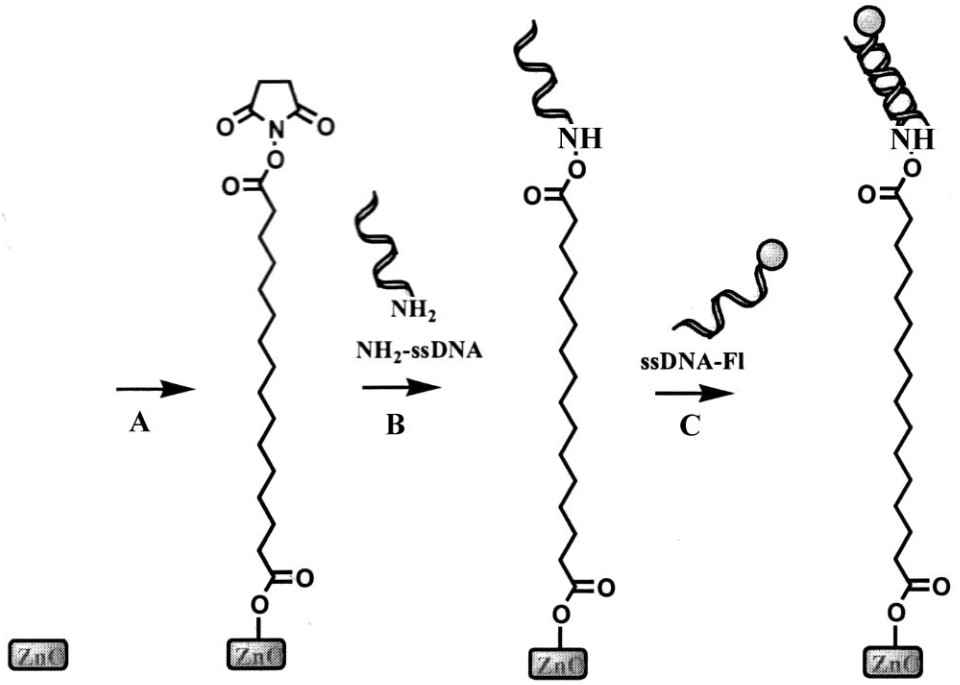


**Fig 6.17.** Schematic presentation of the ZnO nanotips surface modification using $NH_2$-based linker: (a) formation of N-CPDS-surface; (b) immobilization of amino-modified DNA; and (c) hybridization with fluorescence-tagged DNA.

Figure 6.18 shows the frequency shift of ZnO TFBAR using functionalizaiton scheme 2. The solid black line is the frequency response of TFBAR before step 1. The

frequency peak at minimum insertion loss is 1195.9375 MHz. The dashed purple line represents the frequency response ($S_{11}$) of TFBAR measured after step1 ($NH_2$ linker coating). The frequency peak at minimum insertion loss is 1202.5 MHz. The resonance frequency increased after step 1 because ZnO sensing layer was etching by the N-CPDS precursor. The dotted green line is $S_{11}$ of TFBAR measured after step2 ($NH_2$-ssDNA coating). The frequency peak at minimum insertion loss is 1188.125 MHz. The blue line represents $S_{11}$ of TFBAR measured after step3 ($NH_2$-ssDNA-DNAFl coating). The frequency peak at minimum insertion loss is 1184.6875MHz. In this scheme, the PH value of N-CPDS solution needs to be adjusted for the future work.

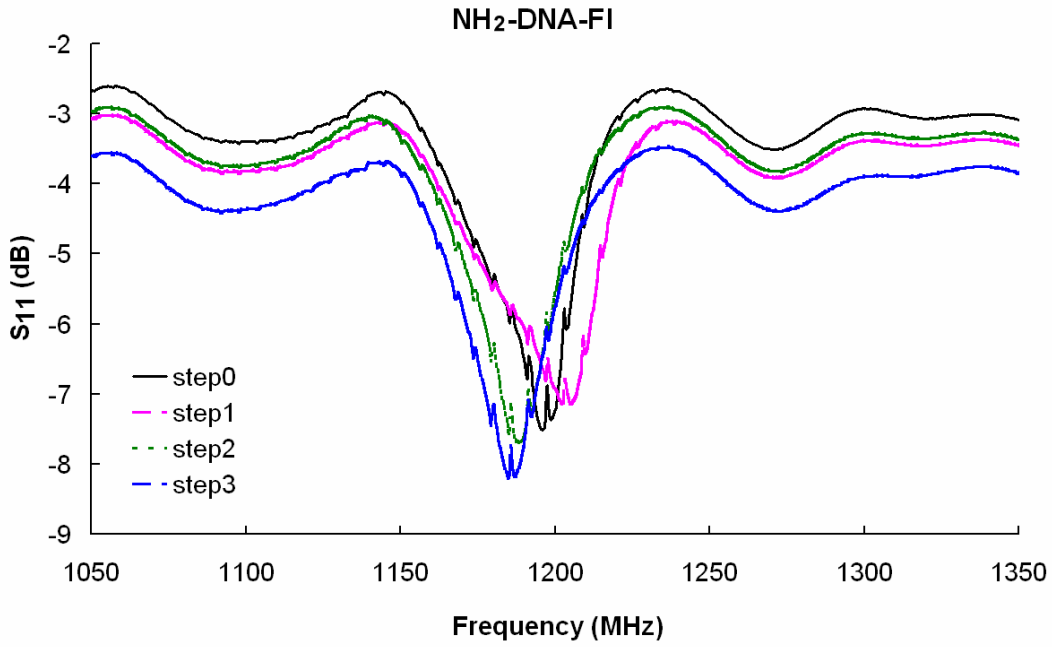


**Figure 6.18.** Frequency shift of ZnO nano-TFBAR where ZnO nanotips were functionalized using $NH_2$-based linker.

## 6.6 Summary

Thin film bulk acoustic resonators using the new piezoelectric material $Mg_xZn_{1-x}O$ were demonstrated on Si substrates with an acoustic mirror, consisting of alternating quarter-wavelength $SiO_2$ and W layers. The c-axis oriented $Mg_xZn_{1-x}O$ thin films were deposited using RF sputtering on mirror/Si substrate. The ability to tailor bulk acoustic wave velocity by changing Mg composition in $Mg_xZn_{1-x}O$ was demonstrated. This allows for further flexibility in TFBAR device design because the resonant frequency can be controlled by the piezoelectric film thickness and Mg composition. The mass sensitivity of ZnO based 1.67GHz TFBAR was found at 5 *KHz* $cm^2/ng$ level, which is thousand of times better than that of QCMs. Not only is the $Mg_xZn_{1-x}O$ TFR a good candidate for BAW devices which can enable next-generation wireless products, but it is also a feasible candidate for ultra-sensitive-mass chemical and biochemical sensor applications. A prototype biosensor by integrating MOCVD grown ZnO nanostructures with TFBAR was demonstrated with high sensitivity.

# CHPATER VII. CONCLUSIONS AND SUGGESTIONS FOR FUTURE WORK

## 7.1 Conclusions

Piezoelectric ZnO thin films were deposited on r-$Al_2O_3$, $Al_xGa_{1-x}N$/c-$Al_2O_3$, SiC-6H, and Si substrates. The films' microstructural properties were characterized using X-ray diffraction (XRD) and field emission scanning electron microscopy (FESEM). The acoustic properties of these multilayer structures were studied through comprehensive characterizations and simulations.

- C-axis oriented piezoelectric ZnO films were deposited on $Al_xGa_{1-x}N$ on c-plane sapphire substrates by RF sputtering technology. For the first time, the piezoelectric properties, including acoustic velocities, electromechanical coupling coefficients, and multiple wave modes in the ZnO/ $Al_xGa_{1-x}N$/c-$Al_2O_3$ were tested and analyzed. We demonstrated the tailoring of surface acoustic wave (SAW) characteristics by varying the Al mole composition in $Al_xGa_{1-x}N$ and by varying the thickness ratio of ZnO to $Al_xGa_{1-x}N$. It was found that the acoustic wave velocity increased and piezoelectric coupling decreased with increasing Al composition in the ZnO/$Al_xGa_{1-x}N$/c-$Al_2O_3$. The thickness-frequency product (*hf*) region where the coupling coefficient of the 2nd and 3rd higher order wave modes are close to the maximum value ($K^2_{max}$) broadens with increasing Al content, while $K^2_{max}$ decreases slightly. In addition, the calculated coupling coefficient increases with the film thickness ratio of $Al_xGa_{1-x}N$ to ZnO in the low *hf* region for the first two basic wave modes. The *hf*

bandwidth of the second and third higher order wave modes broadens with the increasing thickness ratio of $Al_xGa_{1-x}N$ to ZnO. In comparison with a single $Al_xGa_{1-x}N$ film, the ZnO/$Al_xGa_{1-x}N$ multilayer structure generates multiple wave modes, and broadens *hf* bandwidth of the 2nd and 3rd higher order waves. The results indicate that by properly selecting the ZnO/ $Al_xGa_{1-x}N$ ratio, SAW devices with a constant and large coupling coefficient over a wide frequency range can be achieved, which provides the flexibility to design the high velocity, low loss and wide bandwidth SAW devices.

- A novel hybrid deposition technology was developed by using MOCVD of a thin ZnO buffer layer followed by sputtering deposition of a thick piezoelectric $Mg_xZn_{1-x}O$ film to achieve high quality and thick piezoelectric layers on r-$Al_2O_3$ substrates. Introduction of the ZnO thin buffer with a minimum thickness of ~10nm improved the structural quality of thick sputter-deposited $Mg_xZn_{1-x}O$ films. Post-deposition annealing further improved the films' crystallinity and piezoelectric properties. The epitaxial relationship of a-$Mg_xZn_{1-x}O$ film on r-sapphire substrate was retained as $(11\bar{2}0)$ MgZnO || $(01\bar{1}2)$ $Al_2O_3$, and $[0001]$ MgZnO || $[0\bar{1}11]$ $Al_2O_3$. The c-axis lies on the $Mg_xZn_{1-x}O$ growth plane, resulting in the in-plane anisotropy of piezoelectric properties: the Rayleigh-type SAW propagating in parallel to the $Mg_xZn_{1-x}O$ c-axis and the Love-type SAW moving in perpendicular to the $Mg_xZn_{1-x}O$ c-axis. In addition, the SAW characteristics in the $Mg_xZn_{1-x}O$/r-$Al_2O_3$ were tailored by changing the Mg mole composition.
- Piezoelectric ZnO films were deposited on semi-insulating SiC-6H substrate by RF sputtering. The SAW properties of ZnO/SiC-6H were studied. The measured

velocities of the base general SAW mode ranged from 5100 m/s to 6200 m/s. The velocities of the second GSAW mode were between 4977 m/s to 6770 m/s. The velocity values of the pseudo-SAW (PSAW) were between 7711 m/s to 10,460 m/s. It is shown that the ZnO/SiC-6H structure is promising for high frequency and low loss SAW devices. Epitaxial ZnO films were also grown on n-type SiC-6H substrates by MOCVD. We have demonstrated a transparent Schottky diode by depositing a Ga-doped ZnO (GZO) film onto an n-type SiC substrate.

- Thin film bulk acoustic resonators (TFBARs) using piezoelectric ZnO and $Mg_xZn_{1-x}O$ films were built on Si substrates with an acoustic mirror, consisting of alternating quarter-wavelength $SiO_2$ and W layers. The ability to tailor bulk acoustic velocity was demonstrated by controlling Mg composition in $Mg_xZn_{1-x}O$. The mass-loading effect of ZnO TFBAR was studied. It is found that TFBAR has a mass-loading sensitivity of ~ $10^3$ Hz $cm^2$/ng, which is ~ 5 orders of magnitude higher than that of 5MHz QCM (0.057 Hz $cm^2$/ng). The TFBAR can be used for the next-generation of wireless systems; furthermore, it is also promising for the ultra-sensitive chemical and biochemical sensor applications. A prototype of biosensor, which integrates the ZnO nanostructures with TFBAR, has been demonstrated. It greatly enhances the immobilization of DNA and protein molecules.

## 7.2 Suggestions for Future Work

The current research on the piezoelectric ZnO based multilayer structures has generated a series of the novel acoustic devices. In order to improve the device performance and extend their applications, the following work is recommended:

1) It was simulated that higher order wave modes with large coupling coefficients over a wide frequency range could be obtained by integrating the piezoelectric ZnO and $Al_xGa_{1-x}N/c\text{-}Al_2O_3$ ($0 \leq x \leq 1$) structure. The detailed experimental work needs to be done, including design and fabrication of the new SAW devices with properly selected SAW wavelength, film thickness, and Al composition in $Al_xGa_{1-x}N$, and measuring of the electromechanical coupling coefficients.

3). ZnO nanostructures promise the development of novel sensors and sensor arrays with fast responses, high sensitivities, and high selectivity. By integrating ZnO nanostructures with ZnO/SiC SAW devices, a new type of high temperature SAW gas sensors will be developed.

4) We have demonstrated a transparent Schottky diode by integrating a Ga-doped ZnO (GZO) film and an n-type SiC substrate at room temperature. To further develop the GZO/SiC diode as the high temperature sensors and UV detectors, the systematic studies based on electrical and optical characterizations are needed.

5) ZnO nanotips provide excellent binding surfaces in comparison to ZnO films. We have demonstrated a prototype of TFBAR biosensor with a rough ZnO surface. To improve sensitivity of TFBAR biosensor, the MOCVD process needs to be optimized to grow ZnO nanotips on TFBAR surface to form the integrated ZnO nanotip-TFBAR (Nano-TFBAR) devices. The sensitivity and selectivity of Nano-TFBAR will be studied in conjunction with the development of the surface functionalization of ZnO nanotips. The ZnO nanostructure-based TFBAR sensors will enable a wide range of applications, including environmental monitoring and petrochemical sensing.

# REFERENCES


1. B. A. Auld, Acoustic Fields and Waves in Solids, vol.1, 2nd ed. *Krieger Publishing Company, Malabar*, Florida, Appendix 2, 1990
2. C. K. Campbell, Surface Acoustic Wave Devices for Mobile and Wireless Communications, *Academic Press*, 1998
3. C. K. Campbell, Surface Acoustic Wave Devices and Their Signal Processing Applications, *Academic Press*, 1989
4. W. R. Smith and W. F. Pedler, "Fundamental- and Harmonic-frequency Circuit Model Analysis of Interdigital Transducers with Arbitrary Metallization Ratios and Polarity Sequences", *IEEE Transactions on Microwave Theory and Techniques*, vol. 23, pp. 853, 1975
5. Clemens C. W. Ruppel and Tor A. Fjeldly, Advances in Surface Acoustic Wave Technology, Systems, and Applications, *World Scientific Publishing Company*, 2001
6. R. M. Lec, "Piezoelectric Biosensors: Recent Advances and Applications," *Proc. of 2001 IEEE Frequency Control Symposium*, pp. 419, 2001
7. A. J. Ricco and S. J. Martin, "Thin Metal Film Characterization & Chemical Sensors: Monitoring Electronic Conductivity, Mass Loading, and Mechanical Properties with SAW Devices**",** *Thin Solid Films*, vol. 206, pp.94, 1991
8. A. J. Ricco, "SAW Chemical Sensors (Invited)", *The Electrochemical Society Interface*, vol. 3, pp.38, 1994
9. A. J. Ricco, R. M. Crooks, and G. C. Osbourn, "Surface Acoustic Wave Chemical Sensor Arrays: New Chemically Sensitive Interfaces Combined with Novel Cluster Analysis to Detect Volatile Organic Compounds and Mixtures", *Accounts of Chemical Research*, vol. 31, no. 5, pp. 289, 1998
10. J. Kondoh, T. Muramatsu, T. Nakanishi, Y. Matsui, and S. Shiokawa, "Development of Practical Surface Acoustic Wave Liquid Sensing system and Its Application for Measurement of Japanese tea", *Sensors and Actuators B,* vol. 92, pp. 191, 2003
11. O. Tamarin, S. Comeau, C. Déjous, D. Moynet, D. Rebière, J. Bezian, and J. Pistré, "Real Time Device for Biosensing: Design of a Bacteriophage Model Using Love Acoustic Waves", *Biosensors and Bioelectronics*, vol. 18, pp. 755, 2003
12. P. J. Edmonson and C. K. *Campbell*, United States Patent No; US 6,827,281 B2, Dec. 7, 2004
13. W. D. Hunt, D. D. Stubbs, and S. H. Lee, "Time-dependent Signatures of Acoustic Wave Biosensors", *Proc. of the IEEE*, vol. 91, pp. 890, 2003.
14. P. J. Edmonson and C. K. Campbell, US Patent No: US 6,967,428 B2, Nov. 22, 2005
15. V. I. Anisimkin, M. Penza, A. Valentini, F. Quaranta, and L. Vasanelli, "Detection of Combustible Gases by Means of a ZnO-on-Si Surface acoustic Wave (SAW) Delay Line", *Sensors and Actuators B,* vol. 23, pp. 197, 1995

16. S. J. Ippolito, S. Kandasamy, K. Kalantar-zadeh, W. Wlodarski, K. Galatsis, G. Kiriakidis, N. Katsarakis, and M. Suchea, "Highly Sensitive Layered ZnO/$LiNbO_3$ SAW Device with $InO_x$ Selective Layer for $NO_2$ and $H_2$ Gas Sensing", *Sensors and Actuators B*, vol. 111–112, pp.207, 2005

17. S. Ahmadi, F. Hassani, O. Tigli, S. Ahmadi, C. Korman, and M. Zaghloul, **"**Integrated CMOS Surface Acoustic Wave Gas Sensor: Design and Characteristics", *Proc. of 2003 IEEE Sensors*, vol.2, pp.22, 2003

18. K. K. Zadeh, A. Trinchi, W. Wlodarski, and A. Holland, "A Novel Love-mode Device Based on a ZnO/ST-cut Quartz Crystal Structure for Sensing Applications", *Sensors and Actuators A: Physical*, vol. 100, pp. 135, 2002

19. S. Y. Chu, W. Water, and J. Liaw, "An Investigation of the Dependence of ZnO Film on the Sensitivity of Love Mode Sensor in ZnO/quartz Structure", *Ultrasonics,* vol. 41, pp. 133, 2003

20. Z. Zhang, N. W. Emanetoglu, G. Saraf, Y. Chen, P. Wu, J. Zhong, Y. Lu, J. Chen, O. Mirochnitchenko, and M. Inouye, "DNA Immobilization and SAW Response in ZnO Nanotips Grown on $LiNbO_3$ Substrates"**,** *IEEE Trans. on Ultrasonics, Ferroelectrics and Frequency Control*, vol. 53, issue 4, pp. 786, 2006

21. K. M. Lakin, "Thin Film Resonators and Filters", *Proc. of 1999 IEEE Ultrasonics Symposium*, vol. 2, pp. 895, 1999

22. J. F. Rosenbaum, "Bulk Acoustic Wave Theory and Devices", *Artech House*, Boston, 1988

23. H. P. Lobl, M. Klee, C. Metzmacher, W. Brand, and R. Milsom, " Piezoelectric Materials for BAW Resonators", *Proc. of 2001 IEEE Ultrasonics Symposium*, vol. 1, pp. 807, 2001

24. K. M. Lakin, G. R. Kline, R. S. Ketcham, A. R. Landin, W. A. Burkland, K. T. McCarron, S. D. Braymen, and S. G. Burns, "Thin Film Resonator Technology", *Proc. of 1987 IEEE Frequency Control Symposium*, pp.371, 1987

25. S. V. Krishnaswamy, J. Rosenbaum, S. Horwitz, C. Vale, and R. A. Moore, "Film Bulk Acoustic Wave Resonator Technology", *Proc. of 1990 IEEE Ultrasonics Symposium*, pp.529, 1990

26. J. Kaitila, M. Ylilammi, J. Molarius, J.Ella, and T. Makkonen, "ZnO Based Thin Film Bulk Acoustic Wave Filters for EGSM Band**",** *Proc. of 2001 IEEE Ultrasonics Symposium*, pp.803, 2001

27. Y. S. Park, S. Pinkett, J. S. Kenney, and W. D. Hunt, "A 2.4 GHz VCO with an Integrated Acoustic Solidly Mounted Resonator", *Proc. of 2001 IEEE Ultrasonics Symposium*, pp.839, 2001

28. R. Kubo, H. Fujii, H. Kawamura, M. Takeuchi, K. Inoue, Y. Yoshino, T. Makino and S. Arai, "Fabrication of 5GHz Band Film Bulk Acoustic Wave Resonators using ZnO Thin Film**",** *Proc. of 2003 IEEE Ultrasonics Symposium*, pp.166, 2003

29. R. Ruby, P. Bradley, Y. Oshmyansky, A. Chien, and J. D. Larson III, "Thin Film Bulk Wave Acoustic Resonators (FBAR) for Wireless Applications", *Proc. of 2001 IEEE Ultrasonics Symposium*, pp. 813, 2001

30. T. Nishihara, T. Yokoyama, T. Miyashita, and Y. Satoh, "High Performance and Miniature Thin Film Bulk Acoustic Wave Filters for 5 GHz", *Proc. of 2002 IEEE Ultrasonics Symposium*, pp.969, 2002

31. G. Sauerbrey, "Verwendung von Schwingquarzen zur Waegung duenner Schichten und zur Mikrowaegung", *Z Physics*, vol. 155, pp.206, 1959 (in German)

32. R. Gabl, E. Green, M. Schreiter, H. D. Feucht, H. Zeininger, R. Primig, D. Piker, G. Eckstein, W. Wersing, W. Reichl, and J. Runck, "Novel Integrated FBAR Sensors: a Universal Technology Platform for Bio- and Gas-detection", *Proc. of 2003 IEEE Sensors*, vol. 2, pp.1184, 2003

33. R. Gabl, H. D. Feucht, H. Zeininger, G. Eckstein, M. Schreiter, R. Primig, D. Pitzer, and W. Wersing, "First Results on Label-free Detection of DNA and Protein Molecules using a Novel Integrated Sensor Technology Based on Gravimetric Detection Principle", *Biosensors and Bioelectronics*, vol. 19, pp.615, 2004

34. W. Reichl, J. Runck, M. Schreiter, E. Green, and R. Gabl, "Novel Gas Sensors Based on Thin Film Bulk Acoustic Resonators", *Proc. of 2004 IEEE Sensors*, vol.3, pp. 1504, 2004

35. H. Zhang, M. S. Marma, E. S. Kim, C. E. McKenna, and M. E. Thompson, "Implantable Resonant Mass Sensor for Liquid Biochemical Sensing", *Proc. of 17th IEEE International Conference on Micro Electro Mechanical Systems*, pp. 347, 2004

36. L. Mai, D. Kim, M. Yim, and G. Yoon, "A Feasibility Study of ZnO-based FBAR Devices for an Ultra-Mass-Sensitive Sensor Applications", *Microwave and Optical Technology Letters*, vol. 42, no. 6, pp. 505, Sept. 2004

37. S. B. Zhan, S. H. Wei, and A. Zunger, "Intrinsic n-type Versus p-type Doping Asymmetry and the Defect Physics of ZnO", *Physics Review B*, vol. 63, pp. 075205/1, 2001

38. D. C. Look, J. W. Hemsky, and J. R. Sizelove, "Residual Native Shallow Donor in ZnO", *Physics Review Letters*, vol. 82, pp. 2552, 1999

39. V. Srikant, V. Sergo, and D.R. Clarke, "Epitaxial Aluminum-doped Zinc Oxide Thin Films on Sapphire: II, Defect Equilibria and Electrical Properties", *Journal of American Ceramics Society,* vol. 78, pp. 1935, 1995

40. Y. Li, G. S. Tompa, S. Liang, C. R. Gorla, and Y. Lu, "Transparent and Conductive Ga-Doped ZnO Films Grown by Low Pressure Metal Organic Chemical Vapor Deposition", *Journal of Vacuum Science and Technology A*, vol. 15, pp.1063, 1997

41. Z. Jin, T. Fukumura, M. Kawasaki, K. Ando, H. Saito, T. Sekiguchi, Y. Z. Yoo, M. Murakami, Y. Matsumoto, T. Hasegawa, and H. Koinuma, "High Throughput Fabrication of Transition-metal-doped Epitaxial ZnO Thin Films: a Series of Oxide-diluted Magnetic Semiconductors and Their Properties", *Applied Physics Letters*, vol. 78, pp. 3824, 2001

42. J. H. Kim, H. Kim, D. Kim, Y. E. Ihm, and W. K. Choo, “Magnetic Properties of Epitaxially Grown Semiconducting $Zn_{1-x}Co_xO$ Thin Films by Pulsed Laser Deposition”, *Journal of Applied Physics*, vol. 92, pp. 6066, 2002

43. D. H. Hill, D. A. Arena, R. A. Bartynski, P. Wu, G. Saraf, Y. Lu, L. Wielunski, R. Gateau, J. Dvorak, A. Moodenbaugh, and Yung Kee Yeo, “Room Temperature Ferromagnetism in Mn Ion Implanted Epitaxial ZnO Films”, *Physica Status Solidi (a)*, vol. 203, pp. 3836, 2006

44. P. Wu, G. Saraf, Y. Lu, D. H. Hill, R. A. Bartynski, T. Siegrist, M. Ryu, J. A. Raley, and Y. K. Yeo, “Room Temperature Ferromagnetism in Fe-implanted a-plane ZnO Films”, *Applied Physics Letters*, vol. 89, pp. 012508, 2006

45. N. W. Emanetoglu, C.R. Gorla, S. Liang, Y. Liu, Y. Lu, S. Jen, and R. Subramanian, “Epitaxial Growth and Characterization of High Quality ZnO Films for Surface Acoustic Wave Applications”, *Proc. of 1997 IEEE Ultrasonic Symposium*, vol. 1, pp.195, 1997

46. H. Ieki, H. Tanaka, J. Koike, and T. Nishikawa, “Microwave Low Insertion Loss SAW Filter by Using ZnO/sapphire Substrate with Ni Dopant”, *1996 IEEE MTT-S Digest*, pp. 409, 1996

47. J. S. Lee, H. J. Lee, S. H. Seo, and J. S. Park, “Characterization of Undoped and Cu-doped ZnO Films for Surface Acoustic Wave Applications”, *Thin Solid Films*, vol. 398-399, pp.641, 2001

48. T. Mitsuyu, S. Ono, and K. Wasa, "Structures and SAW Properties of RF-Sputtered Single-Crystal Films of ZnO on Sapphire", *Journal of Applied Physics*, vol. 51, no.5, pp. 2464, 1980

49. M. Kadota and M. Minakata, "Piezoelectric Properties of ZnO Films on a Sapphire Substrate Deposited by an RF-Magnetron-Mode ECR Sputtering System", *Jap. Journal of Applied Physics Part 1: Reg. Papers, Short Notes & Review Papers,* vol. 37, no.5B, pp. 2923, 1998

50. I. S. Didenko, F. S. Hickernell, and N. F. Naumenko, "The Experimental and Theoretical Characterization of the SAW Propagation Properties for Zinc Oxide Films on Silicon Carbide", *IEEE Trans. on Ultrasonics, Ferroelectrics and Frequency Control*, vol. 47, no.1, pp.179, 2000

51. D. L. Dreifus, R. J. Higgins, R. B. Henard, R. Almar, and L. P. Solie, "Experimental Observation of High Velocity Pseudo-SAWS in ZnO/Diamond/Si Multilayers", *Proc. of 1997 IEEE Ultrasonics Symposium*, pp. 191, 1997

52. A. Hachigo, H. Nakahata, K. Itakura, S. Fujii, and S. Shikata, "10 GHz Narrow Band SAW Filters using Diamond", *Proc. of 1999 IEEE International Ultrasonics Symposium*, pp. 325, 1999

53. B. S. Panwar, "Characteristics of Surface Acoustic Wave Convolver in the Monolithic Metal–Zinc Oxide–Silicon Nitride–Silicon Dioxide–Silicon Structure", *Applied Physics Letters*, vol. 80, no. 10, pp.1832, 2002

54. F. Moeller, T. Vandahl, D.C. Malocha, N. Schwesinger, and W. Buff, "Properties of Thick ZnO Layers on Oxidized Silicon", *Proc. of 1994 IEEE Ultrasonics Symposium*, pp. 403, 1994

55. Y. Kim, W. D. Hunt, F. S. Hickernell, R. J. Higgins, and C. K. Jen, "ZnO Films on {001}-Cut <110>-Propagating GaAs Substrates for Surface Acoustic Wave Device Applications", *IEEE Trans. on Ultrasonics, Ferroelectrics and Frequency Control*, vol. 42, no. 3, pp.351, 1995

56. T. Gryba, A. Haddou, V. Sadaune, V. Zhang, J. E. Lefebvre, E. Doghech, E. Cattan, and D. Remiens, "Integration of RF Filters on GaAs Substrate", *Proc. of 2001 IEEE Ultrasonics Symposium*, pp. 57, 2001

57. T. Shiba, A. Wham, M. Moteki, Y. Ota, K. Odal, and K. Tsubouchi, "Low Loss SAW Matched Filters With Low Sidelobe Sequences For Spread Spectrum Communications", *Proc. of 1995 IEEE Ultrasonics Symposium*, pp. 107, 1995

58. F.S. Hickernell and E. L. Adler, "The Experimental and Theoretical Characterization of SAW Modes on ST-X Quartz with a Zinc Oxide Film Layer", *Proc. of 1997 IEEE International Ultrasonics Symposium*, pp. 852, 1997

59. M. Kadota and M. Minakata, "Piezoelectric Properties of Zinc Oxide Films on Glass Substrates Deposited by RF-Magnetron-Mode Electron Cyclotron Resonance Sputtering System", *IEEE Trans. on Ultrasonics, Ferroelectrics and Frequency Control*, vol. 42, no. 3, pp.345, 1995

60. M. Kadota and T. Kitamura, "Influence of Leaky Surface Acoustic Wave Velocity of Glass Substrates on Frequency Variation of ZnO/Glass SAW Filters", *IEEE Trans. on Ultrasonics, Ferroelectrics and Frequency Control*, vol.46, no.4, pp.817, 1999

61. A. M. Matteo, V. M. N. Passaro, and M. N. Armenise, "High-Performance Guided-Wave Acoustooptic Bragg Cells in $LiNbO_3$- and GaAs-Based Structures", *IEEE Trans. on Ultrasonics, Ferroelectrics and Frequency Control*, vol. 43, no.2, pp.270, 1996

62. S. J. Chang, Y. K. Su, and Y. P. Shei, "High Quality ZnO Thin Films on InP Substrates Prepared by Radio Frequency Magnetron Sputtering. II. Surface Acoustic Wave Device Fabrication", *Journal of Vacuum Science and Technology A,* vol. 13, no. 2, pp.385, 1995

63. Y. Kim and W. D. Hunt, "An Analysis of Surface Acoustic Wave Propagation in a Piezoelectric Film Over a GaAs/AlGaAs Heterostructure", *Journal of Applied Physics*, vol.71, pp.2136, 1992

64. N. Ashkenov, B. N. Mbenkum, C. Bundesmann, V. Riede, M. Lorenz, D. Spemann, E. M. Kaidashev, A. Kasic, M. Schubert, M. Grundmann, G. Wagner, H. Neumann, V. Darakchieva, H. Arwin, and B. Monemar, "Infrared Dielectric Functions and Phonon Modes of High-quality ZnO Films", *Journal of Applied Physics,* vol. 93, pp. 126, 2003

65. J. G. Gualtieri, J. A. Kosinski, and A. Ballato, "Piezoelectric Materials for Acoustic Wave Applications", *IEEE Trans. on Ultrasonics, Ferroelectrics and Frequency Control*, vol. 41, no. 1, pp. 53-59, Jan. 1994

66. G. Carlotti, G. Socino, A. Petri, and E. Verona, “Elastic Constants of Sputtered ZnO Films”, *Proc. of 1987 IEEE Ultrasonics Symposium*, pp. 295, 1987

67. E. F. Tokarev, I. B. Kobyakov, I. P. Kuzmina, A. N. Lobachev, and G. S. Pado, “Elastic, Dielectric, and Piezoelectric Properties of Zincite in the 4.2–800°K Temperature Range”, *Soviet Physical Solid State*, vol. 17, pp.629, 1975

68. A. Ohtomo, M. Kawasaki, T. Koida, K. Masubuchi, H. Koinuma, Y. Sakurai, Y. Yoshida, T. Yasuda, and Y. Segawa, “$Mg_xZn_{1-x}O$ as a II-VI Widegap Semiconductor Alloy”, *Applied Physics Letters*, vol. 72, no. 19, pp. 2466, 1998

69. A. Ohtomo, M. Kawasaki, I. Ohkubo, H. Koinuma, T. Yasuda, and Y. Segawa, “Structure and Optical Properties of $ZnO/Mg_{0.2}Zn_{0.8}O$ Superlattices”, *Applied Physics Letters*, vol. 75, no. 7, pp. 980, 1999

70. A. K. Sharma, J. Narayan, J. F. Muth, C. W. Teng, C. Jin, A. Kvit, R. M. Kolbas, and O. W. Holland, "Optical and Structural Properties of Epitaxial $Mg_xZn_{1-x}O$ Alloys", *Applied Physics Letters*, vol. 75, no 21, pp. 3327, 1999

71. J. H. Kang, Y. R. Park, and K. J. Kim, "Spectroscopic Ellipsometry Study of $Zn_{1-x}Mg_xO$ Thin Films Deposited on $Al_2O_3(0001)$", *Solid State Communications*, vol. 115, pp.127, 2000

72. T. Minemoto, T. Negami, S. Nishiwaki, H. Takakura, and Y. Hamakawa, "Preparation of $Zn_{1-x}Mg_xO$ Films by Radio Frequency Magnetron Sputtering", *Thin Solid Films*, vol. 372, pp.173, 2000

73. N. W. Emanetoglu, S. Muthukumar, P. Wu, R. H. Wittstruck, Y. Chen, and Y. Lu, “$Mg_xZn_{1-x}O$: a New Piezoelectric Material”, *IEEE Transactions on Ultrasonics, Ferroelectrics and Frequency Control*, vol. 50, pp. 537, 2003

74. R. H. Wittstruck, X. Tong, N. W. Emanetoglu, P. Wu, J. Zhu, Y. Lu, and A. Ballato, "Characterization of $Mg_xZn_{1-x}O$ Bulk Acoustic Wave Devices," *IEEE Transactions on Ultrasonics, Ferroelectrics and Frequency Control*, vol. 50, pp. 1272, 2003

75. H, Nakahata, A. Hachigo, K. Itakura and S. Shikata, “Fabrication of High Frequency SAW Filters From 5 to 10 GHz using $SiO_2$/ZnO/Diamond Structure”, *Proc. of 2000 IEEE Ultrasonics Symposium*, pp. 349, 2000

76. Y, Takagaki, P. V. Santos, E. wiebicke, O. Brandt, H. P. Schönherr, and K. H. Ploog, “Guided Propagation of Surface Acoustic Waves in AlN and GaN Films Grown on 4H-SiC(0001) Substrates”, *Physical Review B*, vol. 66, pp.155439, 2002

77. Th. Pastureaud, A. Soufyane, S. Camou, S. Ballandras, D. Schenck, F. Semond, J.Desbois, and V. Lande, “AlN and GaN Layers Deposited on Sapphires or Silicon Substrates: Theory and Experiment”, *Proc. of 2000 IEEE Ultrasonics Symposium*, pp. 293, 2000

78. Y. Takagaki, P. V. Santos, E. Wiebicke, O. Brandt, H. P. Schönherr, and K. H. Ploog, “Superhigh-frequency Surface-acoustic-wave Transducers using AlN Layers Grown on SiC Substrates”, *Applied Physics Letters*, vol. 81, pp. 2538, 2002

79. N. W. Emanetoglu, G. Patounakis, S. Liang, C. R. Gorla, R. H. Wittstruck, and Y. Lu, “Analysis of SAW Properties of Epitaxial ZnO Films Grown on r-$Al_2O_3$ Substrates,”

*IEEE Trans. on Ultrasonics, Ferroelectrics and Frequency Control*, vol.48, n.5, pp. 1389, 2001

80. H. Ieki and M. Kadota, "ZnO Thin Films for High Frequency SAW Devices", *Proc. of 1999 IEEE Ultrasonic Symposium*, pp. 281, 1999
81. T. Palacios, F. Calle, J. Grajal, E. Monroy, M. Eickhoff, O. Amvacher, and F. Omnes, "High Frequency SAW Devices on AlGaN: Fabrication, Characterization and Integration with Optoelectronics", *Proc. of 2002 IEEE Ultrasonics Symposium*, pp. 55, 2002
82. P. Sharma, S. Kumai, and K. Sreenivas, "Interaction of Surface Acoustic Waves and Ultraviolet Light in ZnO Films", *Journal of Materials Research*, vol.18, no. 3, pp. 545, 2003
83. T. Y. Lin, Y. M. Sheu, Y. F. Chen, J. Y. Lin, and H. X. Jiang, "Optical Properties of GaN/AlN Multiple Quantum Wells", *Solid State Communications*, vol. 131, pp. 389, 2004
84. L. Shen, S. Heikman, B. Moran, R. Coffie, N. Q. Zhang, D. Buttari, I. P. Smorchkova, S. Keller, S. P. Denbaars, and U. K. Mishra, "AlGaN/AlN/GaN High-power Microwave HEMT", *IEEE Electron Device Letters*, vol. 22, no. 10, pp. 457, 2001
85. C. Deger, E. Born, H. Angerer, O. Ambacher, M. Stutzmann, J. Hornsteiner, E. Riha, and G. Fischerauer, "Sound Velocity of $Al_xGa_{1-x}N$ Thin Films Obtained by Surface Acoustic Wave Measurements", *Applied Physics Letters*, vol. 72, pp. 2400, 1998
86. S. Nakamura and G. Fasol, "The Blue Laser Diode: GaN Based Light Emitters and Lasers", *Springer*, Berlin, 1997
87. K. Uehara and C.M.Yang, "AlN Epitaxial Film with Atomically Flat Surface for GHz-Band SAW Devices", *Proc. of 2002 IEEE Ultrasonic Symposium*, pp.135, 1999
88. K. Tsubouchi, K. Sugai, and N. Mikoshiba, "Zero Temperature Coefficient Surface-acoustic-wave Devices Using Epitaxial AlN Films", *Proc. of 1982 Ultrasonics Symposium*, pp. 340, 1982
89. S. Lee, H. Jeong, S. Bae, H. Choi, J. Lee, and Y. Lee, "Epitaxially Grown GaN Thin-film SAW Filter with High Velocity and Low Insertion Loss", *IEEE Trans. on Ultrasonics, Ferroelectrics and Frequency Control*, vol. 48, no. 3, pp. 524, 2001
90. Y. J. Kim, G. H. Lim, K. H. Choi, S. J. Chung, H. J. Kim, H. Park, and H. S. Park, "SAW Characteristics of GaN Epitaxial Films Deposited on Different Plane Sapphire Substrates Using MOCVD", *Proc. of 2002 IEEE Ultrasonics Symposium*, pp.412, 2002
91. P. Tobias, B. Golding, and R. N. Ghosh, "Interface States in High-temperature Gas Sensors Based on Silicon Carbide", *IEEE Sensor Journal*, vol. 2, no. 5, pp. 543, 2003
92. A. Trinchi, K. Galatsis, W. Wlodarski, and Y. X. Li, "A Pt/$Ga_2O_3$-ZnO/SiC Schottky Diode-based Hydrocarbon Gas Sensor", *IEEE Sensor Journal*, vol. 3, no. 5, pp. 548, 2003

93. K. Kalantar-zadeh, A. Trinchi, W. Wlodarski, A. Holland, and M.Z.Atashbar, "A Novel Love Mode Devices with Nanocrystalline ZnO Film for Gas Sensing Applications", *Proc. of 1st IEEE Conference Nanotechnology,* pp. 556, 2001.

94. I. S. Didenko, F. S. Hickernell, and N. F. Naumenko, "Theoretical Aspects of GSAW and HVPSAW Propagation Properties for ZnO Films on SiC and Correlation with Experimental Data", *Proc. of 1999 IEEE Ultrasonics Symposium*, pp313, 1999

95. S. Muthukumar, Y. Chen, J. Zhong, F. Cosandey, Y. Lu, and T. Siegrist, "Metalorganic Chemical Vapor Deposition and Characterizations of Epitaxial $Mg_xZn_{1-x}O$ ($0 \leq x \leq 0.33$) Films on r-sapphire Substrates", *Journal of Crystal Growth*, vol. 261, pp.316, 2004

96. A. Rubio, J. L. Corkill, M. L. Cohen, E. L. Shirley, and S. G. Louie, "Quasiparticle band structure of AlN and GaN", *Physics Review B*, vol. 48, pp. 11810, 1993

97. S. J. Ness, "Stress Analysis of Silicon Carbide Microelectromechanical Systems using Raman Spectroscopy", *Air Force Institute of Technology*, March 2003

98. A.F. Wright, "Elastic Properties of Zinc-blende and Wurtzite AlN, GaN and InN", *Journal of Applied Physics*, vol. 82, no.6, pp. 2833, 1997

99. G. Simmons and H. Wang, "Single Crystal Elastic Constants and Calculated Aggregate Properties: A Handbook", *Cambridge, MA: M.I.T. Press*, 1971

100. D. W. Oliver and G. A. Slack, "Ultrasonic Attenuation in Insulators", *Journal of Applied Physics*, vol. 37, no. 5, pp. 1542, 1966

101. A. A. Glagovski, S. N. Ivanov, A. N. Makletsov, V. V. Medved, V. N. Posadski, and E. A. Semenov, " Study of Acoustic Properties of Silicon Carbide", *Radiotechnika I Elektronika*, vol. 24, pp.386, 1979 (in Russia)

102. M. Pomerantz, "Ultrasonic Attenuation by Phonons in Insulators", *Proc. of 1972 IEEE Ultrasonics Symposium*, pp.479, 1972

103. V. Craciun, J. Elders, J. G. E. Gardeniers, and I. W. Boyd, "Characteristics of High Quality ZnO Thin Films Deposited by Pulsed Laser Deposition", *Applied Physics Letters*, vol. 65, no. 23, pp. 2963, 1994

104. F. Craciun, P. Verardi, M. Dinescu, G. Guidarelli, "Reactive Pulsed Laser Deposition of Piezoelectric and Ferroelectric Thin Films", *Thin Solid Film*, vol. 343-344, pp. 90, 1999

105. Y. Kashiwaba, K. Haga, H. Watanabe, B. P. Zhang, Y. Segawa, and K. Wakatsuki, "Structures and Photoluminescence Properties of ZnO Films Epitaxially Grown by Atmospheric Pressure MOCVD", *Physica Status Solidi B*, vol. 229, pp. 921, 2002

106. B. P. Zhang, Y. Segawa, K. Wakatsuki, Y. Kashiwaba, and K. Haga, "Structural and Optical Properties of ZnO Films Grown on r–$Al_2O_3$ Substrates", *Applied Physics Letters*, vol. 79, pp. 3953, 2001

107. S. J. Chang, Y. K. Su, and Y. P. Shei, "High Quality ZnO Thin Films on InP Substrates Prepared by Radio Frequency Magnetron Sputtering. I. Material Study", *Journal of Vacuum Science and Technology A,* vol. 13, no. 2, pp.381, 1995

108. J. B. Lee, H. J. Lee, and J. S. Park, "Effects of Two-step Deposition and Thermal Treatment on the Frequency Response Characteristics of ZnO SAW Devices", *Proc. of 2003 IEEE Frequency Control Symposium*, pp.868, 2003

109. S. Y. Chu, W. Water, and J. T. Liaw, "Influence of Postdeposition Annealing on the Properties of ZnO Films Prepared by RF Magnetron Sputtering", *Journal of the European Ceramic Society*, vol. 23, pp. 1593, 2003

110. Y. Yoshino, K. Inoue, M. Takeuchi, and K. Ohwada, "Effect of Substrate Surface Morphology and Interface Microstructure in ZnO Thin Films Formed on Various Substrates", *Vacuum*, vol. 5, no. 4, pp. 601, 1998

111. M. Kadota, T. Miura, and M. Minakata, "Piezoelectric and Optical Properties of ZnO Films Deposited by an Electron–cyclotron-resonance Sputtering System", *Journal of Crystal Growth*, vol. 237/239, pp.523, 2002

112. T. Hata, E. Noda, O. Morimoto, and T. Hada, "High Rate Deposition of Thick Piezoelectric ZnO Films using a New Magnetron Sputtering Technique", *Applied Physics Letters*, vol. 37, pp. 633, 1980

113. E. L Adler, "Matrix Methods Applied to Acoustic Waves in Multilayers," *IEEE Trans. on Ultrasonics, Ferroelectrics and Frequency Control*, vol. 37, no. 6, pp. 485, 1990.

114. C. R. Gorla, N. W. Emanetoglu, S. Liang, W. E. Mayo, Y. Lu, M. Wraback, and H. Shen, "Structural, Optical and SAW Properties of Epitaxial ZnO Films Grown on $(01\bar{1}2)$ Sapphire by MOCVD", *Journal of Applied Physics*, vol. 85, no. 5, pp. 2595, 1999

115. C. R. Gorla, S. Liang, W. E. Mayo and Y. Lu, "Structure and Interface-Controlled Growth Kinetics of $ZnAl_2O_4$, Formed at $(11\bar{2}0)$ ZnO/$(01\bar{1}2)$ $Al_2O_3$ Interface", *Journal of Applied Physics,* vol. 87, no. 8, pp. 3736, 2000

116. J. Zhu, Y. Chen, G. Saraf, N. W. Emanetoglu, and Y. Lu, "Voltage Tunable Surface Acoustic Wave Phase Shifter Using Semiconducting/piezoelectric ZnO Dual-layers Grown on r-$Al_2O_3$", *Applied Physics Letters*, vol. 89, pp 103513, 2006

117. R. H. Wittstruck, N. W. Emanetoglu, Y. Lu, S. Laffey, and A. Ballato, "Properties of Transducers and Substrates for High Frequency Resonators and Sensors", *Journal of the Acoustic Society of America*, vol. 118 no. 3, pp.1414, 2005

118. A. B. M. A. Ashrafi, B. P. Zhang, N. T. Binh, K.Wakatsuki, and Y. Segawa, "High-quality ZnO Layers Grown on 6H-SiC Substrates by Metalorganic Chemical Vapor Deposition", *Jpn. Journal of Applied Physics*, vol. 1, no. 43, pp. 1114, 2004

119. A. B. M. A. Ashrafi, N. T. Binh, B. P. Zhang, and Y. Segawa, "Strain Relaxation and its Effect in Exciton Resonance Energies of Epitaxial ZnO Layers Grown on 6H-SiC Substrates", *Applied Physics Letters*, vol. 84, pp. 2814, 2004

120. A. B. M. A. Ashrafi, N. T. Binh, B. P. Zhang, and Y. Segawa, "Temperature-dependent Photoluminescence of ZnO Layers Grown on 6H-SiC Substrates", *Journal of Applied Physics*, vol. 95, pp. 7738, 2004

121. W. J. Li, E. W. Shi, W. Z. Zhong, and Z. W. Yin, "Growth Mechanism and Growth Habit of Oxide Crystals", *Journal of Crystal Growth*, vol. 203**,** pp. 186, 1999

122. Ya. I Alivov, B. Xiao, Q. Fan, H. Morkoç and D.Johnstone, "Band Offset Measurements of ZnO/6H-SiC Heterostructure System", *Applied Physics Letters*, vol. 89, pp. 152115, 2006

123. A. Ballato, "Transmission-line Analogs for Piezoelectric Layered Structures", Ph.D. dissertation, *Polytechnic Institute of Brooklyn, NY,* June 1972.

124. A. Z. Sadek, W Wlodarski, K. Kalantar-zadeh, D.A. Powell, W. L. Hughes, B.A. Buchine, and Z. L. Wang, "$H_2$ and $NO_2$ Gas Sensors with ZnO Nanobelt Layer on 36º $LiTaO_3$ and 64º $LiNbO_3$ SAW Transducer", *Proc. of 2005 IEEE Sensor*, pp,1343, 2005

125. X. Wang, J. Zhang, and Z. Zhu, "Ammonia Sensing Characteristics of ZnO Nanowires Studied by Quartz Crystal Microbalance", *Applied Surface Science*, vol. 252, pp. 2404, 2006

126. Y. Zhang, K. Yu, S. Quyang, L. Luo, H. Hu, Q. Zhang, and Z. Zhu, "Detection of Humidity Based on Quartz Crystal Microbalance Coated with ZnO Nanostructure Film", *Physica B*, vol. 368, pp. 94, 2005

127. X. Zhou, J. Zhang, T. Jiang, X. Wang, and Z. Zhu, "Humidity Detection by Nanostructured ZnO: A Wirelss Quartz Crystal Microbalance Investigation", *Sensors and Actuators A*, vol. 135, pp.209, 2007

128. O. Taratula, E. Galoppini, D. Wang, D. Chu, Z. Zhang, H. Chen, G. Saraf, and Y. Lu, "Binding Studies of Molecular Linkers to ZnO and MgZnO Nanotip Films", *Journal of Physical Chemistry B.,* March 2006

129. Z. Zhang, H. Chen, J. Zhong, Y. Chen, and Y. Lu, "ZnO Nanotip-based QCM Biosensors**"**, *Proc. of 2006 IEEE Frequency Control Symposium,* pp.545, 2006

130. H. Chen, J. Zhong, G. Saraf, Z. Zhang, Y. Lu, L. A. Fetter, and C. S. Pai, "Properties of ZnO Nanotips Selectively Grown by MOCVD", *Proc. of SPIE*, vol. 5592-31, pp. 164, 2004

131. J. Zhong, G. Saraf, S. Muthukumar, H. Chen, Y. Chen, and Y. Lu, "ZnO Nanotips Grown on Silicon Substrates by Metal-Organic Chemical-Vapor Deposition", *TMS & IEEE J. Electronic Materials*, vol. 33, pp. 654, 2004

132. O. Taratula, E. Galoppini, D. Wang, D. Chu, Z. Zhang, H. Chen, G. Saraf, and Y. Lu, "Binding Studies of Molecular Linkers to ZnO Nanotips", *Journal of Physical Chemistry B*, vol. 110, pp. 6506, 2006

133. Z. Yan, X. Y. Zhou, G. K. H. Pang, T. Zhang, W. L. Liu, J. G. Cheng, Z. T. Song, and S. L. Feng, L. H. Lai, J. Z. Chen, and Y. Wang, "ZnO-based Film Bulk Acoustic Resonator for High Sensitivity Biosensor Applications", *Applied Physics Letters*, vol. 90, pp. 143503, 2007

# CURRICULUM VITA

YING CHEN

## Education Background

| | |
|---|---|
| June 1999 | B.S. in Information Science and Electronic Engineering, Zhejiang University, Hangzhou, Zhejiang, P. R. China |
| March 2002 | M. S. in Information Science and Electronic Engineering, Zhejiang University, Hangzhou, Zhejiang, P. R. China |
| May 2008 | Doctor of Philosophy in Electrical and Computer Engineering Rutgers University, New Brunswick, New Jersey |

## Principal Occupation

Research Assistant (Aug. 2002 to Mar. 2007)

- Fabrication and testing of ZnO/r-$Al_2O_3$ tunable surface acoustic wave (SAW) device as ultraviolet photodetectors;
- Fabrication and testing of ZnO/r-$Al_2O_3$ monolithically integrated tunable SAW (MITSAW) devices using $Mg_xZn_{1-x}O$/ZnO heterostructure;
- Study of piezoelectric properties, including phase velocity and electromechanical coupling coefficient, in ZnO based multilayer structures;
- Development of $Mg_xZn_{1-x}O$ thin film bulk acoustic wave resonators for sensor application.

Teaching Assistant: *Capstone Design of Microelectronic Processing* (Fall 2006)
*Digital Electronics* (Spring 2007)

Interim Engineering Intern, Qualcomm, San Diego (Jun. 2007 to Dec. 2007)

## Publications

***Journals:***

1. Ying Chen, G. Saraf, Y. Lu, L. S. Wielunski, and T. Siegrist "a-plane $Mg_xZn_{1-x}O$ Films Deposited on r-sapphire and its SAW Characteristics", *Journal of Vacuum Science and Technology A: Vacuum, Surfaces, and Films*, vol. 25, issue 4, pp.857, 2007
2. J. Zhu, Ying Chen, G. Saraf, N. W. Emanetoglu, and Y. Lu, "Voltage Tunable Surface Acoustic Wave Phase Shifter Using Semiconducting/piezoelectric ZnO Dual-layers Grown on r-$Al_2O_3$", *Applied Physics Letters*, 89, pp 103513, 2006
3. G. Saraf, Ying Chen, T. Siegrist, L. S. Wielunski, and Y. Lu, "Hybrid Deposition of Piezoelectric $(11\bar{2}0)$ $Mg_xZn_{1-x}O$ $(0 \leq x \leq 0.3)$ on $(01\bar{1}2)$ r-Sapphire Substrates using RF Sputtering and MOCVD", *TMS & IEEE Journal of Electronic Materials,* vol. 35, No. 6, pp.1306, 2006

4. Ying Chen, N. W. Emanetoglu, G. Saraf, P. Wu, and Y. Lu, "Analysis of SAW Properties in ZnO/$Al_xGa_{1-x}N$/c-$Al_2O_3$ Structures", *IEEE Trans. on Ultrasonics, ferroelectrics and frequency control*, vol. 52, no. 7, pp.1161, 2005
5. N. W. Emanetoglu, J. Zhu, Ying. Chen, J. Zhong, Y. Chen, and Y. Lu, "Optoelectronic-acoustic Interaction in ZnO/r-$Al_2O_3$ for Tunable Surface Acoustic Wave Filters and Ultraviolet Photodetectors", *Applied Physics Letters*, 85, pp.3702, 2004.

***Conference Proceedings:***

1. Z. Zhang, H. Chen, J. Zhong, Ying Chen, and Y. Lu, "ZnO Nanotip-based QCM Biosensors**"**, *Proceedings of IEEE International Frequency Control Symposium,* pp.545, 2006
2. Ying Chen, G. Saraf, R. H. Wittstruck, N. W. Emanetoglu, and Y. Lu, **"**Studies on $Mg_x$ $Zn_{1-x}O$ Thin Film Resonator for Mass Sensor Application", *Proceedings of IEEE International Frequency Control Symposium,* pp.142, 2005
3. Ying Chen, N. W. Emanetoglu, Y. Chen, G. Saraf, Y. Lu, A. Parekh, V. Merai, M. Prophristic, D. Lu, D. S. Lee, and E. A. Armour, "Surface Acoustic Waves in ZnO/$Al_xGa_{1-x}N$/c-Sapphire Structures", *Proc. of 2003 IEEE International Ultrasonics Symposium*, pp.2130, 2003

***Book chapter:***

1. Yicheng Lu, Nuri W. Emanetoglu, and Ying Chen, "ZnO Piezoelectric Devices", in *Zinc* Oxide *Bulk, Thin Films and Nanostructures: Processing, Properties and Applications,* Elsevier Limited, USA, Feb 2006

**Patent Applications:**

- "MOCVD-Sputtering Hybrid Technology to Deposit Multilayer and Multifunctional Epitaxial Films", Y. Lu, Ying Chen, G. Saraf, and J. Zhu, US patent filed in Oct. 2006
- "Sensor Technology Based on Integration of ZnO Nanostructures with QCM and TFBAR Devices", Y. Lu, Ying Chen, and Z. Zhang, US patent filed in Nov. 2006